Precision tests of the electroweak interaction at the Z pole

M. Martinez

Institut de Física d'Altes Energies, Universitat Autònoma de Barcelona, 08193 Bellaterra (Barcelona), Spain

R. Miquel

Institut de Física d'Altes Energies, Universitat Autònoma de Barcelona, 08193 Bellaterra (Barcelona), Spain and Departemento ECM, Universit Barcelona, Facultad de Física, Diagonal 647, 08028 Barcelona, Spain

L. Rolandi

European Laboratory for Particle Physics (CERN), 1211 Geneva 23, Switzerland

R. Tenchini

Istituto Nazionale di Fisica Nucleare, Sezione di Pisa, 56010 San Piero a Grado (Pisa), Italy

The measurements of the properties of the Z boson performed with the large data samples collected at LEP and SLC challenge the standard model of the electroweak interaction with unprecedented precision. The Z mass is measured to 2 parts in 10^5, while other relevant electroweak observables such as the electroweak mixing angle, which is related to the strength of the neutral current, are measured with an accuracy of 1 part in 10^3. At this level of precision the effects of electroweak radiative corrections and in particular of the nontrivial loop contributions are visible. Assuming the validity of the standard model, the top mass can be predicted with a precision of about 10% and with a value in good agreement with the direct measurements. The global fit of electroweak data constrains the mass of the Higgs boson, giving an indirect indication of a relatively light Higgs. The overall agreement of the data with the predictions of the standard model is good, considerably limiting the room available for new physics. This paper describes the experimental techniques that led to such a thorough test of the electroweak theory. The basic theoretical concepts are reviewed and the measurements compared with theoretical predictions. [S0034-6861(99)01003-X]

CONTENTS

I. Introduction 576
A. Parameters of the minimal standard model 576
1. The Fermi constant 577
2. The fine-structure constant at M_Z^2 scale 578
3. The top mass 578
4. The strong-coupling constant at M_Z^2 scale 578
B. Radiative corrections 578
1. Radiative corrections to the e^+e^- annihilation cross section 579
2. Vacuum polarization corrections 579
3. Vertex corrections 580
4. The photon self-energy 580
5. Radiative corrections to the W mass prediction 581
C. Precision of the MSM calculations including radiative corrections 582
D. Dependence of the MSM predictions on the input parameters 583
E. LEP and its detectors 584
F. SLC and SLD 585
II. The Z Line Shape 586
A. The fitting formula 586
B. Cross sections 587
1. Luminosity determination 587
2. Hadronic cross section 588
3. Leptonic cross sections 589
C. LEP energy calibration 589
1. The energy of electrons and positrons in LEP 590
2. Energy calibration with resonant depolarization 590
3. The time variation of the collision energy 591
D. Results from the Z line shape analysis 591
1. The Z mass 592
2. The Z width 592
3. $R_\ell = \Gamma_h/\Gamma_\ell$ 593
4. The hadronic peak cross section 593
E. Derived quantities 594
F. S-matrix approach 594
III. Z Decay Widths to Quarks 595
A. Heavy-flavor tagging 596
1. Lifetime tagging 596
2. Lepton tagging 598
3. Event shape tagging 600
4. D^* tagging 600
B. Measurement of R_b from double tagging 601
C. R_c from the D^* and D mesons 602
D. Average of R_b and R_c 603
IV. Asymmetries at the Z pole 603
A. Lepton forward-backward asymmetries 605
B. Tau polarization asymmetries 606
C. Measurement of A_{LR} at SLD 607
D. Universality of the neutral-current couplings 608
E. Quark forward-backward asymmetry 609
1. Measuring the asymmetry of b and c quarks from decays into leptons 609
2. Measuring c quark asymmetry from D* 610
3. Measuring b quark asymmetry from jet charge 610
4. Corrections to the measured heavy-quark asymmetries 611

5. Measurement of jet charge asymmetry in $Z \to q\bar{q}$ 612
6. Measurements of heavy-quark forward-backward polarized asymmetries 613
F. Comparison of the different determinations of $\sin^2\theta_{\text{eff}}$ 613
V. *W* Mass Measurement 614
A. Measurement of the *W* mass at $p\bar{p}$ colliders 614
B. Measurement of the *W* mass at LEP 614
C. Neutrino-nucleon scattering 615
VI. Standard-Model Tests 616
A. Standard-model fits 616
B. Tests of new physics using the ε's variables 619
1. Implications for the minimal supersymmetric standard model 620
2. Implications for technicolor 621
C. Limits on extra neutral bosons 621
D. Conclusions and outlook 622
Acknowledgments 623
Appendix: Cross Sections and Formulae 623
References 624

I. INTRODUCTION

The existence of the neutral weak currents was predicted by the "standard model" of the electroweak interaction (Glashow, 1961; Weinberg, 1967; Salam, 1968) before their discovery by Hasert *et al.* (1973) at CERN. In the following years one of the fundamental parameters of the theory, $\sin^2\theta_W$, was measured precisely at CERN and Fermilab in the deep-inelastic scattering of high-energy neutrino beams on isoscalar targets by the collaborations FMM (1985), CCFR (1985), CDHS (1986), and CHARM (1987). The intermediate vector bosons were eventually discovered at CERN by the UA1 collaboration (1983a, 1983b) and UA2 collaboration (1983a, 1983b) in proton-antiproton collisions.

The electroweak theory predicts relations among experimentally measurable quantities. Any observable, like the masses of the vector bosons, can be predicted in terms of a finite number of parameters, which have to be determined in previous experiments. New measurements are compared with predictions. If these agree within their errors, the measurement can be used to further constrain the input parameters. Non-agreement indicates inconsistency of the theoretical framework and new physics.

The comparison between the measured masses of the intermediate vector bosons and the prediction based on measurements of neutrino scattering cross sections and the muon lifetime was a major quantitative test of the electroweak theory (Amaldi *et al.*, 1987; Costa *et al.*, 1988). It established the existence of radiative corrections at three-standard-deviation level. The mass of the top quark—which affects the predictions of these measurements only via radiative corrections—was indirectly constrained (Langacker, 1989) at 90% confidence level in the range $40\,\text{GeV} < m_t < 210\,\text{GeV}$.

This paper describes how the high-precision experiments performed with e^+e^- collisions at LEP and SLC have tested the electroweak theory to a level comparable to the g-2 experiments (Farley and Picasso, 1990) which were performed to test quantum electrodynamics.

The accurate measurements of the mass, width, and partial widths of the Z boson and of the asymmetries in its production and decay allow for the first time quantitative tests of the electroweak theory beyond the tree-level prediction. Using these measurements, the LEP Electroweak Group (1997) has constrained the mass of the top quark to $m_t = 181 \pm 6 \pm 17$ GeV, where the second error accounts for the variation in the prediction when the mass of the Higgs boson, the last yet-unknown parameter of the theory, is varied in the range from 70 to 1000 GeV. The predicted value of m_t is in very good agreement with the top mass value $m_t = 175.6 \pm 5.5$ GeV reported by the collaborations CDF (1997b) and DØ (1997b), confirming once again the success of the electroweak theory.

After a description of the parameters used to compute the predictions of the minimal standard model and a discussion of the precision of these predictions, the present section contains a very brief description of LEP and its detectors and of SLD. The subsequent sections describe the precise measurements performed by the LEP collaborations and by SLD and also include a brief description of the measurement of the *W* mass. The overall comparison of the measurements with the standard-model predictions is left to the last section.

LEP completed data taking at the Z peak in summer 1995, but the analysis of the data has not yet been completed. SLD is still taking data. This report includes many preliminary results presented in August 1997 at the International Europhysics Conference on High-Energy Physics in Jerusalem. They may slightly change in the future when the final analyses are available.

A. Parameters of the minimal standard model

The minimal standard model (MSM) most commonly used to predict the observables measured at LEP and SLC has the following precisely known quantities as input parameters:

(i) α, the fine-structure constant measured at values of q^2 close to zero. It determines the strength of the QED part of the neutral currents. $\alpha^{-1} = 137.035\,989\,5(61)$.
(ii) G_F, the Fermi constant measured in muon decay. It determines the strength of the charged current. $G_F = 1.16639(2) \times 10^{-5}\ \text{GeV}^{-2}$.
(iii) M_Z, the mass of the Z boson, as measured at LEP. $M_Z = 91.1867(20)$ GeV.

Any process mediated by the weak or electromagnetic current can be computed at tree level from these three quantities,[1] neglecting the small phase-space effects caused by the nonzero mass of the final-state fermions.

[1]The Cabibbo-Kobayashi-Maskawa mass-mixing matrix is needed in addition for tree-level predictions of charged-current processes involving flavor-tagged hadronic final states.

In particular, the strength of the weak neutral current s_W^2 ($c_W^2=1-s_W^2$) and the mass of the W boson M_W are given by

$$\sqrt{2}G_F M_Z^2=\frac{e^2}{4s_W^2c_W^2}=\frac{\pi\alpha}{s_W^2c_W^2},$$

$$M_W^2=\frac{\pi\alpha}{\sqrt{2}G_F s_W^2}, \tag{1}$$

$$s_W^2\equiv 1-\frac{M_W^2}{M_Z^2}.$$

The precision of the measurements described in this paper is such that the tree-level prediction is not accurate enough to match the experimental precision and higher orders have to be included in the calculations. This can be easily seen by comparing the prediction of $M_W=80.937$ GeV computed using the previous equations with the measurement given in Sec. V: the prediction is 0.7% larger than the measured value, which is known with a precision of about 0.1%.

When higher orders are included in the calculations, other input parameters are needed to predict the observables measured at LEP and SLC:

(i) m_f, the masses of all fermions. The contribution of the fermion masses to the photon self-energy (see Sec. I.B) is taken into account by replacing the input parameter $\alpha(0)$ with $\alpha(M_Z^2)$, the fine-structure constant at $q^2=M_Z^2$, which is known with a precision of 7×10^{-4}. The fermion masses also appear in the weak boson self-energy corrections in the form $(m_i^2-m_j^2)/M_Z^2$, where i and j are two fermions of the same isodoublet, and in the vertex corrections in the form $(m_f/M_Z)^2$. These corrections are in general small and known with sufficient accuracy, except for the case of the top quark. The mass of the top quark is known with a precision of 3%.

(ii) M_H, the mass of the Higgs boson. It appears in the higher-order terms as a correction of the form $\ln(M_H/M_Z)$ and therefore has a small effect on the predictions. The value of the Higgs mass is bounded from below at about 77 GeV from searches at LEP (Janot, 1997) and from above at 1 TeV, above which new strong interactions appear (Cabibbo *et al.*, 1979; Lindner, 1986; Luscher and Weisz, 1988; Sher, 1989; Altarelli and Isidori, 1994; Casas *et al.*, 1995).

(iii) α_s, the strong-coupling constant at $q^2=M_Z^2$. It appears in gluon radiation corrections of any weak process involving quarks and is known to about 3% of its value. It also has a minor effect in processes where quarks contribute only through radiative corrections.

Any observable O_i (electroweak observable) can be computed in the MSM as a function of these parameters,

$$O_i=f_i[\alpha(M_Z^2),G_F,M_Z,m_f,M_H,\alpha_s],$$

with sufficient accuracy to match the experimental precision. The accuracy of the prediction is limited mainly by the precision of the least known parameters of the model (m_t,M_H,α_s) and not by missing high orders in the radiative corrections (see Sec. I.C).

The comparison between the measurements of many electroweak observables done at LEP and SLC and their prediction as a function of $m_t,M_H,\alpha_s(M_Z^2)$ is the main subject of this paper. The overall fit can be used to further constrain the parameters—in particular M_H—and the quality of the fit provides a test of the structure of the MSM.

The next sections describe the determinations of the MSM parameters measured elsewhere than at LEP and how these parameters enter in the predictions of other electroweak observables through radiative corrections.

1. The Fermi constant

The Fermi constant G_F is defined through the muon lifetime τ_μ. Within the Fermi model, τ_μ is given by (Behrends *et al.*, 1956; Kinoshita and Sirlin, 1959)

$$\frac{1}{\tau_\mu}=\frac{G_F^2m_\mu^5}{192\pi^3}F\left(\frac{m_e^2}{m_\mu^2}\right)\left(1+\frac{3}{5}\frac{m_\mu^2}{M_W^2}\right)\left[1+\frac{\alpha(m_\mu^2)}{2\pi}\left(\frac{25}{4}-\pi^2\right)\right], \tag{2}$$

where $F(x)$ is the phase-space term

$$F(x)=1-8x+8x^3-x^4-12x^2\ln x$$

and

$$\frac{1}{\alpha(m_\mu^2)}=\frac{1}{\alpha}-\frac{1}{3\pi}\ln\left(\frac{m_\mu^2}{m_e^2}\right)+\frac{1}{6\pi}.$$

Equation (2) includes mass effects and the leading QED corrections.

The most precise determinations of τ_μ are those of Giovannetti *et al.* (1984) and Bardin *et al.* (1984). In both cases, a low-energy π^+ beam was stopped. The muons from the pion decays were also stopped, and the positrons from the muon decays then observed either in a water Cherenkov detector (Giovannetti *et al.*, 1984) or by scintillator telescopes (Bardin *et al.*, 1984). The time distributions of the signal positrons gave the μ^+ lifetime.

The combined result for the muon lifetime is

$$\tau_\mu=(2197.03\pm0.04)\text{ ns},$$

from which Eq. (2) gives

$$G_F=1.16639(2)\times10^{-5}\text{ GeV}^{-2}.$$

The 9×10^{-6} relative error on G_F from the input quantities is dominated by the uncertainty on τ_μ. The estimated uncertainty from missing second-order QED corrections to Eq. (2) is larger by a factor of 2. In the parametrization used in this paper G_F is defined by Eq. (2); therefore the uncertainties induced by the missing QED corrections are assigned to the quantities computed with G_F.

2. The fine-structure constant at M_Z^2 scale

The QED coupling constant $\alpha(q^2)$ is very precisely determined at $q^2 \sim 0$ through the measurements of the quantized Hall resistance (Bliek *et al.*, 1985; Cage *et al.*, 1985; Hartland *et al.*, 1985; Wada *et al.*, 1985; Van del Wel *et al.*, 1985; Delhaye *et al.*, 1986). It can be calculated with equivalent precision from the measurement of the electron's anomalous magnetic moment (Van Dick *et al.*, 1984) using the QED radiative corrections to the eighth-order term by Kinoshita and Lindquist (1981, 1983).

The value of $\alpha(0)$ is obtained from a combined fit to a large set of interrelated atomic, molecular, and nuclear data (Cohen and Taylor, 1986) which is also sensitive to many other parameters that are left free in the fit. The result is

$$\alpha^{-1}(0) = 137.035\,989\,5\ (61).$$

The coupling constant at $q^2 = M_Z^2$ is obtained by adding to $\alpha(0)$ the radiative corrections due to the photon self-energy (see Sec. I.B). They depend on the masses of the fermions as $\ln(s/m_f^2)$ and hence are large for light fermions. A special treatment, described in Sec. I.B.4, is needed for the masses of the light quarks, since they are not well defined. The correction $\Delta\alpha$ is

$$\Delta\alpha = 0.0632 \pm 0.0007,$$

resulting in

$$\alpha^{-1}(M_Z^2) = \frac{1-\Delta\alpha}{\alpha(0)} = 128.89 \pm 0.09.$$

As discussed in Sec. I.B.4, the error on $\alpha(M_Z^2)$ is dominated by the uncertainty on the hadronic contribution to the vacuum polarization corrections.

3. The top mass

The top quark was discovered by CDF (1995b) and DØ (1995) at Fermilab. They have recently performed analyses (CDF, 1997b; DØ, 1997b) of their full data sample of about $110\,\mathrm{pb}^{-1}$ to measure its mass.

Top quarks are produced in $p\bar{p}$ collisions at $\sqrt{s} = 1.8\,\mathrm{TeV}$ predominantly in pairs with a cross section of about 7 (pb). They decay into a W boson and a b quark, producing multijet events which can be classified according to the W decay modes. The most useful channel for the mass measurement is when one of the W's decays into an electron or muon plus neutrino and the other W decays in two hadronic jets. This channel corresponds to about 30% of the $t\bar{t}$ events. For each event an average top mass is calculated with a kinematic fit requiring that the two top masses be equal and constraining the masses of the W's.

The mass of the top quark is determined by comparing the measured distributions of the average mass with distributions obtained from Monte Carlo simulations for several possible input values of the top mass. The likelihood fit gives

$$m_t = 175.6 \pm 5.5\,\mathrm{GeV},$$

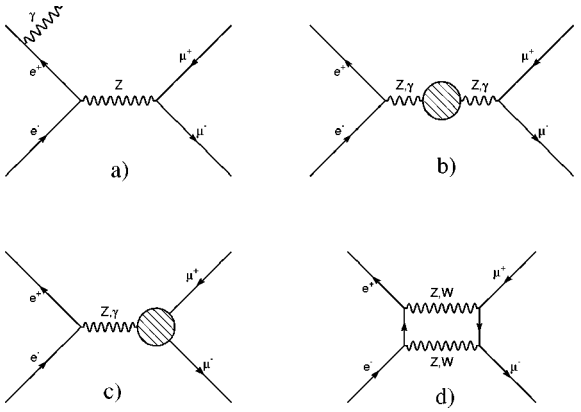

FIG. 1. Examples of Feynman diagrams for the process $e^+e^- \to \mu^+\mu^-$ at one-loop level. (a) QED corrections; (b) vacuum polarization corrections; (c) vertex corrections; (d) box corrections.

where the quoted uncertainty also includes systematic errors of the same size as the statistical ones. They are mainly due to uncertainties in the energy scale of the calorimeters and in the simulation of the gluon radiation.

4. The strong-coupling constant at M_Z^2 scale

The strong-coupling constant has been measured with a variety of methods in recent years, ranging in energy from the study of tau lepton decays to that of jet properties in e^+e^- annihilations at high energy. The measurements are expressed at the M_Z scale through the evolution predicted by the renormalization-group equations (Altarelli, 1982).

In most cases the accuracy of the measurements is limited by theoretical uncertainties related either to uncalculated higher-order perturbative QCD corrections to the predictions or to low-energy nonperturbative effects.

There are many good reviews on the subject (Schmelling, 1996). The average value of all α_s measurements excluding the constraint given by the electroweak fit is usually quoted as

$$\alpha_s(M_Z) = 0.118 \pm 0.003,$$

although some authors think the error should be increased to 0.005 (Altarelli, 1997).

B. Radiative corrections

Radiative corrections at LEP/SLC can be classified into four categories, from the most to the least important numerically:

(i) QED corrections [see Fig. 1(a)]: these are the corrections involving the radiation of a real photon or the exchange of a virtual photon. They are numerically very important (more than 30% reduction of the Z-pole cross section, for instance) and known with sufficient accuracy. See Sec. II.A for details.

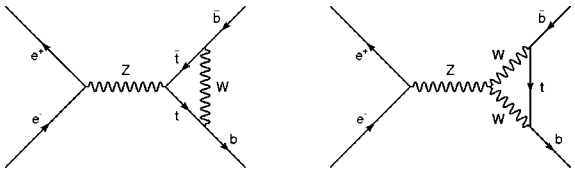

FIG. 2. Feynman diagrams for vertex correction to the $Z \to b\bar{b}$ vertex involving the top quark.

(ii) Vacuum polarization [see Fig. 1(b)], also called oblique corrections: they are numerically important and interesting for their sensitivity to new physics. They are universal, in the sense that they do not depend on the final state. The large [$\mathcal{O}$ (10%)] correction due to the $\gamma\gamma$ propagator can be renormalized by the use of the running QED coupling constant $\alpha(M_Z^2)$, while the ZZ and γZ propagator corrections can have $\mathcal{O}$ (1%) effects on the Z-pole observables.

(iii) Vertex corrections [see Fig. 1(c)], their size depends on the final state and they are large for the $Z \to b\bar{b}$ vertex [$\mathcal{O}$ (1%)]. Some of them can also be interesting for new physics.

(iv) Box diagrams [see Fig. 1(d)]. These are almost negligible at LEP1/SLC energies.

The oblique corrections are the most interesting type of radiative correction at LEP/SLC due to a property of the MSM not present in pure QED and QCD: the nondecoupling property. Nondecoupling, common to theories in which a large particle mass is associated with a large coupling constant, means that the effect of particles with masses much larger than the electroweak scale does not vanish as M_Z/M_X to some power: the heavy degrees of freedom do not decouple, and their contributions to vacuum polarization corrections can instead grow with M_X.

An example of such a particle is the top quark: the contribution of the top-quark loop to the photon vacuum polarization (QED) is proportional to $(M_Z/m_t)^2$, while its contribution to the Z self-energy for high top mass is proportional to $(m_t/M_Z)^2$.

Nondecoupling also appears in the $Z \to b\bar{b}$ vertex. The contribution of the vertex correction (see Fig. 2) involving the top quark is also proportional to $(m_t/M_Z)^2$.

The vacuum polarization and the vertex corrections to processes involving two fermions in the initial and final states, like e^+e^- annihilation into $f\bar{f}$, can be implemented using an amplitude with the same structure as the tree-level amplitude and absorbing the effects of the radiative corrections into energy-dependent complex couplings (Lynn, 1988; Hollik, 1990a; Bardin *et al.*, 1991c).

This procedure, called the improved Born approximation, is quite natural for neutral-current processes since the vacuum polarization and vertex corrections at one-loop level are naturally separated from the QED ones, forming a gauge-invariant subset. ZZ and WW box diagrams can also be separated from the external QED corrections and, even though their numerical effects are small near the Z resonance, they are included as explicit corrections to the improved Born amplitude.

The implementation of the one-loop radiative corrections in the calculation of the differential cross section for fermion production in e^+e^- annihilation near the Z pole and in the prediction of the W mass are briefly described in the following sections. A detailed discussion can be found in a paper by Hollik (1990a).

1. Radiative corrections to the e^+e^- annihilation cross section

In the improved Born approximation the amplitude for the process $e^+e^- \to f\bar{f}$ has the same structure as the tree-level amplitude and contains three running complex couplings, $\overline{\alpha}(s)$, $\overline{s}_W^2(s)$, and $\overline{\rho}(s)$:

$$\begin{aligned}\bar{A} = {} & Q_e Q_f \frac{4\pi\overline{\alpha}(s)}{s}[\gamma_\mu \otimes \gamma^\mu] \\ & + \sqrt{2} G_F M_Z^2 \overline{\rho}(s) \frac{1}{s - M_Z^2 + is\dfrac{\Gamma_Z}{M_Z}} \\ & \times [\gamma_\mu (I_3^e - 2Q_e \overline{s}_W^2(s)) - \gamma_\mu \gamma_5 I_3^e] \\ & \otimes [\gamma^\mu (I_3^f - 2Q_f \overline{s}_W^2(s)) - \gamma^\mu \gamma^5 I_3^f]. \end{aligned} \tag{3}$$

Here the first term corresponds to the photon exchange and the second to the Z exchange. The notation $A_\mu \otimes B^\mu$ in the previous equation represents a bilinear combination of spinors u and v:

$$A_\mu \otimes B^\mu \equiv [\bar{v}_e A_\mu u_e] \cdot [\bar{u}_f B^\mu v_f].$$

The running couplings have contributions from vacuum polarization corrections and from vertex corrections. The former are the same for all $f\bar{f}$ final states, while the latter depend on the flavor of the final state. They are discussed in turn.

2. Vacuum polarization corrections

As shown in Fig. 1(b) there are three different loop diagrams and consequently three different corrections: one involving photon lines to both vertices (the photon self-energy), one with a photon line to one vertex and a Z line to the other (γZ mixing), and one with Z lines to both vertices (the Z self-energy).

The correction $\Pi^\gamma(s)$ is evaluated by calculating the loop diagram of Fig. 1(b) with photon lines at both vertices and is absorbed in the effective complex coupling constant $\overline{\alpha}(s)$, defined as

$$\overline{\alpha}(s) \equiv \frac{\alpha(0)}{1 + \Pi^\gamma(s)} = \frac{\alpha(0)}{1 - \Delta\alpha(s)}, \tag{4}$$

where $\Delta\alpha(s)$ is a complex quantity whose real part was already introduced in Sec. I.A.2. Here $\Pi^\gamma(s)$ is defined as

$$\Pi^\gamma(s) = \frac{\Sigma_\gamma(s)}{s},$$

where $\Sigma_\gamma(s)$ stands for the photon self-energy function (Hollik, 1990a).

Following the procedure described by Hollik (1990a), we find that the correction induced by the γZ mixing is absorbed in an effective mixing angle $\overline{s}^2_W$:

$$\overline{s}^2_W(s) \equiv s^2_W(1+\Delta\kappa(s)), \tag{5}$$

where the complex quantity $\Delta\kappa(s)$ is

$$\Delta\kappa(s) = -\frac{c_W}{s_W}\frac{\Pi^{\gamma Z}(s)}{1+\Pi^\gamma(s)}. \tag{6}$$

When we again follow the procedure of Hollik (1990a), using the tree-level relation (1), the real part of the Z self-energy is absorbed in the effective parameter $\overline{\rho}(s)$, not present at tree level, defined by

$$\frac{e^2}{4s^2_W c^2_W}\frac{1}{1+\Pi^Z(s)} = \sqrt{2}G_F M^2_Z \overline{\rho}(s)$$

with

$$\Pi^Z(s) = \frac{\mathrm{Re}[\Sigma_Z(s)]}{s-M^2_Z}.$$

The imaginary part of the Z self-energy can be interpreted (Hollik, 1990a) using the optical theorem as

$$\frac{\mathrm{Im}[\Sigma_Z(s)]}{1+\Pi^Z(s)} = \Gamma_Z(s) \cong \frac{s}{M^2_Z}\Gamma_Z(M^2_Z),$$

where $\Gamma_Z(s)$ is the Born total Z decay width computed in terms of effective couplings.

In the MSM at tree level $\overline{\rho}(s)$ is equal to 1, and it is convenient to define the quantity $\Delta\rho(s)$:

$$\overline{\rho}(s) \equiv 1+\Delta\rho(s). \tag{7}$$

Here $\Delta\rho(s)$ and $\overline{\rho}(s)$ are real quantities by definition, since they include only the real part of the Z vacuum polarization.

3. Vertex corrections

The vertex corrections are flavor dependent. They can be absorbed into the effective parameters making them flavor dependent, that is, having a set of effective parameters for every $\overline{ff}$ final state.

The vertex corrections to the Z amplitude at one-loop level can be introduced through the use of complex form factors F_{VZf} and F_{AZf} modifying the Born axial and vector couplings to the Z currents (Hollik, 1990a):

$$C^Z_\mu = [\gamma_\mu(Q^f + F_{VZf}(s) - F_{AZf}(s)\gamma_5)].$$

These form factors can be included in a redefinition of the couplings together with the vacuum polarization corrections. This is done by defining flavor-dependent complex effective weak mixing angles as

$$\sin^2\theta^f_{\mathrm{eff}}(s) \equiv s^2_W(1+\Delta\kappa(s)+\Delta\kappa_f(s)) \tag{8}$$

and the flavor-dependent complex effective ρ parameters as

$$\rho^f(s) \equiv (1+\Delta\rho(s)+\Delta\rho^f(s)).$$

The new quantities $\Delta\kappa_f(s)$ and $\Delta\rho^f(s)$ are given by the vertex functions $F_{VZf}(s)$ and $F_{AZf}(s)$ as

$$\Delta\kappa_f(s) = -\frac{1}{Q_f}\frac{c_W}{s_W}\left(F_{VZf}(s) - \frac{v_f}{a_f}F_{AZf}(s)\right)$$

$$\Delta\rho_f(s) = \left(1+\frac{F_{AZf}(s)}{a_f}\right)^2 - 1,$$

where

$$a_f = \frac{I^f_3}{2c_W s_W},$$

$$v_f = \frac{I^f_3 - 2Q_f s^2_W}{2c_W s_W}.$$

With the introduction of these complex flavor-dependent effective parameters, the Z exchange amplitude of Eq. (3) can be rewritten as

$$A_Z = \sqrt{2}G_F M^2_Z \frac{1}{s-M^2_Z+is\dfrac{\Gamma_Z}{M_Z}}[\gamma_\mu(g_{Ve}(s) - g_{Ae}(s)\gamma_5)] \otimes [\gamma^\mu(g_{Vf}(s) - g_{Af}(s)\gamma^5)], \tag{9}$$

where the complex effective vector and axial couplings are defined as

$$g_{Vf}(s) = \sqrt{\rho^f(s)}[I^f_3 - 2Q_f \sin^2\theta^f_{\mathrm{eff}}(s)],$$

$$g_{Af}(s) = \sqrt{\rho^f(s)}I^f_3. \tag{10}$$

Neglecting the small mass terms, we obtain the total Z decay width in terms of the effective couplings,

$$\Gamma_Z = \sum_f N^f_c \frac{G_F M^3_Z}{6\sqrt{2}\pi}[g^2_{Af}(M^2_Z) + g^2_{Vf}(M^2_Z)], \tag{11}$$

where the factor N^f_c is 1 for leptons and $3(1+\alpha_s/\pi)$ for quarks. The reduced differential cross sections (see Sec. II.A) for $\overline{ff}$ production can be computed in terms of the effective couplings using the amplitudes given in Eqs. (3) and (9). The explicit formulas are given in the Appendix.

The effective parameters introduced in this section are complex functions of s. In practice, however, their energy dependence is small and can be safely neglected near the Z peak region. The imaginary parts are also small. They affect observables that are sensitive to phase differences between photon and Z exchange diagrams. To the present level of precision of the observables discussed in this paper only the imaginary part of $\overline{\alpha}(s)$ has to be taken into account while the other imaginary parts can be safely neglected.

4. The photon self-energy

In the minimal standard model the radiative correction terms $\Delta\rho$ and $\Delta\kappa$ have important contributions from the masses of heavy particles like the top quark and the Higgs boson, whereas the contribution of the photon

self-energy $\Pi^{\gamma}(s)$ to $\Delta\alpha$ is sensitive to the fermion masses through $\ln(s/m_f^2)$ terms that are large for the light fermions.

The analytical expression (Kleiss *et al.*, 1989) of $\Pi^{\gamma}(s)$ is used to calculate the contribution of the leptons and of the top quark with negligible error. It cannot be used for the other quarks because nonperturbative QCD corrections at low energy scale are large.

The contribution of the light quarks is computed by relating (Cabibbo and Gatto, 1961) through unitarity the imaginary part of the Π^{γ} function to $R(s)$, the hadronic cross section in e^+e^- annihilation through one-photon exchange, normalized to the pointlike muon cross section:

$$R(s)=\frac{\sigma_{\gamma}^{h}(s)}{\sigma_{0}^{\mu}(s)}=\frac{\sigma_{\gamma}^{h}(s)}{4\pi\alpha^2/3s}.$$

The real part of Π^{γ} is computed via the dispersion integral,

$$\mathrm{Re}[\Pi_h^{\gamma}(s)]=\frac{\alpha s}{3\pi}\mathrm{Re}\int_{4m_{\pi}^2}^{\infty}\frac{ds'}{s'(s'-s+i\epsilon)}R(s'),$$

using the measured cross section of e^+e^- annihilation into hadrons. The most recent compilations of the experimental data (Burkhardt and Pietrzyk, 1995, Eidelman and Jegerlehner, 1995) result in

$$\Delta\alpha_h(M_Z^2)\equiv-\mathrm{Re}[\Pi_h^{\gamma}(M_Z^2)]=0.0280\pm0.0007. \quad (12)$$

The real part of the photon self-energy is obtained by adding to $\Delta\alpha_h$ the real parts of the leptonic and top contributions, giving

$$\Delta\alpha=0.0632\pm0.0007.$$

The error on $\Delta\alpha$ could be reduced by more precise measurements of the hadronic cross section in e^+e^- annihilation, especially in the region between 1 and 5 GeV center-of-mass energy.

5. Radiative corrections to the *W* mass prediction

The Fermi constant G_F is defined within the Fermi model through the muon lifetime τ_{μ}, Eq. (2). The Fermi model prediction for the muon lifetime can be interpreted at tree level in the framework of the standard model. As in Eq. (1), it relates the four-fermion coupling G_F to the product of the square of the W boson coupling to a fermion pair times the W boson propagator at $q^2\simeq0$,

$$G_F=\frac{\pi\alpha}{\sqrt{2}s_W^2}\frac{1}{M_W^2}. \quad (13)$$

When the radiative corrections are introduced, Eq. (13) becomes (Hollik, 1990a)

$$M_W^2=\frac{\pi\alpha}{\sqrt{2}}\frac{1}{G_F s_W^2}(1+\Delta r), \quad (14)$$

where

$$\Delta r=\frac{\mathrm{Re}[\Sigma_W(0)]}{M_W^2}+\frac{\alpha}{4\pi s_W^2}\left(6+\frac{7-4s_W^2}{2s_W^2}\ln c_W^2\right). \quad (15)$$

The first term accounts for the W self-energy correction (vacuum polarization), while the second corresponds to the remaining corrections (vertices and boxes).

The prediction for Δr given by Eq. (15) is split into parts of different origin:

$$\Delta r=\Delta\alpha-\frac{c_W^2}{s_W^2}\Delta\rho+\Delta r_{\mathrm{rem}}. \quad (16)$$

The photon vacuum polarization $\Delta\alpha$ has already been introduced in Sec. I.B.4; the second term $\Delta\rho$ is the radiative correction to the ρ parameter defined from the ratio of neutral-current to charged-current amplitude at $q^2=0$. The third term accounts for the remaining corrections.

In the minimal standard model (and also for extensions of the MSM with any number of Higgs doublets) at tree level, the ρ parameter is $\rho_0=M_W^2/(c_W^2M_Z^2)=1$. If one-loop corrections are included it becomes $\rho=1+\Delta\rho$.

With this definition the ρ parameter is the ratio of the neutral-current amplitude to the charged-current amplitude at low energy. It is essentially equivalent to the parameter $\overline{\rho}(s)$ introduced in Sec. I.B.1, and hence the leading terms of their radiative corrections are the same. In the MSM the leading term of $\Delta\rho$ is

$$\Delta\rho=\frac{\sqrt{2}G_F}{16\pi^2}\sum_f N_c^f\Delta m_f^2+\cdots, \quad (17)$$

where the sum extends over all fermion isodoublets f; $\Delta m_f^2=|m_{f1}^2-m_{f2}^2|$ is the isodoublet mass splitting. The correction $\Delta\rho$ is then sensitive to all possible $\mathrm{SU}(2)_L$ multiplets that couple to gauge bosons and that exhibit large mass splitting; hence it is very sensitive to new heavy particles.

Among the known fermion isodoublets the largest contributor to $\Delta\rho$ is the top-bottom isodoublet:

$$\Delta\rho\sim\Delta\rho_{tb}\sim3\frac{\sqrt{2}G_F m_t^2}{16\pi^2}=0.0099\left(\frac{m_t}{175\,\mathrm{GeV}}\right)^2. \quad (18)$$

The leading top contribution to Δr is amplified by a factor $c_W^2/s_W^2\sim3.5$ and amounts to -0.0349 ± 0.0023 for $m_t=175.6\pm5.5$ GeV.

Light fermions contribute to the last term in Eq. (16) with $\Delta r_{\mathrm{rem}}^{\mathrm{leptons}}\simeq0.0015$ and $\Delta r_{\mathrm{rem}}^{\mathrm{quarks}}\simeq0.0040$, while the top quark contributes with non-negligible logarithmic terms that give $\Delta r_{\mathrm{rem}}^{\mathrm{top}}\simeq0.0069$.

At one-loop radiative corrections there is no quadratic Higgs mass dependence in $\Delta\rho$. This is due to the accidental $\mathrm{SU}(2)_R$ symmetry of the Higgs sector in the MSM, which implies $\rho=1$ at tree level (Veltman screening). The leading contribution of the Higgs boson, which is only logarithmic, is split into two terms, one appearing in $\Delta\rho$ and the other in Δr_{rem}. Provided that $M_H^2\gg M_W^2$, the Higgs boson contribution is

TABLE I. Errors for the most precisely measured electroweak observables. Theoretical errors are assigned by the quoted uncertainty on the input parameters of the minimal standard model for the most precisely measured electroweak observables. All errors are in per mill. The two variations for the Higgs boson mass are computed against a reference value of 300 GeV. The last column shows the errors due to the intrinsic theoretical accuracy.

Observable	Expt. error	m_t ±6 GeV	M_H 70	M_H 1000 GeV	α_s ±0.003	$\alpha(M_Z^2)^{-1}$ ±0.09	Theor. errors
Γ_Z	1.0	0.6	+1.7	−2.1	0.7	0.3	0.2
Γ_ℓ	1.2	0.7	+1.3	−1.7	–	0.2	0.2
R_ℓ	1.3	–	+0.7	−0.6	1.0	0.2	0.2
R_b	4.1	0.9	−0.2	0.0	–	–	0.4
$\sin^2\theta_{\rm eff}^\ell$	1.0	0.8	−3.7	+3.0	–	1.0	0.4
M_W	1.0	0.5	+1.3	−1.2	–	0.2	0.1

$$\Delta r^{\rm Higgs} \simeq \frac{\sqrt{2} G_F M_W^2}{16\pi^2}\left\{\frac{11}{3}\left(\ln\frac{M_H^2}{M_W^2}-\frac{5}{6}\right)\right\}$$
$$= 0.0025\left(\ln\frac{M_H^2}{M_W^2}-\frac{5}{6}\right) \quad (19)$$

and amounts to 0.0045 for $M_H = 300\,\text{GeV}$.

The numerical prediction for Δr given in this section and the measured value of the W mass given in Sec. V can be compared using Eq. (14). This exercise is a simple—and to some extent approximate—example of the procedure used throughout this report. Using $M_W = 80.43 \pm 0.08\,\text{GeV}$ and Eq. (14) and taking into account the dependence of s_W^2 on M_W, one obtains

$$\Delta r = 0.0326 \pm 0.0051.$$

This value can be compared with the predictions for the various terms in Eq. (16):

$$\Delta r \simeq \Delta\alpha - \frac{c_W^2}{s_W^2}\Delta\rho_{tb} + \Delta r_{\rm rem}^{\rm leptons} + \Delta r_{\rm rem}^{\rm quarks} + \Delta r_{\rm rem}^{\rm top} + \cdots + \Delta r^{\rm Higgs},$$
$$\Delta r \simeq 0.0632 - 0.0349 \pm 0.0023 + 0.0124 + \cdots + 0.0025\left(\ln\frac{M_H^2}{M_W^2}-\frac{5}{6}\right),$$

where only the largest error has been shown. The dots indicate that some non-negligible terms compared to the quoted error are still missing. The comparison gives

$$0.0025\left(\ln\frac{M_H^2}{M_W^2}-\frac{5}{6}\right) \simeq -0.0081 \pm 0.0056,$$

that is, equivalent to $\ln(M_H/M_W) \simeq -1.16 \pm 1.12$. Unfortunately, this result corresponds to a relatively light Higgs boson mass, for which the approximation (19) does not hold. By replacing the left-hand side of Eq. (19) with the exact form (Burgers *et al.*, 1990) of $\Delta r^{\rm Higgs}$, one obtains a central value of $\ln(M_H/M_W) \simeq -0.33$ and an upper bound on the Higgs mass of about 350 GeV at 95% confidence level.

C. Precision of the MSM calculations including radiative corrections

The predictions for the electroweak observables are computed in the minimal standard model as a function of the parameters of the model using computer codes that implement the radiative corrections described in the previous sections. The most commonly used electroweak libraries are those of Burgers *et al.* (1990) and Bardin *et al.* (1992). Uncertainties can originate from two different sources in the theoretical prediction: errors on the input parameters, discussed in the next section, and the limitation of the calculation itself, often called "intrinsic theoretical accuracy."

Predictions for the electroweak observables are computed up to a certain order in the perturbative expansion and have limited precision, estimated by inferring the size of the next missing order in the calculation.

The precision of the electroweak libraries has improved in the last few years with the resummation of known leading one-loop terms, calculations of leading terms from genuine two-loop electroweak corrections, and studies of the interplay between QCD and electroweak corrections. The estimates of theoretical uncertainties are to some extent subjective, and their values partly reflect the philosophy underlying implementation of radiative corrections in a given scheme. Bardin *et al.* (1995) studied the quantification of these uncertainties in detail arriving at the following conclusions:

(i) The differences between results of different computational schemes are small compared to present experimental uncertainties.

(ii) In many cases the one-loop approximation in the electroweak gauge coupling is adequate at the present level of experimental accuracy. Recently, a complete evaluation of the sub-leading $O(G_F^2 M_Z^2 m_t^2)$ corrections was performed by Degrassi *et al.* (1996), and the estimated theoretical uncertainties were found to be significantly reduced.

The intrinsic theoretical error in the prediction of the most relevant electroweak observables is shown in Table

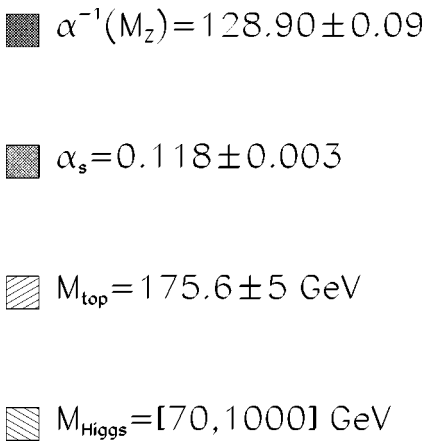

FIG. 3. Ranges for the input parameters of the minimal standard model.

I. The values quoted are the largest differences found by Bardin *et al.* (1995), which may be considered a rather conservative estimate. They are typically smaller than the experimental accuracy and the uncertainty induced by errors on the input parameters.

D. Dependence of the MSM predictions on the input parameters

The predictions of the minimal standard model for six relevant electroweak observables are shown in Figs. 4 and 5 as a function of the input value of m_t and M_H. The range of m_t is arbitrarily set between 150 and 200 GeV and that of M_H between 60 and 1000 GeV. The range of the observables is set to about $\pm 5\sigma$ of the present experimental accuracy. With this choice the slopes of the predictions give the relative sensitivity of the various measurements to m_t or M_H. In the calculation the values of the other known input parameters is fixed to their central value and that of M_H to 300 GeV. The hatched band in the plots reflects the error on the prediction induced by uncertainties on the other input parameters, with a hatching code, shown in Fig. 3, that will be extensively used in this report.

These predictions depend on the masses of the fermions and on M_H according to a complex pattern requiring flavor-dependent corrections described in the previous sections. However, the leading dependence of one-loop corrections is similar in most observables.

Leaving aside the $\Delta\alpha$ correction, which does not depend on m_t and M_H, there are four numerically relevant loop contributions: the three vacuum polarization corrections Δr, Δk, and $\Delta\rho$ and the $Z\to b\bar{b}$ vertex correction. All four quantities depend quadratically on the top mass, and the first three also depend logarithmically on the Higgs mass.

The leading terms in the vacuum polarization corrections are

$$\Pi^W \to 1+\Delta r \simeq 1+\Delta\alpha-\frac{c_W^2}{s_W^2}\Delta\rho+\cdots,$$

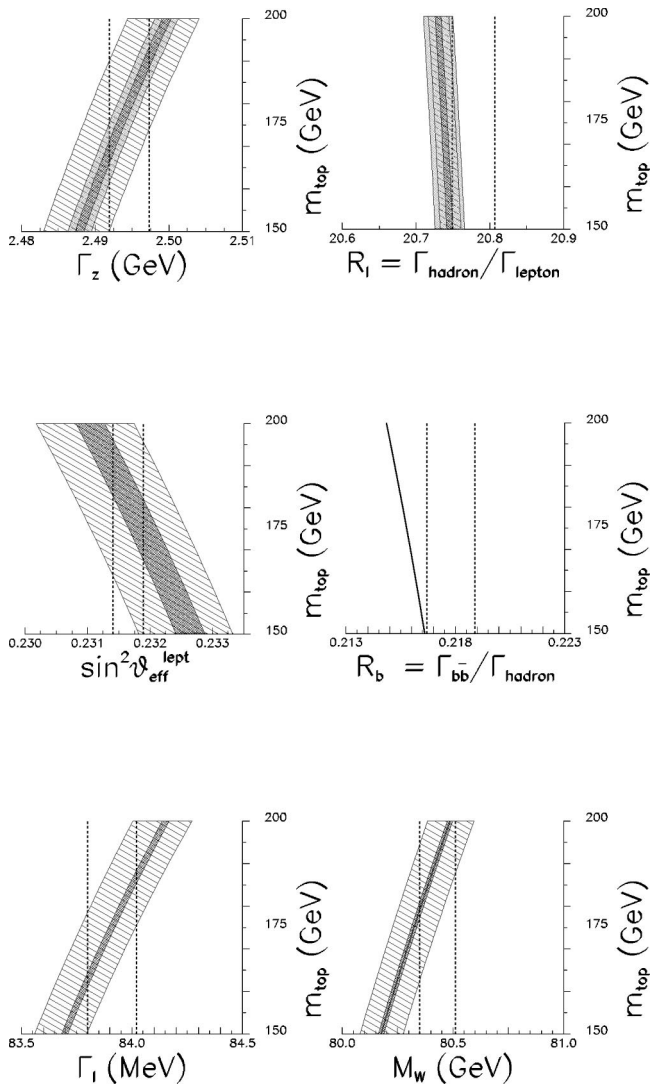

FIG. 4. Dependence on m_t of the predictions for six electroweak observables. The vertical dotted lines indicate the $\pm 1\sigma$ of the present experimental accuracy. The band indicates the error on the prediction due to uncertainties in other input parameters. The hatching code is described in Fig. 3.

$$\Pi^{\gamma Z} \to 1-\Delta\kappa \simeq 1-\frac{c_W^2}{s_W^2}\Delta\rho+\cdots, \tag{20}$$

$$\Pi^Z \to \overline{\rho}(s) \simeq 1+\Delta\rho+\cdots.$$

They all depend on the same quantity, $\Delta\rho$, and therefore have similar leading top dependence. Moreover the contributions of the top and the Higgs masses can only be disentangled at the sub-leading level. The dependence on M_H of the vertex corrections is negligible, since the coupling of the light fermions to the Higgs boson is small. The dependence on the top mass is only relevant for the $Z\to b\bar{b}$ vertex due to the large Kobayashi-Maskawa coupling V_{tb}.

For the above reasons the predictions of the total Z width, Γ_Z, and of the width of the Z in leptons, Γ_ℓ, in Figs. 4 and 5 show a dependence on m_t and M_H similar to the prediction of M_W. The prediction of the effective sine $\sin^2\theta^{\ell}_{\rm eff}$ also has a similar dependence, but with the

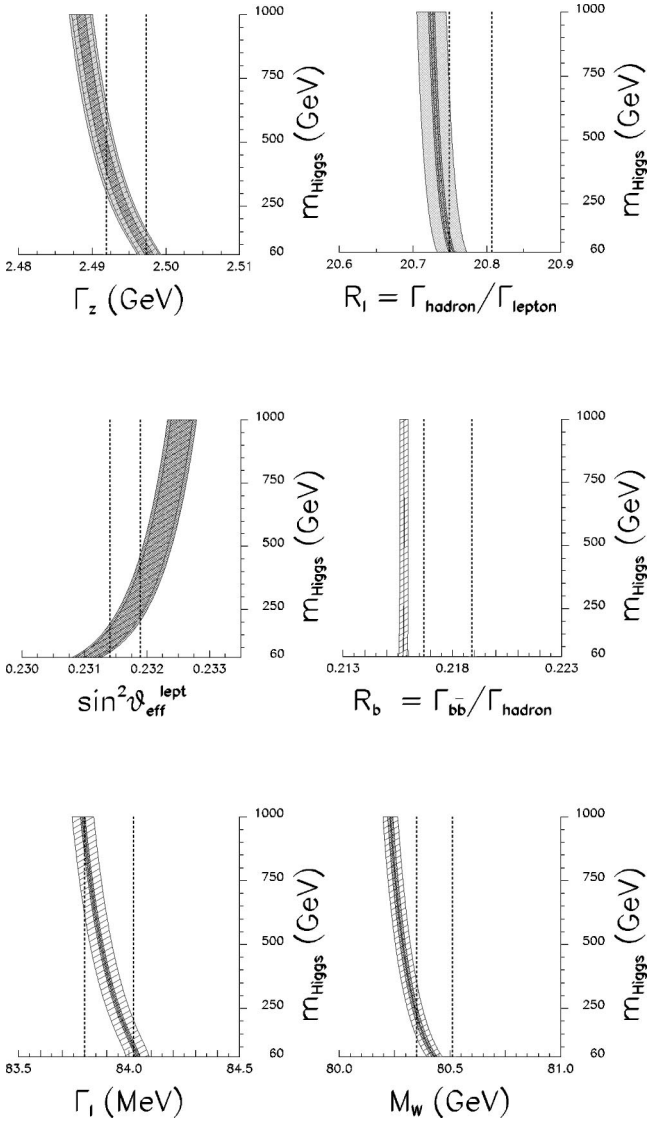

FIG. 5. Dependence on M_H of the predictions for six electroweak observables. The vertical dotted lines indicate the $\pm 1\sigma$ of the present experimental accuracy. The band indicates the error on the prediction due to uncertainties in other input parameters. The hatching code is described in Fig. 3.

opposite sign. The prediction for the ratio R_b of $b\bar{b}$ to hadrons in the Z partial width does not depend appreciably on the vacuum polarization correction—because its leading contributions cancel in the ratio. This ratio depends on m_t via the vertex corrections and is independent of M_H in one-loop order. The ratio R_ℓ of leptons to hadrons is also predicted to be almost independent of the vacuum polarization: its mild dependence on m_t comes mainly from vertex corrections to the Z decays into $b\bar{b}$, which contribute to $\Gamma_{\rm had}$.

The uncertainty on the prediction caused by our limited knowledge of the MSM input parameters is shown in Table I. The prediction for R_ℓ is affected mainly by the error on α_s since its dependence on m_t and M_H is very mild. The prediction of R_b is affected only by the uncertainty on m_t, and for this reason the prediction as a function of the top mass is very accurate, as is shown in Fig. 4. The predictions for the other observables are affected mainly by uncertainties on the top and the Higgs masses. The error induced by $\alpha(M_Z^2)$ is always smaller than the experimental error except in the case of the measurement of $\sin^2\theta^{\ell}_{\rm eff}$, where the two errors are of comparable size. At present precision $\sin^2\theta^{\ell}_{\rm eff}$ is also the variable most sensitive to the top and the Higgs masses.

Since the errors on the predictions induced by the uncertainties on M_H, m_t, and α_s are often larger than, or of the same size as, the experimental error, an overall fit of the electroweak observables can further constrain these quantities.

E. LEP and its detectors

LEP is CERN's Large Electron Positron collider. It is located between the Jura mountains and Lake Geneva in a 26.7-kilometer-long, 3.8-meter-wide underground tunnel situated between 50 and 170 meters below the surface. From its startup in 1989 until 1995 it was used to produce electron-positron collisions at a center-of-mass energy close to the Z mass.

The accelerator consists of eight 2.8-kilometer-long arcs linked by eight straight sections. The particles are kept on their orbit in the arcs by 3400 bending magnets and are focused by 800 quadrupoles and 500 sextupoles. In the first phase (LEP1), electrons and positrons were accelerated by copper radio-frequency accelerating cavities located in two diametrically opposite positions in straight sections on either side of the underground experimental halls. The radio-frequency system is being upgraded for the second phase (LEP2) with the installation of superconducting cavities; work on the upgrade started in fall 1995 and will be completed by 1998 when the beam energy will eventually reach almost 100 GeV. The threshold for the production of W pairs was crossed in 1996. The energy of the LEP beams has been precisely calibrated with the resonant depolarization method.

Electrons and positrons circulate in bunches of some 10^{11} particles with a revolution time of 88.92 μs. They collide at four interaction points, producing a luminous region approximately $300\times60\times2000$ $\mu{\rm m}^3$, where the three numbers refer to the directions along the bending radius, perpendicular to the bending plane, and along the beams. LEP luminosity increased over the years, with improved optics and bunch schemes. The record luminosity in the Z runs was $2.3\,10^{31}\,{\rm cm}^{-2}\,{\rm s}^{-1}$ and luminosities in excess of $1.5\,10^{31}\,{\rm cm}^{-2}\,{\rm s}^{-1}$ were usually achieved in the last years of operation.

Four large underground halls, 70 m long and 23 m in diameter, house the four detectors ALEPH, DELPHI, L3, and OPAL.[2]

[2]ALEPH: Apparatus for LEP PHysics; DELPHI: DEtector with Lepton, Photon, and Hadron Identification; L3: So named because it was the third letter of intent; OPAL: Omni Purpose Apparatus for LEP.

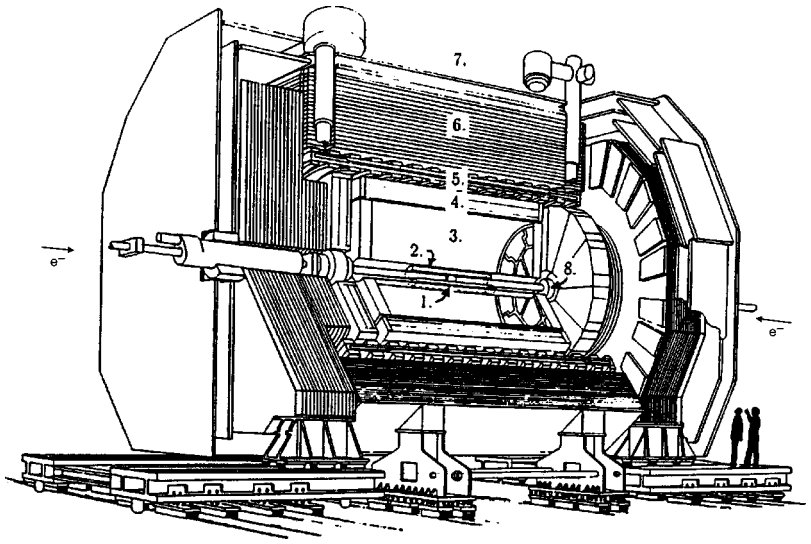

FIG. 6. Cut-away view of the ALEPH detector showing the main detector elements: (1) silicon vertex detector; (2) inner trigger chamber; (3) time projection chamber; (4) electromagnetic calorimeter; (5) superconducting coil; (6) hadron calorimeter; (7) muon chambers; (8) luminosity monitors.

The layout of each detector follows a basic pattern (see Fig. 6). Starting from the beam pipe, one finds a vertex detector, tracking chambers, electromagnetic calorimetry, hadron calorimetry, and a muon detector. Each detector also includes a magnet, to provide the field for measurement of the charge and momentum of charged particles, and a forward calorimeter to monitor the luminosity.

ALEPH is a general-purpose detector (ALEPH, 1990; ALEPH, 1995b). It has a 1.8-m-radius time projection chamber (TPC) in a magnetic field of 1.5 T produced by a superconducting solenoid. The TPC is surrounded by a fine-grain electromagnetic calorimeter for identifying electrons and photons in dense jets and measuring energy depositions with very good spatial resolution. Muons are identified by the instrumented hadron calorimeter and by the external muon chambers.

The main tracking element of the DELPHI detector (DELPHI, 1991) is also a TPC. It is surrounded by ring-imaging Cherenkov counters (RICH), using the Cherenkov effect in a novel way to identify the various types of particles produced. A high-density projection chamber (HPC) is used for fine-grain electromagnetic calorimetry. All these elements are immersed in a magnetic field of 1.2 T, produced by a superconducting solenoid with a cryostat of 2.6-m internal radius.

The OPAL detector (OPAL, 1991b) was designed using well tested detector techniques. The central detector is a cylindrical chamber of 2-m radius surrounded by a lead glass electromagnetic calorimeter, with the coil of the magnet in the annular space between them. The magnetic field of 0.43 T is produced by a warm solenoid.

The L3 detector (L3, 1990) differs from the other detectors in that the coil of the magnet surrounds the whole detector. The central tracker is a 1-m-radius time expansion chamber (TEC) and the electromagnetic calorimetry is provided by crystals of bismuth germanium oxide (BGO), which ensure a very precise measurement of the energies of photons and electrons. Jet energies are precisely measured by the hadron calorimeter, which has uranium absorbers. The muon momentum is precisely measured, since muons are tracked over about 4 m inside the magnetic field of 0.5 T.

During the years 1989–1995 LEP delivered an integrated luminosity of about $200\,\mathrm{pb}^{-1}$ to each of the four experiments. About 80% of this integrated luminosity was delivered at a center-of-mass energy in a range of $\pm 100\,\mathrm{MeV}$ around the Z mass. The remaining 20% was used to scan the resonance. The statistics used by each experiment in the analysis of the Z line shape are shown in Table II. In total, the four experiments collected about 15 million Z decays into hadrons and more than 1.6 million Z decays into leptons.

F. SLC and SLD

The 3.2-kilometer-long linear electron-positron collider SLC (Stanford Linear Collider) started its operation in 1989 at a center-of-mass energy close to the Z mass. In 1993 a new source (Maruyama *et al.*, 1992; Alley *et al.*, 1995) of polarized electrons was commissioned based on an electron gun with a GaAs strained cathode providing electrons with about 90% polarization at a rate of 120 Hz, with the possibility of reversing the spin at each pulse.

SLC operates at a lower luminosity than LEP but takes advantage of the polarized electron beam and of the very small dimensions (a few microns) of the luminous region in the directions perpendicular to the beams.

The SLD detector (SLD, 1984) was installed at the SLC interaction point in 1990. It has a general layout similar to that in the LEP experiments, with very precise vertexing capabilities provided by a 3D silicon charge-couple device system. The tracking is provided by a wire

TABLE II. The LEP statistics in units of 10^3 events used for the analysis of the Z line shape and lepton forward-backward asymmetries. Not all experiments have used the full 1995 data set for the present results.

		ALEPH	DELPHI	L3	OPAL	LEP
$q\bar{q}$	'90-'91	451	357	416	454	1678
	'92	680	697	678	733	2788
	'93 prel.	640	677	646	646	2609
	'94 prel.	1654	1241	1307	1524	5726
	'95 prel.	739	584	311	344	1978
	total	4164	3556	3358	3701	14779
$\ell^+\ell^-$	'90-'91	55	36	40	58	189
	'92	82	70	58	88	298
	'93 prel.	78	74	64	82	298
	'94 prel.	190	135	127	184	636
	'95 prel.	80	67	28	42	217
	total	485	382	317	454	1638

chamber and particle identification by the Cherenkov ring-imaging technique. The polarization of the electron beam is measured with a polarimeter based on the Compton scattering.

The SLC has delivered to the SLD an integrated luminosity of about 8 pb^{-1} corresponding to 20 000 Z decays with 22% polarization, 50 000 Z decays with 63% polarization, and 150 000 Z decays with 77% polarization.

II. THE Z LINE SHAPE

The Z line-shape parameters (mass M_Z, total width Γ_Z, and partial widths) have been precisely determined by measuring the leptonic and hadronic cross sections at different center-of-mass energies around the nominal value of the Z mass.

The measured cross sections are fitted to a formula that depends on the Z parameters and takes into account the important effects of initial-state radiation. The absolute scale of the Z mass and widths is given by the precise calibration of the center-of-mass energy at the collision points.

A. The fitting formula

The interpretation of the measured cross sections in terms of the Z parameters requires a careful treatment of the effects induced by initial-state radiation [see Fig. 1 (a)]. These effects are very large: the QED radiative corrections reduce the μ-pair-production cross section at the Z peak by more than 30%.

The cross section for the process $e^+e^-\to f\bar{f}$, $f\neq e$, corrected with first-order initial-state radiation, is (Bonneau and Martin, 1971)

$$\sigma_1(s)=\sigma_0(s)(1+\delta_1+\beta\ln x_0)+\int_{x_0}^{1}\beta\left(\frac{1}{x}-1+\frac{x}{2}\right)\sigma_0(s')dx, \tag{21}$$

where s and $s'=s(1-x)$ are the square of the e^+e^- center-of-mass energy before and after initial-state radiation and x is the photon energy in units of the beam energy. The term x_0 is an arbitrary cutoff parameter used to split the corrections between those due to virtual and soft photons and those due to hard-photon emission; δ_1 ($\sim 9\%$) accounts for the part of the virtual and soft corrections independent of the infrared singularity; and β is defined as $\beta\equiv(2\alpha/\pi)[\ln(s/m_e^2)-1]\simeq 0.11$, at LEP energies. The second term of Eq. (21) is the convolution of the photon spectrum with the cross section at the center-of-mass energy remaining after initial-state radiation. Since $\sigma_0(s)$ decreases rapidly away from the Z pole, the upper limit of the integral in Eq. (21) is effectively taken at $x_M\sim\Gamma_Z/\sqrt{s}$. The cross section can be then approximated by

$$\sigma_1(s)\sim\sigma_0(s)[1+\delta_1+\beta\ln(\Gamma_Z/M_Z)] \tag{22}$$

for $s\sim M_Z^2$. Due to the large negative term $\beta\ln(\Gamma_Z/M_Z)\sim -40\%$, the overall correction is around -30%. Well below the Z resonance there is no cutoff in the integral, and the dominant correction is δ_1.

In conclusion, QED radiative corrections are large because in the vicinity of the Z pole the radiation of hard photons from the initial state is strongly suppressed, leaving the colliding e^+e^- system with too little energy to produce a Z. Then the real photon radiation cannot compensate for the large negative correction due to virtual-photon effects.

The first-order cross section of Eq. (21) has been complemented with complete initial-state radiation $\mathcal{O}(\alpha^2)$ radiative corrections (Berends *et al.*, 1987). Furthermore, the leading soft-photon effects have been introduced to all orders in exponentiated form (Jadach and Ward, 1988). Figure 7 shows the theoretical prediction for the Z line shape through successive approximations.

All initial-state radiative corrections are included in a radiator function $H(s,s')$. The measured cross sections are fitted using a formula that convolutes a reduced cross section $\hat{\sigma}$, a function of the Z parameters, with $H(s,s')$:

$$\sigma_{f\bar{f}}(s)=\int_{4m_f^2}^{s}ds'H(s,s')\hat{\sigma}_{f\bar{f}}(s'). \tag{23}$$

The expression for the radiator function can be found in the article of Bardin *et al.* (1995). It is peaked at $s'=s$ and has a long tail toward lower values of s'.

The reduced cross section[3] $\hat{\sigma}$ is

$$\hat{\sigma}_{f\bar{f}}(s)=\sigma_{f\bar{f}}^{\text{peak}}\frac{s\Gamma_Z^2}{(s-M_Z^2)^2+\left(\frac{s\Gamma_Z}{M_Z}\right)^2}+\text{``}(\gamma-Z)\text{''}+\text{``}|\gamma|^2\text{''}. \tag{24}$$

The first term includes the relativistic Breit-Wigner distribution corresponding to the Z exchange. The photon

[3]The explicit MSM formula for the reduced cross section in terms of the effective couplings is given in the Appendix.

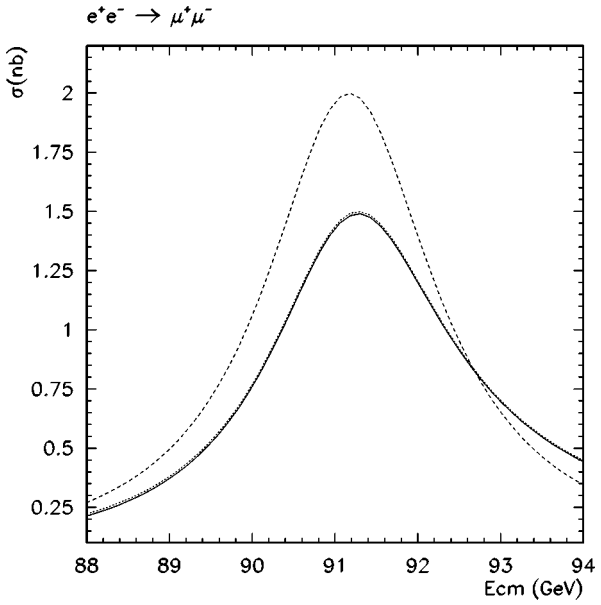

FIG. 7. Effect of QED initial-state radiative corrections on the muon-pair-production cross section near the Z pole: Dashed line, cross section without initial-state radiation; dotted line, $\mathcal{O}(\alpha)$ exponentiated initial-state radiation; solid line, $\mathcal{O}(\alpha^2)$ exponentiated initial-state radiation.

term $|\gamma|^2$ is only a few percent of the Z term and is fixed in the fit to the QED prediction. The interference term $(\gamma-Z)$ is even smaller and is zero when $s=M_Z^2$. It is fixed in the fit to the MSM prediction. If the interference term is fitted, the error on the Z mass increases substantially (see Sec. II.F), since this term has opposite sign on the two sides of the Z peak. In the case of Bhabha scattering, $f=e$, the t-channel photon-exchange and Z-exchange diagrams have to be added. They are fixed in the fit to the MSM prediction, defined as the difference between the MSM cross sections for $f=e$ and $f=\mu$.

The cross section at the peak can be written in terms of the Z mass and width and the Z partial widths to the initial state, Γ_e, and the final state, Γ_f, as

$$\sigma_{ff}^{\text{peak}}=\sigma_{ff}^{0}\left(\frac{1}{1+\delta_{\text{QED}}}\right)=\frac{12\pi}{M_Z^2}\frac{\Gamma_e\Gamma_f}{\Gamma_Z^2}\frac{1}{1+3\alpha/4\pi}. \quad (25)$$

Here Γ_f represents the partial width of the Z decay into the fermion pair $f\bar{f}$ and includes by definition all radiative corrections. Since the initial-state radiation is taken into account by the convolution procedure, the contribution of the QED final-state radiative corrections δ_{QED} is removed from the initial-state width Γ_e, thus avoiding a double counting.

In the study of the Z line shape all hadronic decays of the Z are counted together, irrespective of the final-state flavor, and the partial decay width into hadrons Γ_h is measured. The decays into charged lepton pairs can easily be separated, and the three leptonic partial widths Γ_e, Γ_μ, and Γ_τ are measured. The constraint that the three leptonic widths be equal, after small corrections for mass effects, is used to increase the sensitivity of the fit. In this case—lepton universality—the leptonic width is called Γ_ℓ and corresponds to the width of any single flavor as if it were massless. With the lepton universality assumption, four parameters are needed to describe the s dependence of the hadronic and leptonic cross sections. The set of parameters used is M_Z, Γ_Z, the ratio of hadronic to leptonic partial widths $R_\ell=\Gamma_h/\Gamma_\ell$, and the hadronic peak cross section σ_h^0. These parameters have small correlations. If lepton universality is not assumed, R_ℓ is replaced by three analogous quantities, R_e, R_μ, R_τ.

This scheme is implemented in two computer programs that are used by the LEP collaborations to fit their data: MIZA (Martinez *et al.*, 1991) is used by the ALEPH collaboration and ZFITTER (Bardin *et al.*, 1992) by DELPHI, L3, and OPAL. At the current level of experimental precision, the results obtained with the two programs are equivalent. The overall precision of the treatment of the initial-state radiation for the computation of the total cross section is about 0.06% (Martinez *et al.*, 1991). For differential cross sections, a few modifications are needed, and the accuracy is slightly worse.

B. Cross sections

A cross section σ_i of a given process i is measured by selecting and counting the number N_i of events of type i, correcting them for the contribution of background events N_{bk}^i and the selection efficiency ϵ_i, and normalizing them to the integrated luminosity L:

$$\sigma_i=\frac{N_i-N_{bk}^i}{\epsilon_i L}. \quad (26)$$

1. Luminosity determination

The luminosity L is measured using Eq. (26) for a process with known cross section σ_i. At LEP the Bhabha scattering process $e^+e^-\to e^+e^-$ is used, giving

$$L=\frac{N_{bh}-N_{bk}^{bh}}{\epsilon_{bh}\sigma_{bh}^{th}}.$$

Bhabha scattering is chosen because the cross section is large and is dominated by t-channel photon exchange, a well-understood QED process. To obtain a precise measurement of the luminosity, the background N_{bk}^{bh} has to be small and under control, the efficiency ϵ_{bh} has to be high and well known, and the theoretical cross section σ_{bh}^{th} has to be computed precisely.

Before LEP, the standard accuracy in the determination of the luminosity was of the order of 2–5%. Imperfect knowledge of the absolute efficiency was the main contribution to the overall uncertainty. To compute the efficiency precisely, one needs to know the position $R_{\min}$ of the inner edge of the detector with respect to the beam. The Bhabha cross section can then be approximated as

$$\sigma_{\rm bh}^{\rm th} \sim \frac{16\pi\alpha^2}{s}\left(\frac{1}{\theta_{\rm min}^2}-\frac{1}{\theta_{\rm max}^2}\right),$$

where $\theta_{\rm min}$ and $\theta_{\rm max}$ are the polar angles defining the inner and outer acceptances, respectively. In a first approximation, $\Delta\sigma/\sigma \simeq 2\Delta\theta_{\rm min}/\theta_{\rm min} \simeq 2\Delta R_{\rm min}/R_{\rm min}$.

The typical luminosity detector for a LEP experiment consists of two cylindrical calorimeters located at low angles on either side of the interaction point. Some of them have a tracking device in front, to help in the position measurement. If this is not available, fine granularity in the calorimeter is mandatory.

The first-generation LEP luminosity monitors had inner radii of the order of 100 mm. The overall precision of the luminosity measurement, dominated by the systematic error, was around 2% at startup, improving later to 0.5%

All four experiments upgraded their luminometers between 1992 and 1994. Excellent mechanical precision of the order of 20 μm was achieved in controlling the position of the inner edge of the detectors. For typical values of $R_{\rm min}$ around 60 mm for the second generation detectors, these 20 μm correspond to an uncertainty in the luminosity $\Delta L/L \simeq 2\Delta R_{\rm min}/R_{\rm min} \simeq 7\times10^{-4}$.

To control θ precisely, both the detector position and the position of the luminous region have to be well understood. The sensitivity of the luminosity to the relative position between beam and detector can be largely removed by appropriately choosing the event selection cuts (ALEPH, 1992b). Independence from transverse misalignments is achieved by defining different fiducial regions in the two calorimeters on either side of the interaction point. The difference in size between the two regions has to be more than twice the maximum expected misalignment. If the definition of loose and tight is changed from one side to the other randomly, on an event by event basis, the dependence on longitudinal misalignments is also largely cancelled.

The selection procedure requires two almost back-to-back energy depositions in the luminosity calorimeters in excess of some threshold energy. Then the cuts defining the fiducial regions (''tight'' or ''loose'') are applied. In most cases, the precise radial cut is defined studying the energy asymmetry across calorimeter pad boundaries, rather than by using center-of-gravity type algorithms. The former are more precise and less dependent on detector simulations. The L3 experiment takes advantage of the tracker in front of the calorimeter to define the radial cut.

The main background to the Bhabha reaction comes from random coincidences of off-momentum electrons and positrons. These can be measured directly from the data using samples obtained through downscaled low-energy triggers and studying acoplanar coincidences. Background levels are below the per-mill level and their contribution to the systematic error is very small. The overall experimental error is between 0.07% and 0.1%, depending on the experiment. Usually the tolerances in the mechanical structure determine the largest uncertainty. Since these errors are not correlated among experiments, the combined LEP experimental error is close to 0.05%.

All experiments use calorimeters to define the acceptance, and photons radiated almost collinearly with the outgoing electrons and positrons are not separated. Their effect has to be taken into account in the computation of the theoretical cross section, for which the BHLUMI program (Jadach and Ward, 1989; Jadach *et al.*, 1992) is generally used. BHLUMI includes multiphoton radiation by the Yennie-Fraustchi-Suura (Yennie *et al.*, 1961) mechanism from the dominant diagram, with a photon exchanged in the t channel. The overall precision of the Bhabha cross-section calculation is estimated to be 0.11% (Jadach and Ward, 1996), the main uncertainty coming from missing sub-leading $\mathcal{O}(\alpha^2 L)$ corrections (Arbuzov *et al.*, 1996; Jadach *et al.*, 1997), where $L=\log(-t/m_e^2)$.

2. Hadronic cross section

About 70% of the Z bosons produced decay to a $q\bar{q}$ pair which fragments, producing a multihadronic final state. These events carry most of the weight in the lineshape analysis. They can be easily selected by exploiting their multiparticle structure and their large visible energy.

The four experiments select hadronic events requiring a minimum number of clusters in the calorimeters [of $\mathcal{O}(10)$], with a minimum energy around 10–20% of the center-of-mass energy (ALEPH, 1994d; DELPHI, 1994b; L3, 1994c; OPAL, 1994a). ALEPH and DELPHI also use their time projection chambers to have independent selections, asking for a minimum number of charged-particle tracks (around five) with a minimum charged energy (around 10% $\sqrt{s}$). Acceptances are large, between 97% and 99.5% in the whole solid angle. Inefficiencies are due only to low-multiplicity events going down the beam pipe. Backgrounds are low, below 1%, and come mainly from tau-pair events and the so-called two-photon events, in which two quasireal photons radiated from the incoming beams collide at low q^2.

Since the ratio of hadronic to leptonic cross sections is around 21 at the Z peak, in contrast with values below 4 at PEP/PETRA energies, the selection of hadronic events at LEP is easier. Each experiment accumulated about four million hadronic Z decays, resulting in statistical errors below one per mill for the peak cross section.

The measured cross sections are corrected for the spread of the center-of-mass energy ($\epsilon_{\rm CMS} \sim 56$ MeV):

$$\delta\sigma \simeq -0.5\frac{d^2\sigma}{dE^2}\epsilon_{\rm CMS}^2, \tag{27}$$

which causes an apparent reduction of the cross section of 1.1 per mill at $\sqrt{s}=M_Z$ and an apparent increase of 0.5 per mill at ± 2 GeV from the Z peak. The center-of-mass energy spread is determined with a precision of 2.5% from the measurements of the bunch length at the

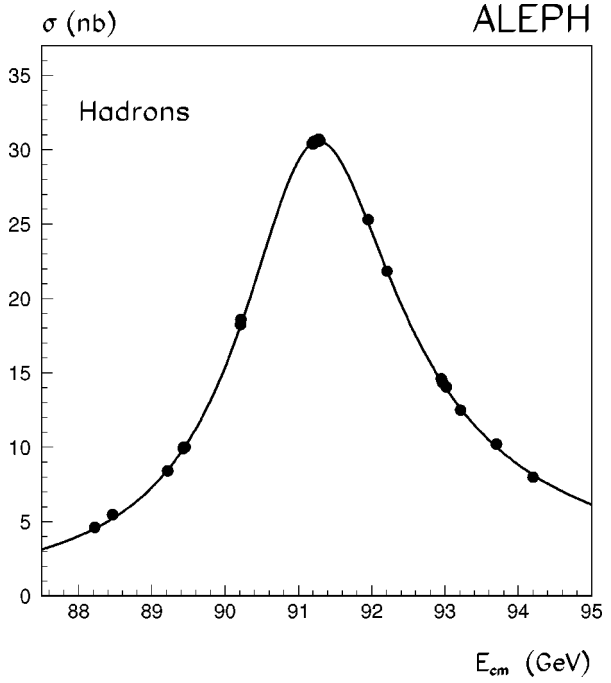

FIG. 8. Hadronic cross section as a function of center-of-mass energy as measured by the ALEPH Collaboration (1994d). The solid line represents the minimal-standard-model fit to the data.

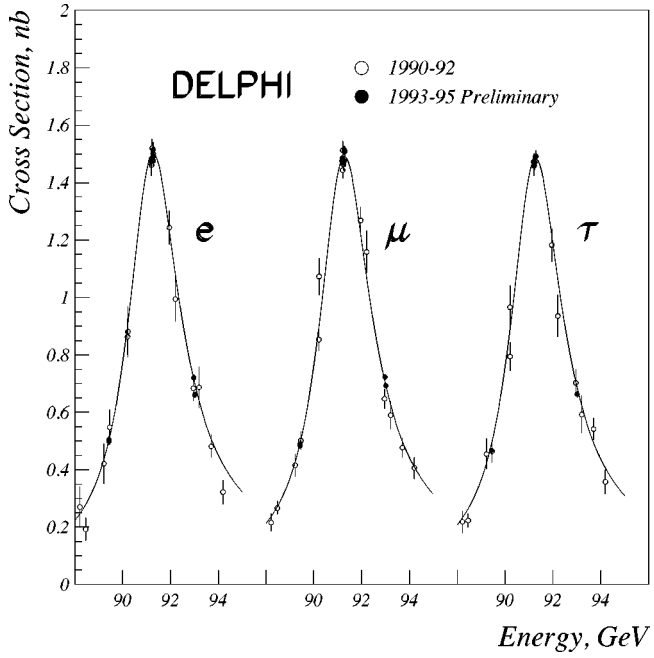

FIG. 9. Leptonic cross sections as a function of center-of-mass energy as measured by the DELPHI Collaboration (1994b). The solid lines represents the MSM fit to the data.

collision points and the incoherent synchrotron oscillation tune of the machine (Lançon and Blondel, 1996).

The main systematic errors are due to the understanding of the two-photon background. Since the two-photon cross section is not resonating, the relative contamination is higher at off-peak energies, affecting the measurement of the Z width. Overall systematic errors range from 0.5 to 1.6 per mill, depending on the experiment. Figure 8 shows the hadronic cross sections measured by the ALEPH collaboration.

3. Leptonic cross sections

Charged-lepton pair decays of the Z account for only 10% of the Z decays. However, they allow the precise determination of the electroweak couplings of individual leptons to the Z.

Lepton selections vary in each experiment, but they are typically based on the criteria of low multiplicity and high visible energy or momentum (ALEPH, 1994d; DELPHI, 1994b; L3, 1994c; OPAL, 1994a). Electron pairs are further identified by the energy deposited in the electromagnetic calorimeters, and muon pairs are identified by their penetration through the dense hadron calorimeters. A variety of methods have been developed to identify tau pairs, using, among other criteria, the missing mass of the event. Some experiments tag tau pairs, vetoing electron and muon pairs from their low-multiplicity event sample.

Efficiencies within the detectors' geometrical acceptances are high, from around 85% for taus to above 95% for electrons and muons. The geometrical acceptance is around 85%, defined by a cut on the production angle. It is corrected for with the help of Monte Carlo (Jadach *et al.*, 1993, 1994) simulations. The cross section for the Bhabha scattering is usually measured for $\cos\theta<0.7$, where θ is the polar angle of the scattered electron: the loss of statistics is compensated for by a significant reduction of the systematic error on the Z parameters, caused by the subtraction of the t-channel contribution.

Backgrounds from two-photon events are only relevant for tau pairs ($\sim 2\%$). Otherwise, the main background consists of lepton-pair events of different flavor. ALEPH and DELPHI have measured the cross section for all charged leptons together and achieved purer dilepton samples. Altogether, each collaboration accumulated between 300 and 400 thousand Z decays into charged leptons during the period 1989–1995.

As in the hadronic cross section, the measured leptonic cross sections are corrected for the effect of the center-of-mass energy spread; see Eq. (27).

Systematic errors are below 0.5% for all species and experiments. Reliability of detector simulations (for electrons and muons) and background contamination (for taus) are the main components. The three leptonic cross sections as measured by the DELPHI collaboration are shown in Fig. 9.

C. LEP energy calibration

The measurements of the mass and width of the Z boson at LEP rely on precise knowledge of the average center-of-mass energy at the collision points. During the 1993 and 1995 energy scans the luminosity was collected at three scan points (named peak-2, peak, and peak $+2$) separated by roughly 1790 MeV, almost symmetrically placed around the energy corresponding to the

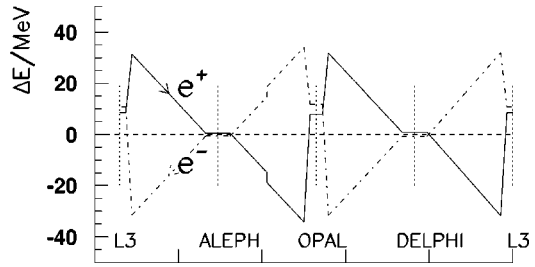

FIG. 10. Deviations from the mean energy in the LEP arcs of electrons and positrons. The step between the ALEPH and OPAL interaction points is due to emittance wigglers, which were in operation at the beginning of fills in order to limit beam-beam effects by increasing the bunch emittance.

maximum of the cross section. In this configuration the errors on M_Z and Γ_Z depend approximately on the errors on the sum and difference of center-of-mass energies at the two off-peak points:

$$\Delta M_Z \approx 0.5\Delta(E_{+2}+E_{-2}), \tag{28}$$

$$\Delta\Gamma_Z \approx \frac{\Gamma_Z}{(E_{+2}-E_{-2})}\Delta(E_{+2}-E_{-2}) = 0.71\Delta(E_{+2}-E_{-2}), \tag{29}$$

where E_{-2} and E_{+2} are the luminosity-weighted center-of-mass energies at the two off-peak points. They have to be known with an error of about 1 MeV in order to match the statistical precision of the measurement of M_Z and Γ_Z.

1. The energy of electrons and positrons in LEP

The energy distribution of the particles in each bunch is almost Gaussian, with a spread (rms) of about 40 MeV at $\sqrt{s}\simeq M_Z$.

The mean energy of the bunch is not constant as it goes around the ring. The acceleration in the radio-frequency (RF) cavities placed symmetrically on either side of the L3 and OPAL interaction points compensates for the energy loss due to synchrotron radiation in the arcs (see Fig. 10). This loss is about 125 MeV per turn at $\sqrt{s}\simeq M_Z$.

The average energies of the electron (positron) bunches going around LEP ($E_{\rm beam}$) is given by

$$E_{\rm beam} = \oint B\, dl, \tag{30}$$

where B is the vertical magnetic field sampled by the electrons on their orbit. Electron and positron average energies are equal, to first approximation. The slight difference of their orbits caused by energy loss in the arcs combined with imperfections of the lattice can induce energy differences of a few tenths of MeV.

The symmetry of LEP and of the RF stations implies that the average energy of the bunches at the interaction points is equal to the beam energy $E_{\rm beam}$. Deviations occur if the accelerating fields seen by the beam at the four RF stations are not equal or if there are errors from misalignment of the RF stations with the interaction points (Arnaudon, 1992). Since the alignment is well measured and the operating status of the RF station is monitored, these corrections are known with a precision of a fraction of a MeV.

The average center-of-mass energy $E_{\rm c.m.}$ is, to first approximation, the sum of the average beam energies at the interaction point. A correlation between the transverse position of the particles in the bunch and their energy (dispersion) may induce a shift in $E_{\rm c.m.}$ (Jowett *et al.*, 1995). This correction is proportional to the offset of the centers of the two bunches at the collision point and to the difference between their dispersions.

2. Energy calibration with resonant depolarization

The average energy of the circulating beam $E_{\rm beam}$ can be measured with a precision of 1 MeV (Arnaudon *et al.*, 1994), using the resonant depolarization method (Arnaudon *et al.*, 1992).

The emission of synchrotron radiation in the vertical bending field polarizes (Sokolov and Ternov, 1964) the LEP beams in the vertical direction. A polarization larger than 10% can be obtained when the beams do not collide after compensation of the magnetic fields of the solenoids and accurate steering of the orbit in the vertical plane. The degree of vertical polarization is measured using a Compton polarimeter (Alexander *et al.*, 1988) with a typical accuracy of 2% absolute.

The spin vector of each electron precesses $a_e\gamma$ times on average during one turn around the ring, where γ is its average Lorentz factor and a_e is the electron magnetic moment anomaly. The *spin tune* is defined as $a_e\gamma$, and the time-averaged spin tune ν_0 of each electron is proportional to the average beam energy, $E_{\rm beam}$:

$$\nu_0 = a_e\gamma = \frac{a_e E}{m_e c^2} = \frac{E_{\rm beam}}{440.6486(1)[\rm MeV]}, \tag{31}$$

where m_e is the mass of the electron and c is the speed of light.

The precession frequency of the polarization vector is precisely measured by inducing a resonant depolarization of the beam with a radial oscillating field from a coil. If the perturbation from the radial field is in phase with the spin precession, then the spin rotations about the radial direction add up coherently from turn to turn and vertical polarization is destroyed. About 10^4 turns ($\approx$1 second) are needed to bring the polarization vector into the radial plane. One resonance condition between the perturbing radial field and the nominal spin precession is $f_{\rm dep}=[\nu]f_{\rm rev}$, where $f_{\rm dep}$ is the frequency of the oscillating field, $f_{\rm rev}$ is the revolution frequency of the particles, which is precisely known, and $[\nu]$ denotes the noninteger part of the spin tune. Its integer part is known accurately enough from the setting of the bending field.

The depolarization occurs slowly compared to the revolution period, and each electron samples the whole energy distribution during the process. For this reason the depolarizing resonance is very narrow (Arnaudon

TABLE III. Size Δ and error σ of the effects changing the LEP center-of-mass energy as a function of time.

Effect	Δ	σ
Temperature variations	$\sim$3 MeV	0.3 MeV
Rise per fill	$\sim$3 MeV	1.0 MeV
Horizontal correctors setting	$\sim$1 MeV	0.4 MeV
Earth Tides (daily)	$\sim$10 MeV	0.1 MeV
Geological shifts (weeks)	$\sim$10 MeV	0.3 MeV
RF corrections	$\sim$10 MeV	0.5 MeV
Vertical collision offsets	$<$1 MeV	0.3 MeV

et al., 1994), about 0.1 MeV, and $E_{\rm beam}$ can be determined with a precision of $\sim$200 KeV. Various spurious effects that can induce systematic errors have been studied theoretically, and experimental bounds on the magnitude of each effect have been established in dedicated experiments (Arnaudon *et al.*, 1994), concluding that the upper bound on the systematic error, on a single measurement of $E_{\rm beam}$, is 1.1 MeV. The largest contribution to this error is due to radial magnetic fields sampled by the beam inside the quadrupoles. Repeated measurements at different machine optimizations will have uncorrelated errors from this source.

3. The time variation of the collision energy

The average beam energy cannot be measured continuously under standard LEP running conditions because the beam-beam interaction prevents the buildup of polarization. A model based on a large set of monitored quantities (currents in the magnets, temperatures, measurement of magnetic fields, status of RF units, etc. . . .) is used to follow the evolution of the energy as a function of time (Assmann *et al.*, 1995). The effects changing $E_{\rm beam}$ and $E_{\rm c.m.}$ are summarized in Table III and can be grouped in three categories: (i) effects changing the dipole field; (ii) effects changing the vertical quadrupole field sampled by the orbit; (iii) effects changing the energy at the interaction point. These effects have been studied with dedicated experiments in order to provide an assessment of the systematic errors.

The magnetic field of a few of the dipoles is monitored with NMR magnetometers. The rise of the dipole magnetic field during a fill has been correlated to vagabond currents that flow along the beam pipe. These current spikes perturb the dipoles and induce a monodirectional walk along their hysteresis curves, resulting in a monotonic increase of the field that saturates on a time scale of several hours. The vagabond currents are mainly due (see Fig. 11) to return currents of electrical trains that do not go back to the power supply along the railtracks.

A variation of 13 μm in the average relative position of the beam with respect to the center of the quadrupole magnets induces a change of $E_{\rm beam}$ of about 1 MeV. The length of the orbit is constrained by the revolution frequency, which is stable to better than one part in 10^{10}, while the radius of the ring is less stable: over a time

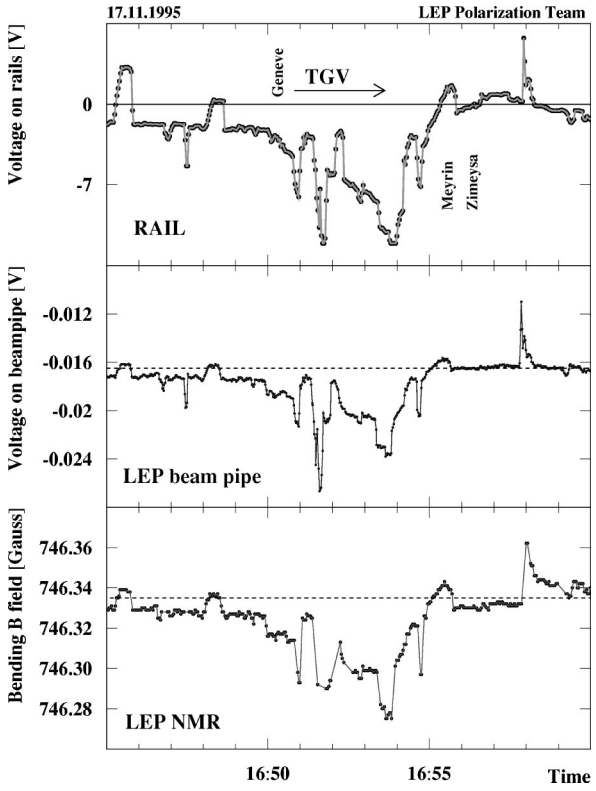

FIG. 11. From top to bottom: railtrack potential, LEP beampipe potential, dipole magnetic field measured with NMR from Assmann *et al.* (1998).

scale of one day it changes by about 100 μm under the influence of earth tides (Arnaudon *et al.*, 1995), and changes of similar magnitude are induced over a longer time scale by other strains in the earth's crust. This effect can be monitored (Wenniger, 1994) by measuring the variation in the position of the beams with respect to the center of the quadrupoles, using the beam position pickups.

The model used to relate the status of the RF cavities to $E_{\rm c.m.}$ also predicts other observables like the synchrotron tune and changes in the longitudinal position of the interaction point. These quantities can be compared to the measured ones (Hildreth *et al.*, 1996), providing strong constraints on the predicted energy variations at the collision points.

The model that describes $E_{\rm beam}$ as a function of time is precisely calibrated using measurements with resonant depolarization. This calibrated model is eventually used to compute the luminosity-weighted energies, with a typical precision of two parts in 10^5 at each collision point. The resulting errors on M_Z and Γ_Z are about 1.5 MeV in both cases (Quast, 1997; Assmann *et al.*, 1998).

D. Results from the *Z* line-hape analysis

The total cross sections to hadrons and leptons measured by each LEP collaboration are fitted to extract the line-shape parameters by applying the formalism outlined in Sec. II.A and using the precise calibration of the

TABLE IV. Average line-shape parameters from the results of the four LEP experiments.

Parameter	Average value
M_Z(GeV)	91.1867±0.0020
Γ_Z(GeV)	2.4948±0.0025
$\sigma^0_{\rm had}$(nb)	41.486±0.053
R_ℓ	20.775±0.027

center-of-mass energy. Assuming lepton universality, the Z line shape is described by four almost uncorrelated parameters: the Z mass and width, the ratio of hadronic to leptonic Z partial widths, and the hadronic peak cross section.

The set of parameters obtained by each collaboration are averaged, taking into account the common sources of errors following the procedure outlined by the LEP Electroweak Group (1997). The average parameters are shown in Table IV. The largest correlation among them is about 15%.

The comparison of the results of the four collaborations and the contributions to the error of each single parameter are discussed in the following sections.

1. The Z mass

The Z mass is the most precise single measurement performed at LEP. The results obtained by the four experiments are shown in Fig. 12.

The measurement is systematically limited and the main error is a common uncertainty of ± 1.5 MeV due to the limited knowledge of the absolute energy scale of the machine (Quast, 1997). This error depends mainly on the uncertainty on the sum of the energies of the two off-peak points, E_+ and E_-, as shown in Eq. (28). The

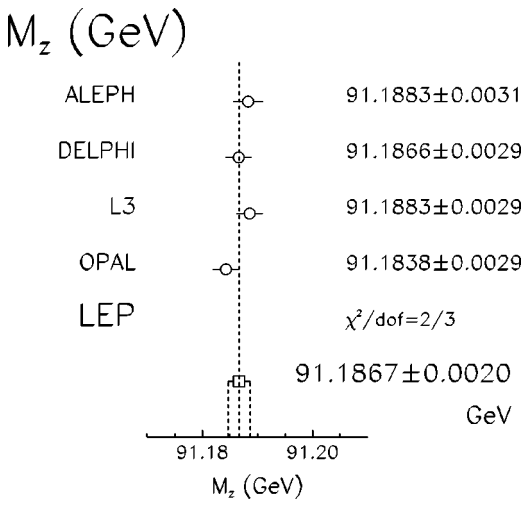

FIG. 12. The Z mass measured by the four experiments, together with the average. The numerical values include the errors common to the four experiments, while the error bars for the four experiments do not, to give a visual impression of the agreement between them, which can also be seen from the value of χ^2 per degree of freedom.

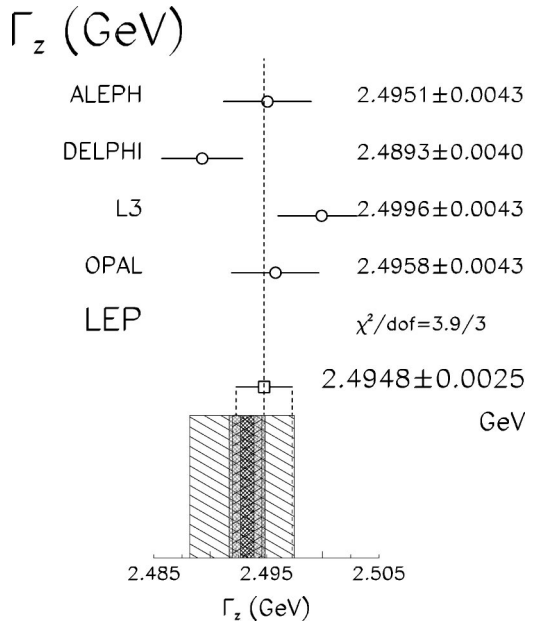

FIG. 13. The Z width measured by the four experiments, together with the average and the minimal-standard-model prediction. The error definitions are those of Fig. 12. The hatching code of the MSM prediction is described in Fig. 3.

error on M_Z is given by the correlated error between E_+ and E_- added in quadrature to their uncorrelated error divided by $\sqrt{2}$.

As discussed in Sec. II.A, the set of parameters used does not describe the Z production and decay completely because it does not include the interference between the Z and the γ exchanges that is fixed to the MSM value in the fit. The interference term can be determined from data with reasonable precision by including in the fit measurements of the cross sections at energies far from the Z peak, such as those collected at Tristan at $\sqrt{s}\sim 60$ GeV and at LEP in the runs above the Z peak. In this fit the total error on the LEP-averaged M_Z increases from 2 MeV to 3.1 MeV (see Sec. II.F).

2. The Z width

The Z width is a very useful observable because of its strong dependence on vacuum polarization corrections. Figure 13 shows the LEP results together with the MSM prediction.

As in the case of the Z mass, the main systematic error comes from the energy calibration: the measurement of the Z width is proportional to the difference between the energies of the two off-peak points, as shown in Eq. (29). Only the uncorrelated errors in E_+ and E_- contribute, giving a systematic error ± 1.5 MeV (Quast, 1997).

The center-of-mass energy spread causes an apparent increase of about 4 MeV in the Z width. This correction is known with good precision and induces a negligible systematic error.

The other important source of uncertainty for the Z width is the background from nonresonating processes

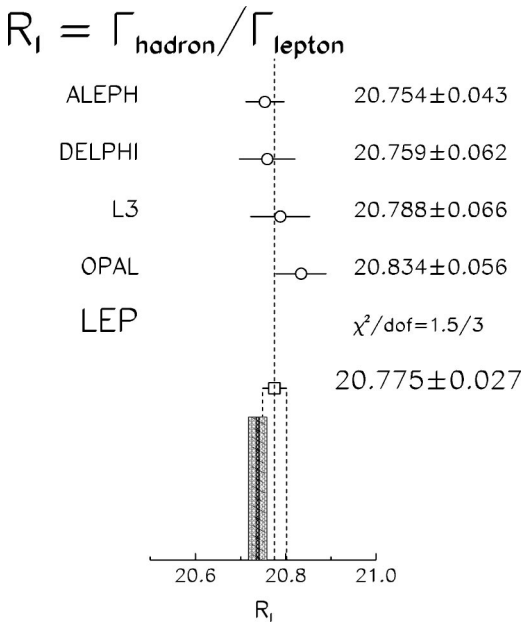

FIG. 14. The ratio of hadronic to leptonic Z partial widths measured by the four experiments, together with the average and the minimal-standard-model prediction. The error definitions are those of Fig. 12. The hatching code of the MSM prediction is described in Fig. 3.

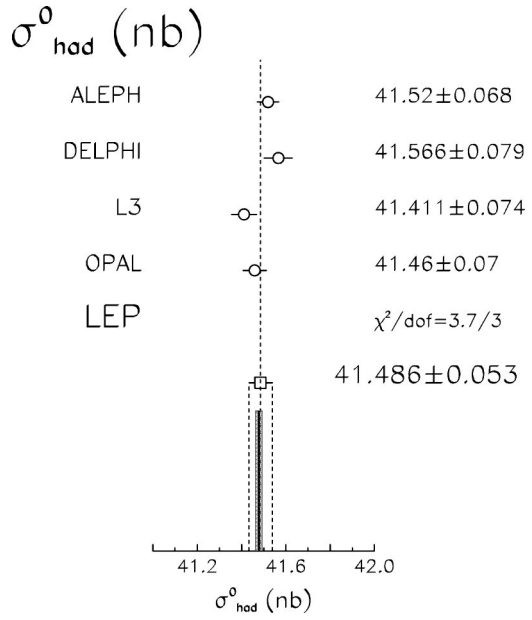

FIG. 15. The hadronic peak cross section measured by the four experiments, together with the average and the minimal-standard-model prediction. The error definitions are those of Fig. 12. The hatching code of the MSM prediction is described in Fig. 3.

like quasireal photon-photon collisions. The current error is slightly above 1 MeV per experiment, but uncorrelated among them. The theoretical error associated with the extraction and interpretation of the width measurement is small, below 1 MeV (Bardin *et al.*, 1995).

3. $R_\ell = \Gamma_h/\Gamma_\ell$

The results of the measurements of R_ℓ, the ratio of the hadronic to the leptonic Z partial widths, are given in Fig. 14. These results are for massless leptons. At the current precision of measurements, only the tau lepton gives rise to a non-negligible mass correction (0.23%).

The experimental systematic error is dominated by the efficiencies and backgrounds of the leptonic selections—about 0.5% per experiment. A common error, from the t-channel correction in the electron channel, contributes 0.1% to the error in R_ℓ. This uncertainty is due to lack of a full $\mathcal{O}(\alpha^2)$ Monte Carlo event generator for Bhabha scattering.

As can be seen from Figs. 4 and 5, R_ℓ does not depend strongly on m_t or on M_H. However, its dependence on the strong-coupling constant makes it an ideal variable for determining $\alpha_s(M_Z^2)$ with minimum theoretical uncertainties. This is done assuming the validity of the MSM to compute the ratio of couplings of quarks and leptons to the Z. Extensions of the MSM which contribute only via Z vacuum polarization do not affect R_ℓ, which is a ratio of partial widths. By contrast, any extension that modifies only the quark couplings has a large influence on R_ℓ.

Using the average value of R_ℓ and the formulas relating R_ℓ to the QCD prediction (Hebbeker *et al.*, 1994), known to $\mathcal{O}(\alpha_s^3)$, one obtains

$$\alpha_s(M_Z^2) = 0.124 \pm 0.004 \pm 0.002_{M_H}, \tag{32}$$

where the second error reflects the uncertainty on the Higgs boson mass. Quark mass terms and the so-called singlet terms are important for this discussion. For a recent review see Chetykin *et al.* (1996).

4. The hadronic peak cross section

The measurements by the four collaborations of the hadronic peak cross section σ_h^0 are shown in Fig. 15.

There are three main contributions to the error: (i) the efficiency and background of the hadron selection contributes about 0.10–0.15% per experiment, uncorrelated; (ii) the experimental uncertainty in the measurement of the absolute luminosity differs depending on the experiment and contributes typically 0.07% and 0.15%; (iii) the theoretical error in the small-angle Bhabha cross section is the largest uncertainty and is common to the four experiments. For this uncertainty the calculation of Jadach and Ward (1996) is used, giving an error of 0.11%. The error induced by limited knowledge of the beam energy spread is negligible.

The MSM prediction is sensitive neither to the top or Higgs masses nor to the strong-coupling constant. Therefore the hadronic peak cross section is an ideal variable for testing possible deviations from the MSM without the uncertainty due to lack of knowledge in some of its parameters. For example, upper limits on the mixing angle between the Z boson and a hypothetical

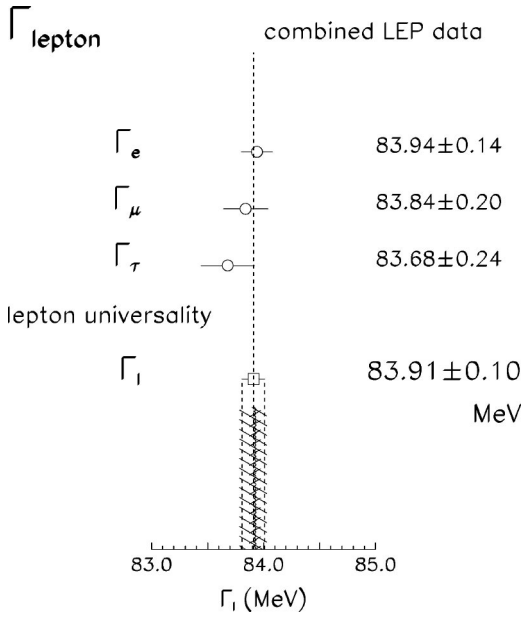

FIG. 16. The partial widths measured at LEP for the three charged leptons, corrected to a massless lepton, are compared to the result of the fit assuming lepton universality and to the prediction of the minimal standard model. The hatching code of the MSM prediction is described in Fig. 3. The error bars show the total error for each quantity.

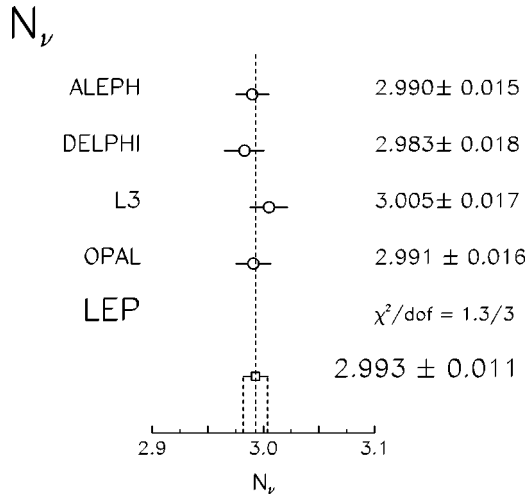

FIG. 17. The number of light-neutrino families measured by the four experiments, together with the average. The error definitions are given in Fig. 12.

extra heavy neutral boson, Z', around 0.003 can be obtained using only σ_h^0, M_Z, and a measurement of α_s from jet studies (see Sec. VI.C).

E. Derived quantities

The four quantities in the previous section describe all line-shape data, assuming lepton universality. The fit can also be performed with six free parameters, deriving the partial decay width into electrons, muons, and tau pairs separately to check lepton universality. They are shown in Fig. 16.

The three results are in agreement, with a $\chi^2/N_{\mathrm{DF}} = 0.3/2$ when common errors are taken into account. The result of the lepton universality fit provides an interesting constraint on vacuum polarization corrections because, in contrast to Γ_Z, it does not depend on α_s.

The invisible width Γ_{inv}, the decay width of the Z to neutrino pairs, is obtained from

$$\Gamma_Z = \Gamma_h + 3\Gamma_\ell + \Gamma_{\mathrm{inv}}.$$

The number of light neutrino families N_ν is obtained from the ratio of the invisible width to the leptonic width. Assuming that the invisible width is only due to neutrino final states, we can write

$$\frac{\Gamma_{\mathrm{inv}}}{\Gamma_\ell} = \frac{\Gamma_Z}{\Gamma_\ell} - R_\ell - 3 = N_\nu \frac{\Gamma_\nu}{\Gamma_\ell}. \tag{33}$$

The ratio Γ_ν over Γ_ℓ is taken from the minimal standard model: $\Gamma_\nu/\Gamma_\ell = 1.991 \pm 0.001$. The small error in the MSM prediction for this ratio results from the large cancellations of the top and Higgs mass dependences. Figure 17 shows the results of the four collaborations, in very good agreement with three families of light neutrinos.

If $N_\nu = 3$ is assumed, the measurement of $\Gamma_{\mathrm{inv}}/\Gamma_\ell$ can be turned into a measurement of Γ_ν/Γ_ℓ:

$$\frac{\Gamma_\nu}{\Gamma_\ell} = 1.9867 \pm 0.0073. \tag{34}$$

This quantity can be used to put limits on the mixing of extra neutral bosons into the Z without assumptions on the strong-coupling constant.

F. *S*-matrix approach

The fitting formula for the Z line-shape fit assumes that the small interference term between the Z- and the photon-exchange amplitudes is sufficiently well described by the MSM (see Sec. II.A). An alternative parametrization of the cross section, the S-matrix ansatz (Borelli *et al.*, 1990; Leike *et al.*, 1991; Stuart, 1991; Riemann, 1992) has been used by the LEP collaborations to put aside this assumption, including in the fit a new parameter which describes this interference.

This parametrization is based on expanding the energy dependence of the cross section around the Z pole. It is suitable for combining cross sections at very different energies, including those measured by Tristan at $\sqrt{s} \sim 60\,\mathrm{GeV}$ and in the high-energy run of LEP above the Z peak.

The reduced cross section $\hat{\sigma}$ of Eq. (24) is replaced by

$$\hat{\sigma}_{ff} = \frac{4}{3}\pi\alpha^2 \left[\frac{g_f^{\mathrm{tot}}}{s} + \frac{s r_f^{\mathrm{tot}} + (s - \bar{M}_Z^2) j_f^{\mathrm{tot}}}{(s - \bar{M}_Z^2)^2 + \bar{M}_Z^2 \bar{\Gamma}_Z^2} \right], \tag{35}$$

where

(i) $\bar{M}_Z$, $\bar{\Gamma}_Z$ are, respectively, the real pole and the width defined by a propagator with denominator $s - \bar{M}_Z^2 + i\bar{M}_Z\bar{\Gamma}_Z$.

(ii) $r_f^{\rm tot}$ is linked to the pole value of the cross section. Due to the different structure of the denominator of the propagator, this pole is not exactly the same pole as in Eq. (24).

(iii) $j_f^{\rm tot}$ is the coefficient of the linear $(s-\overline{M}_Z^2)$ dependence of the total cross sections. It is linked to the contribution of the interference between the Z- and photon-exchange amplitudes.

(iv) $g_f^{\rm tot}$ is the photon-exchange parameter and in the fit is taken from QED.

Four parameters are required in this approach to describe the energy dependence of the $e^+e^-\to f\bar{f}$ for a given flavor, in contrast to the three parameters required in Eq. (24). The new definitions of the Z mass and width are closely connected to the previous ones:

$$\overline{M}_Z = M_Z\sqrt{1+\Gamma_Z^2/M_Z^2},$$

$$\overline{\Gamma}_Z = \Gamma_Z\sqrt{1+\Gamma_Z^2/M_Z^2}.$$

They correspond to a shift in M_Z of 34.0 MeV and in Γ_Z of 0.93 MeV.

The main drawbacks of this parametrization are the large correlations between the fitted values of the parameters and the rather complex interpretation, at the present level of precision, of some of the parameters within the MSM.

This new set of parameters is extracted from the measured cross sections following the formalism described in Sec. II.A and using in Eq. (23) the reduced cross section given in Eq. (35). Since the sensitivity to the interference term is larger at energies far from the Z peak, the total cross sections to hadrons measured above the Z peak by ALEPH (1996c), L3 (1997b), and OPAL (1997e) and below the Z peak by TOPAZ (1995) have been added to the data sample.

Figure 18 shows the correlation between $M_Z=\overline{M}_Z-34\,\text{MeV}$ and $j_{\rm had}^{\rm tot}$. The fitted value of the interference $j_{\rm had}^{\rm tot}=0.14\pm0.12$ is in good agreement with the MSM prediction (0.22). The correlation between $\overline{M}_Z$ and $j_{\rm had}^{\rm tot}$ is -75%.

This parametrization has also been used to fit the energy dependence of the cross section $e^+e^-\to\mu^+\mu^-(n\gamma)$ by reconstructing the effective center-of-mass energy after initial-state radiation (ALEPH, 1997c). The interference term $j_\mu^{\rm tot}=-0.033\pm0.022$ is in good agreement with the MSM prediction (0.004).

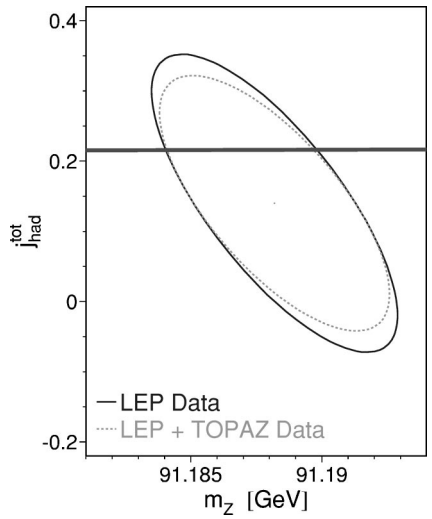

FIG. 18. Contours of 68% confidence level between $(M_Z=\overline{M}_Z-34\,\text{MeV})$ and $j_{\rm had}^{\rm tot}$ for $e^+e^-\to$hadrons (dotted line). The result of the fit using LEP data only (solid line) is also shown. The MSM prediction for $j_{\rm had}^{\rm tot}$ is shown as a horizontal band.

III. *Z* DECAY WIDTHS TO QUARKS

The quark sector is interesting for precision tests of the standard model, as it completes the picture of electroweak interactions and also because electroweak observables involving quarks are potentially very sensitive to standard-model parameters.

Flavor tagging allows precise measurements of the partial widths for the decays $Z\to c\bar{c}$ and $Z\to b\bar{b}$. It is useful to define normalized widths R_c and R_b as partial decay fractions to all hadronic decays

$$R_c\equiv\Gamma_{c\bar{c}}/\Gamma_{\rm had},\quad R_b\equiv\Gamma_{b\bar{b}}/\Gamma_{\rm had}.$$

In this way the effects of α_s [see Eq. (11)] and of the vacuum polarization corrections are canceled.

As already discussed in Sec. I.B, the $Z\to b\bar{b}$ vertex receives sizable corrections from diagrams involving the top quark (see Fig. 2), which are otherwise suppressed. This is the only relevant correction to R_b (Beenakker and Hollik, 1988), and within the MSM R_b is basically dependent on a single parameter, the mass of the top quark.

The partial decay fractions of the Z to other quark flavors, like R_c, are only weakly dependent on m_t; the residual weak dependence is indeed due to the presence of $\Gamma_{b\bar{b}}$ in the denominator. The standard model predicts $\Gamma_{c\bar{c}}/\Gamma_{\rm had}$ to be ≈0.172, valid over a wide range of parameters.

The strong interaction complicates electroweak measurements involving quarks in two ways. First, as quarks cannot be directly observed, electroweak measurements have to be made once the hadronization has taken place. The observables related to the hadrons are modified and often diluted with respect to the original quark-level quantities, limiting the use of a measurement to the cases in which the modification is small and well under control. If the modification is large, the measurement can be turned into a QCD test, assuming that the quark-level process is described by the standard model. The second effect springs from the difficulty of separating different flavors, which all yield high-multiplicity hadronic events, usually made of two or more jets. This problem is partially overcome by LEP and SLC detectors capable of isolating enriched samples of Z hadronic decays to individual flavors. This is particularly true for $Z\to b\bar{b}$ and, to some extent, for $Z\to c\bar{c}$ decays, thanks to the long lifetime and heavy mass of b and c hadrons.

Heavy-flavor tagging is performed by very effective

techniques which allow precision measurements of the ratios R_b and R_c and of the b and c forward-backward asymmetries.

Tagging of lighter quarks is more difficult. Enriched samples of $Z\to s\bar{s}$ decays can be obtained by selecting prompt K^0 and Λ^0, allowing the measurement of the $Z\to s\bar{s}$ asymmetry (DELPHI, 1995d). However, the precision is much lower than in heavier flavors. Detection of prompt photons and of high-momentum stable particles opens up the possibility of separating u-type quarks (u,c) from d-type (d,s,b), and of measuring the partial decay width of the Z to the two types (DELPHI, 1992c; L3, 1993d; Letts and Mattig, 1997; OPAL, 1997f).

Since in $Z\to q\bar{q}$ decays the quark and antiquark are normally boosted in opposite directions, it is useful to divide the event in to two hemispheres and to apply the flavor-tagging techniques described in this section to each hemisphere independently. Correlations among hemispheres, due to momentum conservation or detector effects, are usually small. The event is typically cut into two halves according to a plane orthogonal to the thrust direction defined as the vector $\vec{n}$, which maximizes the quantity

$$T=\frac{\Sigma_i|\vec{p}_i\cdot\vec{n}|}{\Sigma_i|\vec{p}_i|}\ , \tag{36}$$

where $\vec{p}_i$ is the momentum of particle i and the sum runs over all reconstructed particles in the event.

The next section is devoted to a description of heavy-flavor tagging techniques. This provides the necessary background for an understanding of precision measurements of $\Gamma_{b\bar{b}}$ and $\Gamma_{c\bar{c}}$—the subject of the second part of this section—as well as b, c forward-backward asymmetries, described in Sec. IV.

A. Heavy-flavor tagging

The large mass and long lifetime of heavy flavors lend themselves to a number of techniques for effective tagging. These are described in the following sections in order of importance.

1. Lifetime tagging

The most efficient way of selecting b hadrons from Z decays relies on the detection of secondary vertices or on the large impact parameter of the b-hadron decay products. Since the average b lifetime is about $\approx$1.5 ps and b hadrons are produced with a typical energy of 30 GeV at the Z peak, their average path before decaying is about 3 mm. This is an order of magnitude larger than the typical vertexing resolution of present silicon vertex detectors. Alternatively the impact parameter of the b-hadron decay products is about 300 μm, to be compared with an experimental resolution ranging from 20 to 70 μm depending on the momentum of the particle.

The most serious background to lifetime tagging of b hadrons is due to charm. In Table V the lifetimes of b and c hadrons are compared, together with their relative yield at the Z. The charm background can be decreased by exploiting the higher multiplicity of b decays. Indeed the average b-hadron charged-particle yield is about 5 (OPAL, 1994b), to be compared with 2.2 (MARK III, 1991) in the charm case. Another way to reduce charm background is the invariant mass of the b-decay products, which is much larger than in the charm case.

TABLE V. Beauty (Ratoff, 1996; Shepherd-Themistocleous, 1996) and charm (Particle Data Group, 1996) hadron lifetimes. The yield is the rate of b (c) hadron species over the total number of b (c) hadrons in $Z^0\to b\bar{b}$ ($Z^0\to c\bar{c}$) events as given by JETSET 7.3 (Sjostrand and Bengtsson, 1987, 1989; Sjostrand, 1994).

	Lifetime (ps)	Yield per $Z^0\to b$
B^-	1.65±0.04	0.40
B^0	1.55±0.04	0.40
B_s	1.52±0.07	0.12
Λ_b	1.21±0.06	0.08
		Yield per $Z^0\to c$
D^+	1.057±0.015	0.27
D^0	0.415±0.004	0.53
D_s	0.467±0.017	0.12
Λ_c	0.206±0.012	0.08

Lifetime tagging techniques require an accurate measurement of the Z decay point, called the primary vertex. This is usually determined on an event-by-event basis, using the average size and position of the luminous region (beam spot) as a constraint. At LEP the beam spot is flat in the xy plane, having a size of about 5–10 μm in y, 100 μm in x, and about 1 cm in z. The actual size of the beam spot depends on the optics, and its position varies with time. The beam spot position and width are monitored by taking many—typically one hundred—hadronic events and analyzing the impact parameters of particles with respect to a nominal position. The primary vertex of an event is measured by fitting the event's charged-particle tracks to a common vertex, using algorithms as insensitive as possible to decay products of long-lived particles like heavy-flavor hadrons themselves. As an example, the algorithm used by ALEPH (1993a) fitted the primary vertex with the projections of the particles onto the plane perpendicular to the jet they belonged to, so that most of the lifetime bias was removed. In this case the primary vertex was measured with an accuracy of 50 μm in x and 60 μm along the z coordinate. The resolution in y is given by the LEP beam size of 10 μm. At SLC the beam spot is extremely narrow, of the order of a micron in the xy plane. Knowledge of the beam position in the transverse plane is limited by the beam motion, giving a resolution in xy of about 7 μm. Event-by-event reconstruction allows measurement of the z position to within a few tenths of a micron (SLD, 1997f).

Reconstructed charged-particle tracks originating from b-hadron decays show a relatively large minimal approach distance with respect to the primary vertex (i.e., a large impact parameter) and usually cross the b-hadron line of flight *before* the primary vertex itself. This second feature is used to define a sign for the mea-

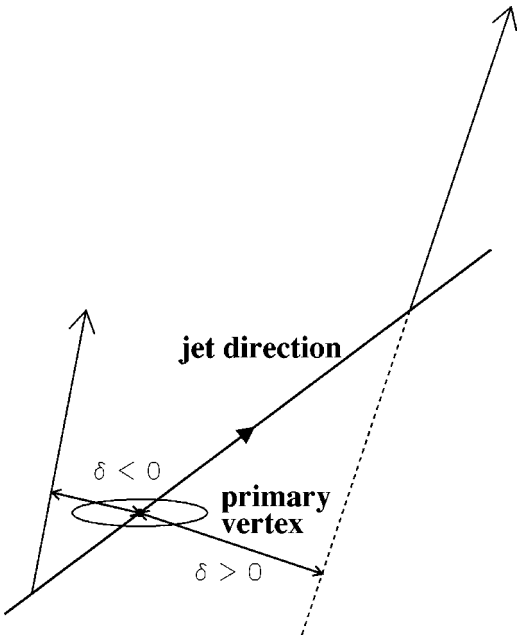

FIG. 19. Definition of impact-parameter sign.

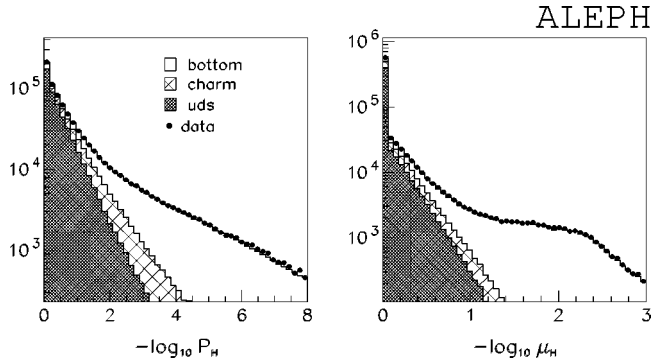

FIG. 20. Lifetime tagging. Negative logarithm of the $\mathcal{P}_H$ tagging variable based on the combination of track impact parameters in a hemisphere. The right plot illustrates the behavior of the invariant-mass related variable (μ_H) described in the text. Both plots are from ALEPH (1997a), dots are data, and histograms are from Monte Carlo simulation.

sured impact parameter. Conventionally the sign is considered as positive when the crossing point is before the primary vertex and negative otherwise (see Fig. 19). The b-hadron direction is usually assumed to be the same as the direction of the jet it belongs to.

The relevant quantity for tagging is the impact-parameter significance $\mathcal{S}$, defined as the signed (positive or negative) impact parameter divided by its estimated measurement error. Tracks from the primary vertex are expected to have $\mathcal{S}$ normally distributed around zero. Tracks with large positive $\mathcal{S}$ come from decays of b hadrons. By counting the number of tracks with $\mathcal{S}$ greater than a certain threshold, one can tag long-lived particles (MARK II, 1991; OPAL, 1993a). The accuracy of impact-parameter tagging can be greatly improved when the negative side of the $\mathcal{S}$ distribution, which is basically free from lifetime information, is used to calibrate the tagging. An effective way to perform this calibration is to fit the negative $\mathcal{S}$ to a functional form and then take the integral of this function as the cumulative probability ($\mathcal{P}_T$) that the track originates from the Z decay point (ALEPH, 1993a). Probabilities from single tracks can be combined to form tagging variables, commonly tracks belonging to the same event hemisphere forming a hemisphere probability ($\mathcal{P}_H$), whereby all tracks in the hemisphere come from the primary vertex. In practice, the performance of this method depends on an effective selection of well reconstructed tracks, with tails as small as possible on the negative side of $\mathcal{S}$. Furthermore it is important that the resolution function (the negative $\mathcal{S}$) be well reproduced by the Monte Carlo simulation used to compute the lighter quark contamination in the b tagged sample. The distribution of the $\mathcal{P}_H$ tagging variable at ALEPH is shown in the left plot of Fig. 20 for data and Monte Carlo simulation of b and lighter quarks. By using this variable ALEPH (1993a) was able to select high-purity b samples (96% pure) while keeping high (26%) b-hadron tagging efficiency.

The information coming from the invariant mass of the b decay products can be naturally incorporated in this technique, for instance by ordering the tracks by $\mathcal{P}_T$ probabilities, then combining them and calculating their invariant mass until they exceed a cut value (typically the charm mass; ALEPH, 1997a, 1997b). For decays of charm hadrons, the first track exceeding the cut is normally coming from the primary vertex and has a high $\mathcal{P}_T$. For decays of b hadrons the probability is typically much lower. This can be seen in the right plot of Fig. 20, where the $\mathcal{P}_T$ of the first track exceeding 1.8 GeV (μ_H) is shown for data and Monte Carlo simulation. By taking advantage of this property, one can decrease the fraction of non-b events in the sample by more than a factor of 2 with no loss of efficiency.

A different approach to lifetime tagging is based on the direct reconstruction of a secondary vertex (OPAL, 1995b). Well reconstructed tracks, belonging to the same jet, are required to be consistent with a common vertex (different from the primary vertex), and specific cuts are applied to reduce contamination from K_s^0 and hyperons. The vertex is used for tagging if a minimum number of tracks [four tracks by OPAL (1995b)] have been successfully fitted to the vertex. As in the impact-parameter case, a decay length significance is defined as the distance from the secondary to the primary vertex, divided by its error. The accuracy of the decay length measurement is improved by constraining the measured decay path to be in the jet direction. Again it is useful to sign the decay length significance, by defining it as positive when the secondary vertex is in front of the primary vertex with respect to the jet direction. The decay length significance for OPAL data and Monte Carlo simulation is shown in Fig. 21.

Backward tags from the negative side of the distribution can be used as a control sample to measure the resolution function directly from the data. In the work of OPAL (1995b) purities similar to the impact parameter case were obtained with a somewhat reduced efficiency (19%). As in the impact-parameter case, the

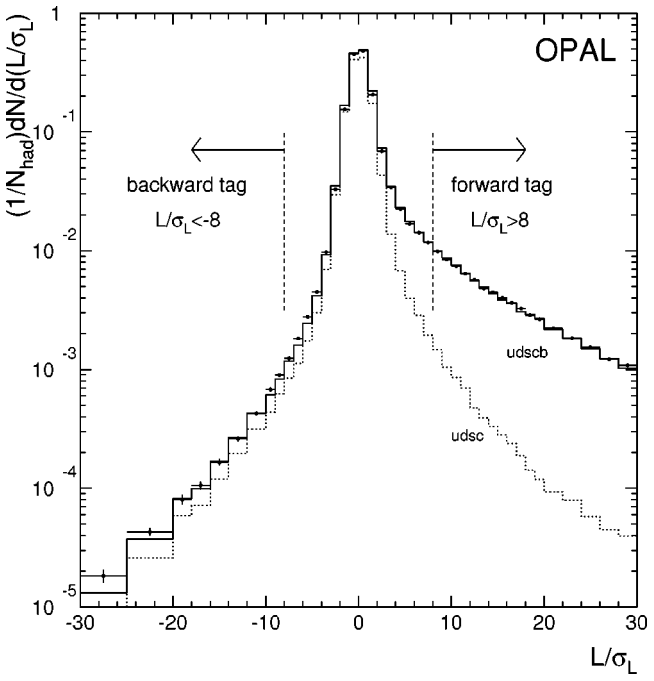

FIG. 21. Lifetime tagging. Distribution of decay length significance for data (points) and Monte Carlo simulation (full histogram) from OPAL (1995b). The dotted histogram shows the contribution from lighter flavors.

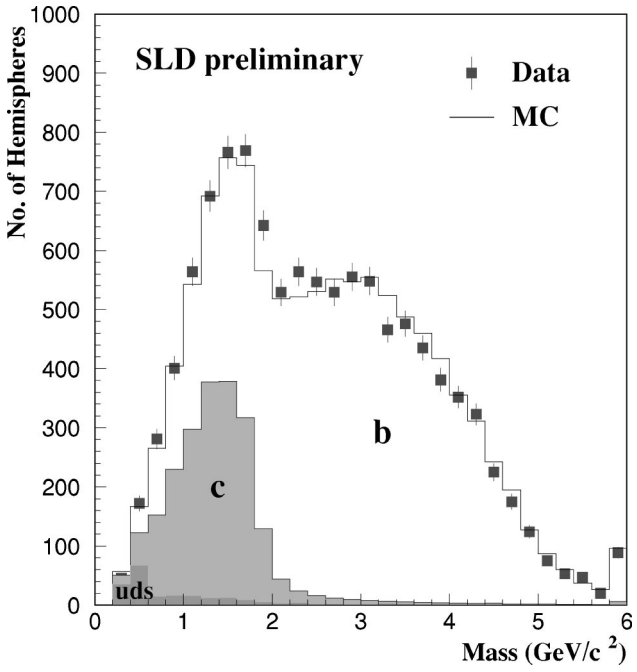

FIG. 22. Lifetime tagging. The invariant mass of charged tracks coming from a secondary vertex, as measured by SLD (1997f). The mass resolution is improved by means of an algorithm which employs the total reconstructed transverse momentum of the charged particles with respect to the hadron direction, to correct for missing neutrals.

invariant-mass information can be incorporated in the vertexing method. This was done by SLD (1997f), who used the invariant mass of tracks originating from a secondary vertex to considerably increase the purity; Fig. 22 shows the discriminating power of their invariant-mass tagging variable.

2. Lepton tagging

Semileptonic decays of heavy quarks provide a distinct signature of $Z\to b\bar{b}$ and $Z\to c\bar{c}$. Electrons and muons in jets are identified with good efficiency by existing LEP and SLC detectors (typically between 60% and 90%), and background contamination is kept under control by the high degree of redundancy offered by these experiments. Jets accompanied by τ leptons are more difficult to identify. Furthermore, the branching ratio of the inclusive semileptonic decay of beauty hadrons to the τ lepton is much lower than that of the two other lepton species (ALEPH, 1995c). In the following, the word *lepton* refers to electrons and muons only. The three main sources of prompt leptons from heavy flavors, each with a branching ratio of about 10% for single lepton species, are

(i) the primary semileptonic b decays, $b\to\ell$;
(ii) the weak decays of b hadrons to c hadrons, with subsequent semileptonic decay of charm, $b\to c\to\ell$;
(iii) the primary semileptonic c decays, $c\to\ell$.

Minor contributions are given by semileptonic decays to τ with subsequent leptonic decay of the τ to electron or muon and by leptonic decays of J/Ψ produced in b decays with a branching ratio of the order of 1% (OPAL, 1991a; ALEPH, 1992a; L3, 1993a; DELPHI, 1994a).

The background from nonprompt leptons is given by the in-flight decays of pions and kaons to muons and e^+e^- pairs from photon conversions in the detector material. Since, in Z decays, hadrons are produced at a rate two orders of magnitude higher than prompt leptons, they can be an important source of background; lepton identification algorithms are tuned to provide good hadron rejection capabilities (of the order of 10^{-3}); (L3, 1992; OPAL, 1993b; ALEPH, 1994e; DELPHI, 1995c).

The large mass of beauty and charm hadrons provides ways to separate the various components of prompt leptons from each other and from background. The radiation of gluons from heavy quarks is suppressed, resulting in a harder momentum spectrum and therefore in high-momentum leptons. Phenomenological models (Peterson *et al.*, 1982) predict that about 70% of the beam energy is carried away by beauty hadrons and 50% by charm hadrons. This has been confirmed by recent measurements of LEP experiments using fully reconstructed events (ALEPH, 1994c, 1995d).

Another feature that is particularly important for semileptonic b decays and a direct consequence of large mass is the high transverse momentum of the lepton with respect to the original b-hadron direction, measured by the axis of the jet associated with the lepton. Jets are reconstructed from charged particles using information from photons detected by the electromagnetic calorimeters and from neutral hadrons detected by had-

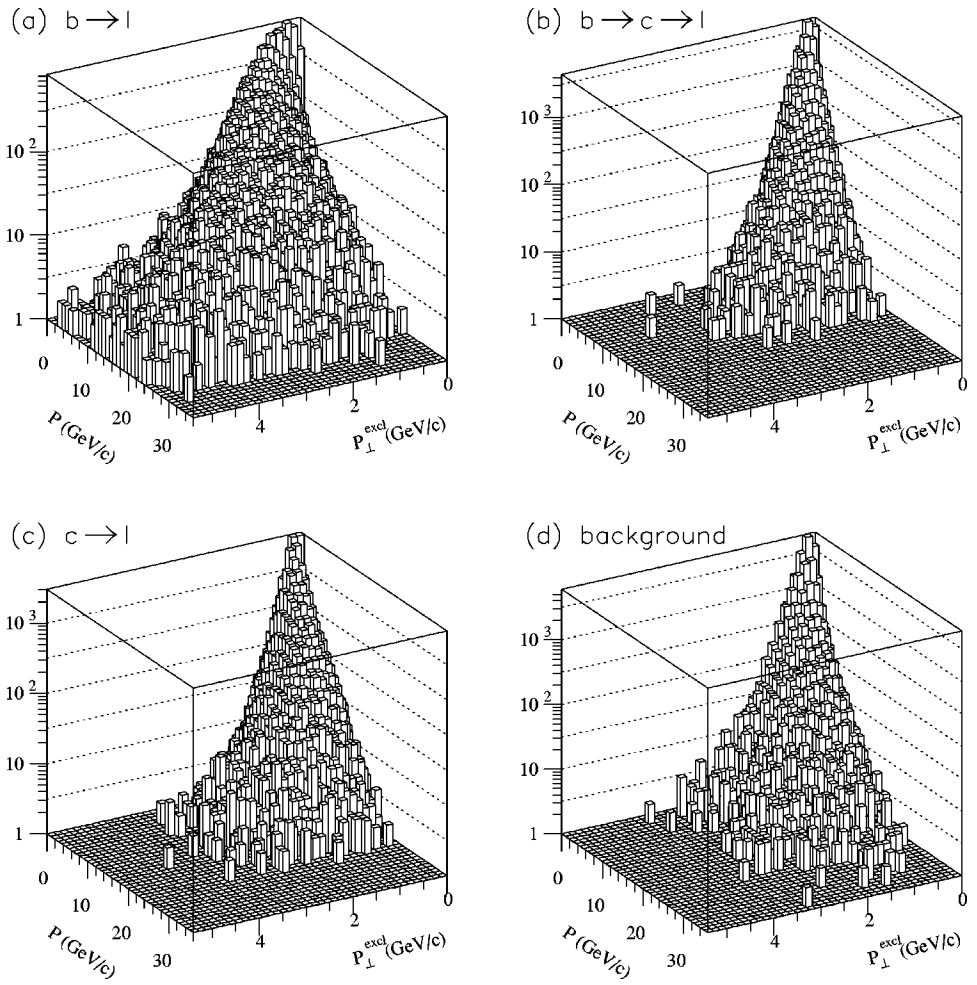

FIG. 23. Lepton tagging. Momentum vs transverse-momentum distributions for leptons from: (a) primary b decays, (b) secondary b decays, (c) primary c decays, (d) lepton fakes.

ronic calorimeters. The most widely used jet clustering algorithm is the Scaled Minimum Invariant Mass by JADE (1988): particles are merged together until they reach a minimum invariant mass that is typically of the order of the b-hadron mass (generally greater to allow for misassociated particles). The typical resolution in the b-hadron direction is about 20 mrad. It has been shown by ALEPH (1994e) that the separation of $b\to\ell$ from the $b\to c\to\ell$ cascade improves if the transverse momentum ($p_\perp$) is measured with respect to the jet reconstructed without the lepton.

Typical distributions of prompt leptons for the three main processes and for background in the $(p,p_\perp)$ plane are shown in Fig. 23.

Primary b decays are characterized by a large average p and $p_\perp$, primary c decays by a smaller $p_\perp$. The $b\to c\to\ell$ cascade is clustered at small p and $p_\perp$. A pure sample of primary b decays can be obtained by selecting leptons at high p and $p_\perp$. A purity of about 80% can be achieved by selecting 25% of the primary semileptonic b decays, thus retaining about 12% of the $Z\to b\bar{b}$ events.

The distribution of the two variables (p and $p_\perp$) for data and the various components of the lepton spectra are shown in Fig. 24 for the L3 experiment.

The shapes of the spectra are taken from lower-energy experiments: $b\to\ell$ and $b\to c\to\ell$ from the fits to ARGUS (1990, 1993) and CLEO (1992, 1993) data and $c\to\ell$ from DELCO (1979) and MARK III (1985). These fits depend on the theoretical model that is assumed for the shape (Altarelli *et al.*, 1982; Grinstein *et al.*, 1986; Isgur *et al.*, 1989; Altarelli and Petrarca, 1991) and this model dependence must be taken into account when lepton tagging is applied to a specific measurement.

High $p_\perp$ leptons provide an important tool for measuring electroweak quantities in the b sector. Electroweak measurements can be extended to the charm sector by fitting the p and $p_\perp$ spectra of the various lepton sources to data (OPAL, 1993d; ALEPH, 1994a; DELPHI, 1995c). The events are first divided into two hemispheres and then classified in terms of the number of tagged leptons in each hemisphere. Multitag events are further decomposed according to the sign of the leptonic charge, to exploit the different correlation to the original quark charge sign which occurs in $b\to\ell$, $b\to c\to\ell$, and $c\to\ell$ decays. The simultaneous fit of the single and dilepton events allows one to determine free parameters such as the partial decay fractions R_b and R_c and

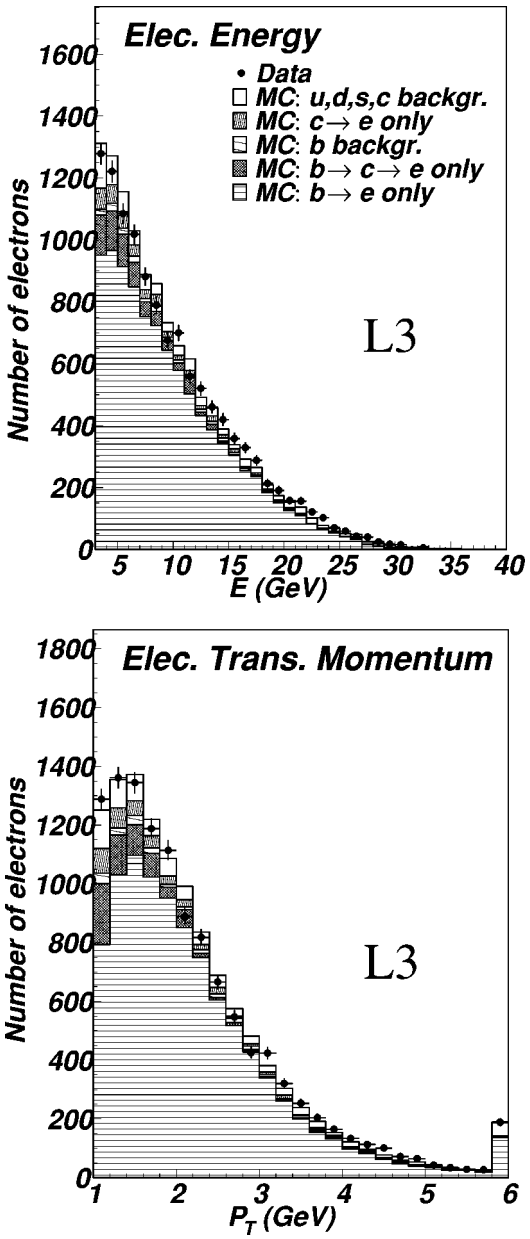

FIG. 24. Inclusive electron spectra as fitted by L3 (1994a), showing data and Monte Carlo simulation with the various components.

the semileptonic branching ratios BR ($b\to\ell$) and BR ($b\to c\to\ell$). Since neutral B mesons can oscillate, the mixing parameter χ is often left free and determined from the fit. Lepton fits in their most elaborated versions are used to determine the b and c forward-backward asymmetries (see Sec. IV.E.1).

3. Event shape tagging

Heavy-quark production affects the global event properties to various degrees. Already, at PETRA center-of-mass energies, event shape variables have been used to obtain enriched samples of b hadrons by the TASSO Collaboration (1984; 1989b). At the Z pole the presence of heavy hadrons, and in particular of b hadrons, characterizes the event in the following way:

(i) The hard fragmentation related to the large mass implies that less energy is carried away by gluon radiation, leaving most of the available energy to heavy-hadron decay products.
(ii) The decay products themselves show a transverse momentum ($p_\perp$) with respect to the associated jet, which is typically larger than the $p_\perp$ of fragmentation particles.
(iii) It is unlikely hat a single detected particle carries away a fraction of the total energy much larger than the other particles of the event. In contrast, this happens in light-quark events where the primary quark hadronizes in a stable particle.

None of these properties can be efficiently described by a single variable; a combination of several variables selected to enhance the above features is used in a multidimensional analysis (DELPHI, 1992b; ALEPH, 1993b, 1994c; L3, 1993b; OPAL, 1995c).

Artificial neural network techniques (Rumelhart *et al.*, 1986; Lonnblad *et al.*, 1991; Bottigli, 1993) have proven very useful for combining several event shape variables with the highest possible selection efficiency by properly treating correlations and making the best use of the available information (Bellantoni *et al.*, 1991, Bortolotto *et al.*, 1991). For this kind of application the response of the neural network is typically a single variable, which disentangles b events from the background. The training of the network is usually performed on Monte Carlo samples. To achieve the best performance it is important that these samples reproduce as closely as possible the features of real data. Moreover, in order to give confidence in the evaluation of the background contamination, the output of the network is controlled on data selected by a different tagging (for instance high $p_\perp$ leptons) to check the Monte Carlo response.

Event shape methods alone are not competitive for tagging $Z\to b\bar{b}$ events. It is hard to obtain purities greater than 70% while keeping a reasonable and well controlled efficiency. However, they have proved to be very useful when combined with other techniques (see Sec. III.B).

4. D^* tagging

The peculiar kinematics of charged D^* decays provide an excellent tool for heavy-flavor tagging at LEP (DELPHI 1990, 1995a; ALEPH, 1991b, 1994c; OPAL, 1995c, 1997d), charm in particular. A D^* can be produced either directly from a primary c quark in $Z\to c\bar{c}$ or as a decay product of a b hadron. Typically the search for D^* is done through the channel $D^{*+}\to D^0\pi^+$ which, being a decay with a q value of only 6 MeV, gives a charged pion of low momentum and small transverse momentum with respect to the D^* line of flight. A very effective tagging can be performed by searching for ex-

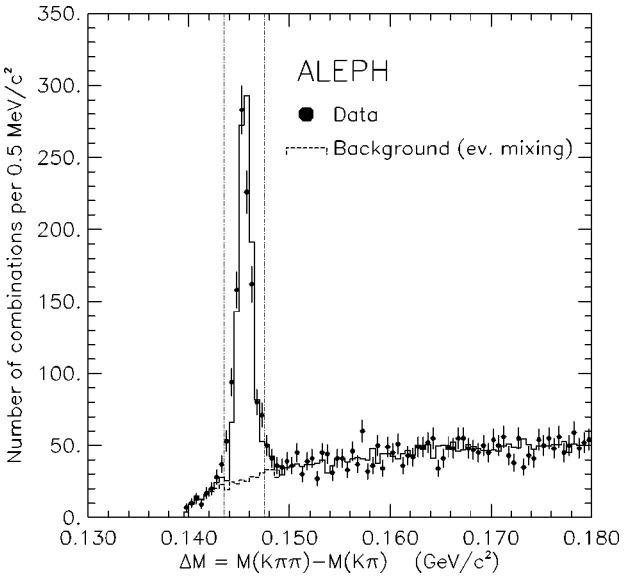

FIG. 25. D^* tagging. The mass difference distribution for $X_E > 0.25$ as seen by ALEPH (1994c) in the channel $D^{*+} \to D^0\pi^+$, $D^0 \to K^-\pi^+$. Data (points) and Monte Carlo results (solid histogram) are shown. The background (dashed histogram) is calculated by an event-mixing technique.

clusive decay chains like[4] $D^{*+} \to D^0\pi^+$ with $D^0 \to K^-\pi^+$, $D^0 \to K^-\pi^+\pi^+\pi^-$, or $D^0 \to K^-\pi^+\pi^0$. Because of the small q value, the distribution of the mass difference $\Delta M = M(K\pi\pi) - M(K\pi)$ yields a sharp peak over a small background, as can be seen in Fig. 25. The remaining two channels, $D^0 \to K^-\pi^+\pi^+\pi^-$ and $D^0 \to K^-\pi^+\pi^0$, are less clean but can still provide a signal-to-background ratio 2:3.

Even if exclusive decays give rather pure samples of D^*, the efficiency is limited by the low branching ratios; for instance the $D^{*+} \to D^0\pi^+$, $D^0 \to K^-\pi^+$ decay chain has a branching ratio of 2.7%, reduced to less than 2% by typical selection cuts. Furthermore D^* produced by $Z \to c\bar{c}$ events have to be disentangled from b-hadron decays. Since primary D^*'s carry away a larger fraction of the original beam energy, a cut on $X_E = E_{D^*}/E_{\text{beam}}$ can be used to select an enriched $Z \to c\bar{c}$ sample (ALEPH, 1994c). The separate contributions of $Z \to c\bar{c}$ and $Z \to b\bar{b}$ events to the X_E distribution are usually measured by means of event shape or lifetime tagging on the hemisphere opposite to the D^* (ALEPH, 1994c; DELPHI, 1995a, OPAL, 1995c). The combined use of X_E and opposite-side tagging improves the separation of $Z \to c\bar{c}$ from $Z \to b\bar{b}$ events tagged through a secondary D^* and allows electroweak measurements to be performed on both the c and the b sectors (DELPHI, 1995a, OPAL, 1995c).

An alternative method of tagging $Z \to c\bar{c}$ events by means of $D^{*+} \to D^0\pi^+$ is based on the inclusive properties of the π^+ which, as was pointed out above, has a very low momentum in the D^{*+} rest frame ($p^* = 40$ MeV); (DELPHI, 1990, ALEPH, 1991b). As a consequence, the pion takes a very low transverse momentum with respect to the original c quark (much lower than the typical 300 MeV of fragmentation tracks) and therefore with respect to the jet axis. The pion longitudinal momentum is bounded by kinematics to be lower than 3 GeV. Therefore the pion is soft and collinear to the jet axis, as is shown in Fig. 26.

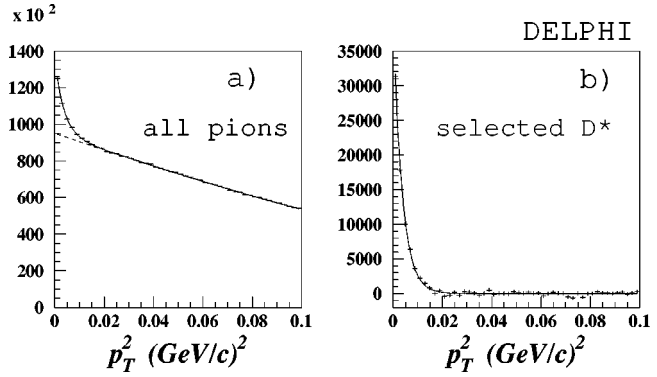

FIG. 26. D^* tagging. Distributions of the squared transverse momentum with respect to the jet axis at DELPHI for (a) inclusive pions, (b) pions from selected D^*.

This method has the advantage of not being restricted to a particular D^0 decay channel. However, the extrapolation of the background below the peak is complicated by the presence of D^* from b hadrons, which produce a broad accumulation in that region.

B. Measurement of R_b from double tagging

The most precise measurements of R_b take advantage of the fact that the b hadrons produced in $Z \to b\bar{b}$ are typically boosted in opposite directions. The two b hadrons are essentially uncorrelated as far as the flavor of their accompanying quarks and their baryonic number are concerned. Therefore it is useful to divide the events into two hemispheres according to the thrust axis and to apply a tag on both sides of the event. This allows one to measure the b tagging efficiency directly on data. If $\mathcal{F}_1$ is the fraction of hemispheres that are tagged and $\mathcal{F}_2$ the fraction of events that are tagged in both hemispheres, one can write

$$\mathcal{F}_1 = R_b \cdot (\epsilon_b - \epsilon_{uds}) + R_c \cdot (\epsilon_c - \epsilon_{uds}) + \epsilon_{uds},$$

$$\mathcal{F}_2 = R_b \cdot (C_b \cdot \epsilon_b^2 - \epsilon_{uds}^2) + R_c \cdot (\epsilon_c^2 - \epsilon_{uds}^2) + \epsilon_{uds}^2,$$

where $\epsilon_b, \epsilon_c, \epsilon_{uds}$ are the efficiency of the tags on b, c, and uds events, respectively, and C_b is a coefficient that takes into account possible correlations between the efficiencies in the two hemispheres for b events. These relations are based on the very similar efficiencies of the tagging methods for $Z \to u\bar{u}$, $Z \to d\bar{d}$, and $Z \to s\bar{s}$ decays and on the fact that the sum of partial decay fractions of the Z to the five quark species is one. Efficiency correlation coefficients for lighter quarks can be neglected, since the tags are designed to have low efficiency for

[4] In this section charge-conjugate modes are implied.

$udsc$ events; therefore the effect of these correlations on the measurement is negligible.

The main advantage of the double tagging method is that the two equations can be solved simultaneously for R_b and ϵ_b, so that the b tagging efficiency is measured on data and is not a source of systematic error. It is instructive to solve the two equations by neglecting ϵ_c and ϵ_{uds}:

$$R_b \approx \frac{C_b \cdot \mathcal{F}_1^2}{\mathcal{F}_2}$$

$$\epsilon_b \approx \frac{\mathcal{F}_2}{C_b \cdot \mathcal{F}_1}.$$

These equations show that the statistical error on R_b is dominated by the double tagging fraction, which has by far the largest statistical uncertainty. With the statistics so far accumulated by LEP experiments, and using high-efficiency tagging methods such as lifetime or event shape tagging, rather low statistical errors are obtained. More important for precision measurements is the fact that the measurement of R_b is directly affected by the knowledge of C_b, i.e., by the uncertainty on the correlation coefficient. Efficiency correlations originate from detector effects, from the physics, or from the algorithm itself. Typical examples of the first two cases are the correlated loss in acceptance due to the beam hole and hard gluon radiation, which sometimes pushes both b hadrons into the same hemisphere. An example of an algorithm-related correlation is the possible bias in the primary vertex position due to inclusion of a displaced track produced in a b-hadron decay. The primary vertex is pulled by the b hadron, causing bias, and is pushed away from the opposite $\bar{b}$, yielding a negative correlation. Great care is taken in the most precise measurements (DELPHI, 1996a; ALEPH 1997a, 1997b; OPAL, 1997a) to identify the cause of the correlations and make sure that the Monte Carlo simulation is reliable in predicting the magnitude of the effect. In these measurements the value of the coefficient C_b is very close to 1.0, and any deviation due to individual components is of the order of a percent or less.

The presence of lighter quarks, in particular of charm particles, is another source of systematic error. The uncertainty on ϵ_c is evaluated with the help of Monte Carlo simulations tuned to reproduce charm hadron properties (lifetimes, decay multiplicities) measured at lower-energy experiments. A major uncertainty for the efficiencies of light quarks is the yield of hard gluons splitting to a $b\bar{b}$ pair. Theoretical arguments (Seymour, 1995) as well as the directly measured $g \to c\bar{c}$ (OPAL, 1995a) are used to constrain this process.

Another source affecting the size of the estimated charm background is the value of R_c. Since this is predicted quite precisely by the standard model, results are usually given assuming $R_c = 0.172$; nevertheless the dependence of the result on R_c is given by all papers and is used to perform the combined R_b, R_c averages described later on.

Double tagging provides the most accurate measurements to date. Event shape tagging methods (ALEPH, 1993b) and, even better, lifetime tagging methods (ALEPH, 1993a, DELPHI 1995b, OPAL, 1995b) are best suited for the high efficiency needed. Results using lepton tagging alone suffer from statistical errors (ALEPH, 1994a), but can be extended to simultaneous measurement of R_b and R_c. In the most recent measurements (ALEPH, 1997b; DELPHI, 1997a; L3, 1997a, OPAL, 1997a; SLD, 1997f) several tagging methods are used to increase efficiency. Multitag methods also have the advantage of permitting, at least for some of the tagging variables, the determination of charm and lighter-quark efficiencies from data, reducing the dependence on Monte Carlo simulation and external measurements.

C. R_c from the D^* and D mesons

High-energy D^* mesons are a signature of $Z \to c\bar{c}$ events and can be used to measure R_c. The techniques used to detect prompt D^* mesons and to disentangle them from b-hadron decay products have been described in Sec. III.A.4. The production rate in the low-background channel $D^0 \to K^- \pi^+$, which is most often used, can be written as the product of the following quantities:

$$R_c \cdot P(c \to D^{*\pm}) \cdot B(D^{*+} \to D^0 \pi^+) \cdot B(D^0 \to K^- \pi^+),$$

where $P(c \to D^{*\pm})$ is the probability that a c quark hadronizes in a D^*. The first published measurements at LEP assumed that the hadronization of a c quark yields the same fraction of D^* mesons as in lower-energy measurements (CLEO, 1988; HRS, 1988; TASSO, 1989a) and R_c was measured with this hypothesis (DELPHI, 1993, OPAL, 1995c). This assumption relies on the expectation that no significant differences exist in c-quark hadronization to excited D states over a wide range of energies far from the charm threshold.

With the full statistics collected at the Z by LEP experiments, it is possible to perform measurements free from this assumption by using double-tagging techniques (ALEPH, 1996e; DELPHI, 1996b; OPAL, 1997d). As the double-tagging sample suffers from low statistics, one of the two D^* is taken from the inclusive D^* sample by tagging the soft pion (see Sec. III.A.4). This method was originally employed to perform a single-tag R_c measurement (DELPHI, 1990). This requires a careful assessment of the background below the prompt D^* peak due to secondary $B \to D^*$ decays and resonances yielding pions at low transverse momentum. Since all excited D states should eventually decay to D^0 or D^+ mesons, the $D^0 + D^+$ yield can be used to perform an R_c measurement. This technique was pioneered by DELPHI (1993) and recently extended to double tagging by ALEPH (1996e). One method that is relatively free from assumptions is the charm counting method. The sum of the yield of high-energy D^0, D^+, D_s, and Λ_c is directly proportional to R_c, as essentially all charm hadrons are decaying to one of these weakly decaying

states. Measurements of R_c using this method have recently been presented by DELPHI (1996b), OPAL (1996b), and ALEPH (1997d). Precise measurements of R_c are also obtained using lepton fits.

D. Average of R_b and R_c

In most R_b and R_c measurements the systematic error is the dominant component of the total error. This means that averaging the measurements requires a careful assessment of the common systematics. A robust procedure for averaging heavy-flavor electroweak measurements was worked out by the four LEP Collaborations within the LEP Electroweak Working Group (1996). This procedure also takes care of the correlations between different electroweak quantities such as R_b versus R_c. The average of the most recent R_b and R_c measurements, which includes new preliminary measurements presented at the Jerusalem conference (LEP Eectroweak Group, 1997), is

$$R_b = 0.2170 \pm 0.0009,$$

$$R_c = 0.1734 \pm 0.0048.$$

The average is compared to the most precise results and to the standard-model expectation in Fig. 27. The R_b and R_c averages are negatively correlated, and the correlation coefficient is -0.20. This result is shown in Fig. 28 together with the standard-model expectation versus the top mass. The agreement with the standard model for R_c is very good, while for R_b it is slightly worse than one standard deviation. It has to be said that the latest R_b measurements are showing a very good agreement with the standard model (Steinberger, 1997). In the past (Olshevski, 1995) both R_c and R_b were off with respect to the expectations. Since then a considerable effort has been made to improve our understanding of the systematics and, in particular for R_b, this has led to a reduction of the charm background and to the development of analyses as independent as possible from the hemisphere correlations (see Sec. III.B).

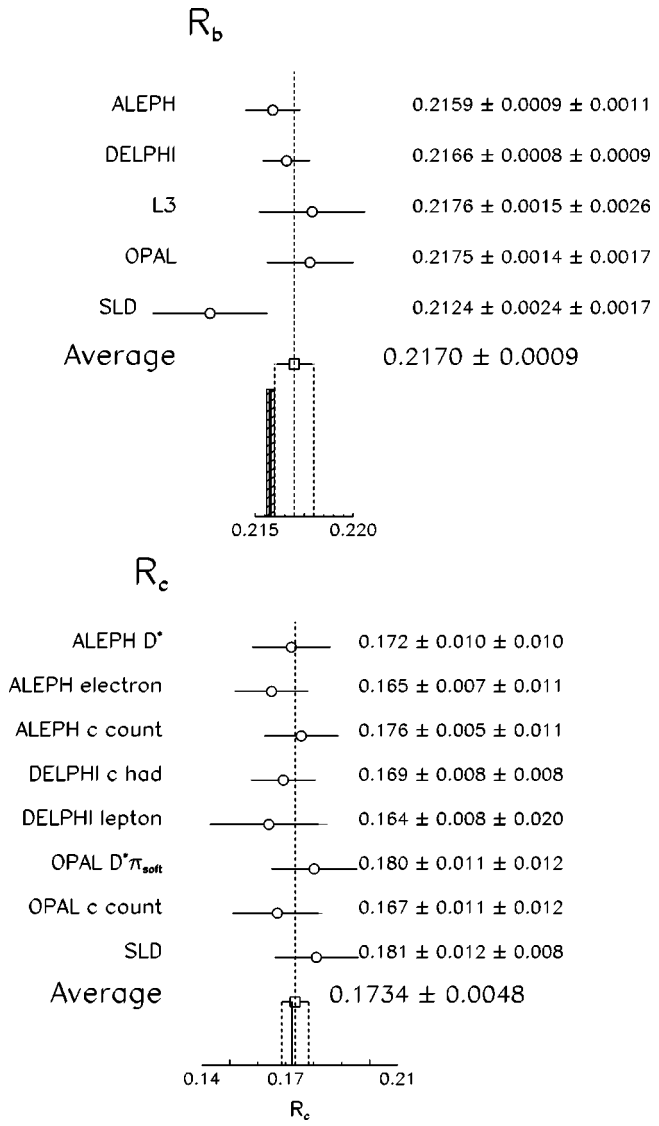

FIG. 27. The most recent R_b, R_c measurements and the resulting LEP/SLD average are compared with the prediction of the minimal standard model. The hatching code of the MSM prediction is described in Fig. 3. The MSM prediction for R_c is a very thin line almost coincident with the average of the measurements.

IV. ASYMMETRIES AT THE *Z* POLE

Parity violation in the weak neutral current is caused by the difference between couplings of the Z to right-handed and left-handed fermions. In the reaction $e^+e^- \to Z \to f\bar{f}$ with unpolarized beams, parity violation in the production causes the Z to be polarized along the direction of the beams. The amount of polarization ($\mathcal{A}_e$) depends on the ratio between the vector (g_{Ve}) and axial-vector (g_{Ae}) coupling constants of the electron:

$$\mathcal{A}_f = \frac{2 g_{Vf} g_{Af}}{(g_{Vf})^2 + (g_{Af})^2} = \frac{2 g_{Vf}/g_{Af}}{1 + (g_{Vf}/g_{Af})^2}. \tag{37}$$

In the parity-violating decay of the $Z \to f\bar{f}$, the fermion is emitted in a preferential direction with respect to the direction of the spin of the Z. The asymmetry for *fully* polarized Z is $\frac{3}{4}\mathcal{A}_f$ where the factor $\frac{3}{4}$ comes from integration over the polar angle. Due to angular momentum conservation, the helicity of the fermion is correlated to the direction of the spin of the Z.

Each Z decay into an $f\bar{f}$ pair can be characterized by the direction and the helicity of the emitted fermion f. Referring to the hemisphere where the electron beam is pointing as "forward," we can subdivide the events into four categories: FR, BR, FL, and BL, corresponding to right-handed (R) or left-handed (L) fermions emitted in the forward (F) or backward (B) direction. The total cross section $\sigma_{\rm tot}$ is measured by adding up the four categories. Three asymmetries can be defined:

$$A_{\rm pol} = \frac{\sigma_{F,R} + \sigma_{B,R} - \sigma_{F,L} - \sigma_{B,L}}{\sigma_{\rm tot}} = \frac{\sigma_R - \sigma_L}{\sigma_{\rm tot}}, \tag{38}$$

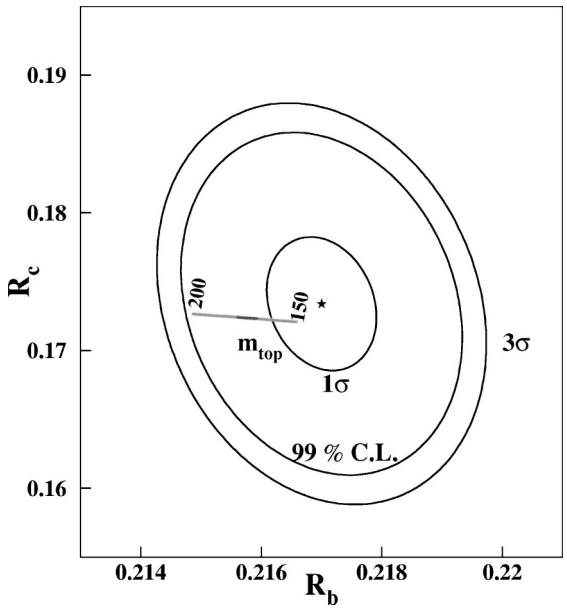

FIG. 28. The LEP and SLD average of R_c vs R_b showing the 1σ, 99% C.L. and 3σ contours. The standard-model expectation as a function of the top mass is indicated.

$$A_{\rm pol}^{\rm FB}=\frac{\sigma_{F,R}+\sigma_{B,L}-\sigma_{B,R}-\sigma_{F,L}}{\sigma_{\rm tot}}, \tag{39}$$

$$A_{\rm FB}=\frac{\sigma_{F,R}+\sigma_{F,L}-\sigma_{B,R}-\sigma_{B,L}}{\sigma_{\rm tot}}=\frac{\sigma_F-\sigma_B}{\sigma_{\rm tot}}. \tag{40}$$

The polarization asymmetry $A_{\rm pol}$ depends only on the helicity of the fermions emitted in the decay of the Z and is not sensitive to parity violation in the production. The forward-backward polarization asymmetry $A_{\rm pol}^{\rm FB}$ measures the polarization of the Z produced in the e^+e^- collision and does not depend on the flavor of the fermion emitted in the Z decay. The forward-backward asymmetry $A_{\rm FB}$ is proportional to the product of the two effects and can be measured without analyzing the polarization of the final state. The first two asymmetries require the measurement of the helicity of the fermion. In practice it can be statistically measured only for the channel $Z\to\tau^+\tau^-$. The forward-backward asymmetry $A_{\rm FB}$ is easier to measure because only the identification of the charge of the fermion and the measurement of its direction are needed. It can be measured for all tagged flavors (e, μ, τ, s, c, and b) and inclusively for hadrons (jet charge asymmetry).

Beam polarization provides the most natural way to separate initial from final-state couplings. The simplest way to access initial-state couplings with polarized beams is the measurement of the left-right asymmetry $A_{\rm LR}$. The cross sections for Z production σ_l and σ_r are measured at SLD with the electron beam having left-handed (l) or right-handed (r) polarization, while the positron beam is unpolarized (lower-case indices are used to distinguish initial-state helicity from final-state helicity). The left-right asymmetry is defined as

$$A_{\rm LR}=\frac{1}{\mathcal{P}}\frac{\sigma_l-\sigma_r}{\sigma_l+\sigma_r}, \tag{41}$$

TABLE VI. Magnitude of the forward-backward asymmetry and its sensitivity to $\sin^2\theta_{\rm eff}^{\ell}$ for various fermion species at the pole of the Z. The numerical values of the couplings given in the Appendix are used.

	$A_{\rm FB}$	$\partial A_{\rm FP}/\partial\sin^2\theta_{\rm eff}^{\ell}$
Leptons	0.02	−1.7
u and c quarks	0.07	−4.0
d, s, and b quarks	0.10	−5.6

where $\mathcal{P}$ is the average beam polarization.

Beam polarization is also useful for the measurement of the final-state couplings where one can take advantage of the difference—which is sizable, especially for quark production—in the forward-backward asymmetry when the polarization of one of the beams is switched from left-handed to right-handed. It is convenient to define the forward-backward polarized asymmetry for the production of a fermion f as

$$A_{\rm FB}^{\rm pol}=\frac{1}{\mathcal{P}}\frac{(\sigma_{F,l}-\sigma_{F,r})-(\sigma_{B,l}-\sigma_{B,r})}{(\sigma_l+\sigma_r)}, \tag{42}$$

where $\sigma_{F,l}$ is the forward cross section for the left-handed beam and the other terms are defined using the same convention.

These asymmetries have been measured at LEP and SLC and have been interpreted as measurements of the ratios of the fermion coupling constants to the neutral current. To match the experimental precision, the measured asymmetries have been corrected for the effects of initial and final-state radiation, for the photon exchange, and for $Z-\gamma$ interference using the standard-model prediction. Moreover, their predicted energy dependence is used to extrapolate the measurement to $\sqrt{s}=M_Z$. In this report the superscript "0" indicates that the measured asymmetry has been corrected for the above-mentioned effects. In the Appendix it is shown that at $\sqrt{s}=M_Z$ the corrected asymmetries can be expressed in terms of the ratio of the effective fermion couplings to the neutral current:

$$A_{\rm pol}=-\mathcal{A}_f, \tag{43}$$

$$A_{\rm pol}^{\rm FB}=-\tfrac{3}{4}\mathcal{A}_e, \tag{44}$$

$$A_{\rm FB}=\tfrac{3}{4}\mathcal{A}_e\mathcal{A}_f, \tag{45}$$

$$A_{\rm LR}=\mathcal{A}_e, \tag{46}$$

$$A_{\rm FB}^{\rm pol}=\tfrac{3}{4}\mathcal{A}_f. \tag{47}$$

The vector coupling of charged leptons (ℓ) to the neutral current is small compared to the axial-vector coupling, and the expected value of $\mathcal{A}_\ell$ is about 15%. The expected forward-backward asymmetry of leptons at the Z pole is very small ($\sim$1.5%), whereas it changes very rapidly with energy. Therefore the precise determination of this asymmetry requires a careful handling of the energy dependence. The other asymmetries are larger (see Table VI for the forward-backward asymme-

tries) and their energy dependence is less important and can be handled by applying a simple correction to the measured value.

Assuming lepton universality, the ratios of the couplings of the Z to the charged leptons are equal. This ratio is used to define the effective mixing angle $\sin^2\theta^{\ell}_{\rm eff}$ [see Eq. (10)]:

$$\sin^2\theta^{\ell}_{\rm eff}=\frac{1}{4}\left(1-\frac{g_{V\ell}}{g_{A\ell}}\right). \tag{48}$$

The asymmetries involving leptons provide a direct determination of the effective mixing angle. As is shown in Sec. IV.E, the forward-backward asymmetries measured from quark final states also provide a measurement of $\sin^2\theta^{\ell}_{\rm eff}$ up to a very small correction.

At the Z pole the forward-backward asymmetry is proportional to $\mathcal{A}_e\mathcal{A}_f$ [see Eq. (45)]. In the case of quarks the second term $\mathcal{A}_f$ is large and weakly dependent on $\sin^2\theta^{\ell}_{\rm eff}$, leaving most of the dependence on the weak mixing angle to $\mathcal{A}_e$. Therefore, at the Z, the forward-backward asymmetry for quarks is essentially linearly dependent on $\sin^2\theta^{\ell}_{\rm eff}$, while for leptons it shows a quadratic dependence. The effect of this behavior is shown in Table VI, where the sensitivity of the forward-backward asymmetry to $\sin^2\theta^{\ell}_{\rm eff}$ is given for leptons and for u-type and d-type quarks. The sensitivity to $\sin^2\theta^{\ell}_{\rm eff}$ is maximal for the A_{LR} asymmetry and for other asymmetries that measure $\mathcal{A}_\ell$ directly ($\partial A_{\rm FB}/\partial\sin^2\theta^{\ell}_{\rm eff}\simeq -7.8$).

A. Lepton forward-backward asymmetries

The lepton forward-backward asymmetry is measured from the angular distribution of the final-state fermion in the process $e^+e^-\to\ell^+\ell^-(\gamma)$ after these events are selected with procedures similar to those used for the measurement of the total cross section (see Sec. II.B.3).

In the case of the e^+e^- final state, the t-channel photon exchange is taken into account by subtracting the MSM expectation for the angular distribution of all t-channel contributions from the measured angular distribution. This expectation is defined as the complete expectation for the e^+e^- final state, as computed by Beenakeer *et al.* (1991a, 1991b) minus the expectation for the $\mu^+\mu^-$ final state.

The information contained in the angular distribution is extracted from the data either by counting the events with the negative lepton in the forward or backward hemisphere and applying Eq. (40) or by fitting the odd term $A_{\rm FB}$ of the angular distribution of the negative lepton:

$$\frac{d\sigma}{d\cos\theta}=\frac{3}{8}\sigma^{\ell}C(\cos\theta)\left(1+\cos^2\theta+\frac{8}{3}A_{\rm FB}\cos\theta\right), \tag{49}$$

where θ is the angle of the negative lepton and $C(\cos\theta)$ is an acceptance function which is symmetric, provided the selection efficiency is charge symmetric or forward-backward symmetric. This method assumes a given behavior of the angular distribution and, under this assumption, allows a more accurate determination of $A_{\rm FB}$, since the whole angular distribution is used.

The corrected asymmetries $A^0_{\rm FB}(\ell)$ ($\ell=e$, μ, and τ) are extracted by fitting the measured $A_{\rm FB}(s)$ to a model-independent formula that explicitly incorporates the photonic corrections as well as those due to boxes and to imaginary parts, notably the imaginary part of the photon vacuum polarization $\Delta\alpha$ (see Sec. I.B). The fitting formula takes into account the energy dependence of the asymmetry, and the fit is done simultaneously with the line-shape data to account for the effect of the energy uncertainty, which enters in the form $(s-M_Z^2)$.

The energy dependence near the Z peak (given in the Appendix) is caused by interference between the photon and the Z exchange and corresponds to a change of

$$\Delta A^{\ell}_{\rm FB}/\Delta E_{\rm c.m.}\simeq 0.00009/{\rm MeV}.$$

Since the vector couplings of the leptons are small, the slope of $A^{\ell}_{\rm FB}(s)$ as a function of the energy is mainly sensitive to the axial couplings. In the simultaneous fit of the line-shape data and $A^{\ell}_{\rm FB}(s)$ the axial couplings are mainly determined by the line-shape and they are used to transport the off-peak measurements of $A^{\ell}_{\rm FB}(s)$ to $\sqrt{s}=M_Z$. In a different approach (Leike *et al.*, 1991; Stuart, 1991; Riemann, 1992), the slope of the asymmetry is described by a free parameter and the consistency in the determination of axial couplings between the line-shape and the forward-backward asymmetries is checked.

The measurement of $A^0_{\rm FB}(\ell)$ is quite simple and robust, and its accuracy is limited by the statistical error. When a log-likelihood method is applied to fit the data using Eq. (49), the result is independent of the detection efficiency of the apparatus as a function of the polar angle, provided it is charge-symmetric or forward-backward symmetric. Typical systematic errors quoted by the LEP experiments are of the order of $\Delta A^0_{\rm FB}(\ell)=0.001$ for $\ell=\mu,\tau$. For $\ell=e$, the theoretical uncertainty introduced in the treatment of the t-channel terms increases this error to $\Delta A^0_{\rm FB}(\ell)=0.002$. The error on the center-of-mass energies gives a contribution of $\Delta A^0_{\rm FB}(\ell)=0.0008$, comparable to the experimental systematics. Some of these errors are common to the four experiments and are treated in a correlated way when averaging the measurements.

Assuming lepton universality, the three measurements of $A^0_{\rm FB}(\ell)$ for $\ell=e$, μ, and τ can be averaged. The results of these averages of the four LEP experiments and the global LEP average are shown in Fig. 29. The LEP average, including preliminary results presented at the Jerusalem Conference (LEP Electroweak Group, 1997), is $A^0_{\rm FB}(\ell)=0.0171\pm 0.0010$.

This result can be converted into a precise measurement of $\sin^2\theta^{\ell}_{\rm eff}$ using Eqs. (45), (37), and (48). Alternatively, using Eqs. (45) and (37), one can interpret the measurements of $A^0_{\rm FB}(\ell)$ for $\ell=e$, μ, and τ as measurements of the products A_eA_ℓ and can use them to determine the ratios $g_{V\ell}/g_{A\ell}$ for the three charged leptons up to a common sign.

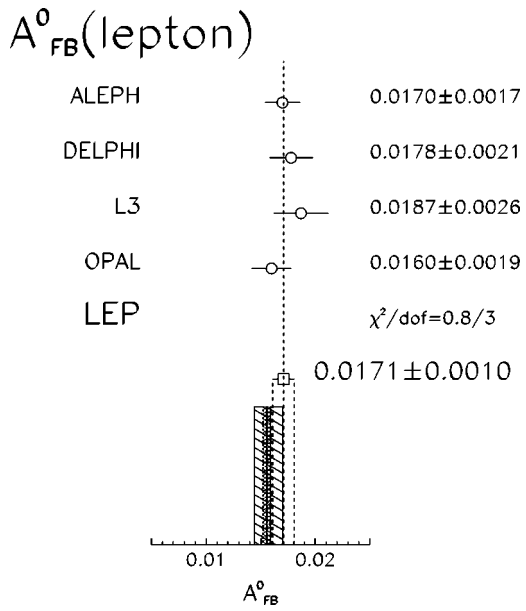

FIG. 29. The most recent measurements of $A_{\rm FB}^0(\ell)$ and the resulting LEP average compared with the expectation of the standard model. The hatching code of the MSM prediction is described in Fig. 3.

B. Tau polarization asymmetries

The τ polarization as a function of the polar angle is used to measure the two asymmetries defined by Eqs. (38) and (39).

The helicity of the two taus from Z decay are nearly 100% anticorrelated and the tau polarization for any $\cos\theta$ bin is defined by

$$P_\tau=\frac{\sigma_R-\sigma_L}{\sigma_R+\sigma_L}, \tag{50}$$

where σ_R is the cross section to produce a right-handed τ^- and σ_L is the cross section to produce a left-handed τ^-. Comparing this definition with Eq. (38), we see that the polarization asymmetry $A_{\rm pol}$ is equal to the tau polarization measured over the entire $\cos\theta$ range. The forward-backward polarization asymmetry $A_{pol}^{\rm FB}$ can be measured by comparing the polarization measured in the forward and in the backward directions.

A more sensitive method is to fit the measured dependence of the polarization as a function of the polar angle θ to its prediction to lowest order:

$$P_\tau(\cos\theta)=\frac{A_{\rm pol}(1+\cos^2\theta)+\frac{8}{3}A_{\rm pol}^{\rm FB}\cos\theta}{(1+\cos^2\theta)+\frac{8}{3}A_{\rm FB}\cos\theta} \tag{51}$$

where $A_{\rm FB}$ is the forward-backward asymmetry of the tau pairs.

The polarization of the τ is measured by exploiting the parity violation of its decay (Tsai, 1971), which is mediated by the weak charged current. Due to the undetected neutrinos, the τ direction cannot be precisely reconstructed, and all polarization estimators have to be defined in the laboratory reference system. The τ polarization is obtained by fitting the measured distributions for each τ decay channel. Since decay distributions of a τ^- with given helicity are identical to those of a τ^+ with opposite helicity, the decay distributions of a τ^+ decaying at a polar angle θ can be simply added in the analysis to the distributions of the τ^- decaying at polar angle $\pi-\theta$.

In the case of the two-body decay $\tau\to\pi\nu$ and for the leptonic decays $\tau\to\ell\nu\overline{\nu}$ the only available observable of the τ decay is the energy (momentum) of the charged particle, and the decay distributions have simple forms (Jadach and Was, 1989). The hadronic decays $\tau\to(2,3)\pi\nu$ are more difficult and various methods (Rougé, 1990; Kühn and Mirkes, 1992; Davier *et al.*, 1993; Privitera, 1993) have been proposed to measure P_τ from the decay distributions. The decay modes with more than three pions in the final states, which correspond to about 10% of the branching ratio, are not useful for the polarization measurement because the description of the decays depends on model assumptions and because they cannot be selected with high purity.

The measurement of the polarization is dominated by the $\tau\to\pi\nu$ and $\tau\to2\pi\nu$ channels that have large sensitivity and large branching ratios and that can be selected with sufficiently high purity. The leptonic channels have smaller sensitivities because of the two undetected neutrinos in the final state.

When both τ's from the same Z decay are used in the polarization measurement the correlated decay distribution (Rougé, 1990) should be used to take into account the nearly 100% anticorrelated helicity of the two τ's. In practice this effect is small because typical selection efficiencies are of the order of 50%, and only in a relatively small fraction of the events are both τ's selected for the measurement.

The tau polarization has been measured by L3 (1994b), DELPHI (1995e), ALEPH (1996d), and OPAL (1996c), selecting $Z\to\tau^+\tau^-$ events and identifying the τ decay channel. The typical signature of the decay of the Z boson in two τ's is the detection of two almost back-to-back very collimated jets, with small charge multiplicity and with large missing energy and unbalanced transverse momentum due to the undetected neutrinos. The tau decay channels are separated using charge multiplicity, particle identification, photon counting, and the invariant mass of the visible state. For reviews see the papers of Bella (1995), Harton (1995), and Koumine (1995). No attempt is made to separate pions from kaons, since they have similar decay distributions. The large background from Z decays into electron and muon pairs is rejected mainly by applying cuts on the opposite jet in order to minimize the energy dependence of the efficiency.

The efficiencies and purities are very different in the various experiments, reflecting the different designs of the detectors, and have a strong dependence on the polar angle. Some experiments restrict the acceptance of the analyses to the central region, where particle identification and photon counting are more powerful, thus reducing sensitivity to the polarization asymmetry.

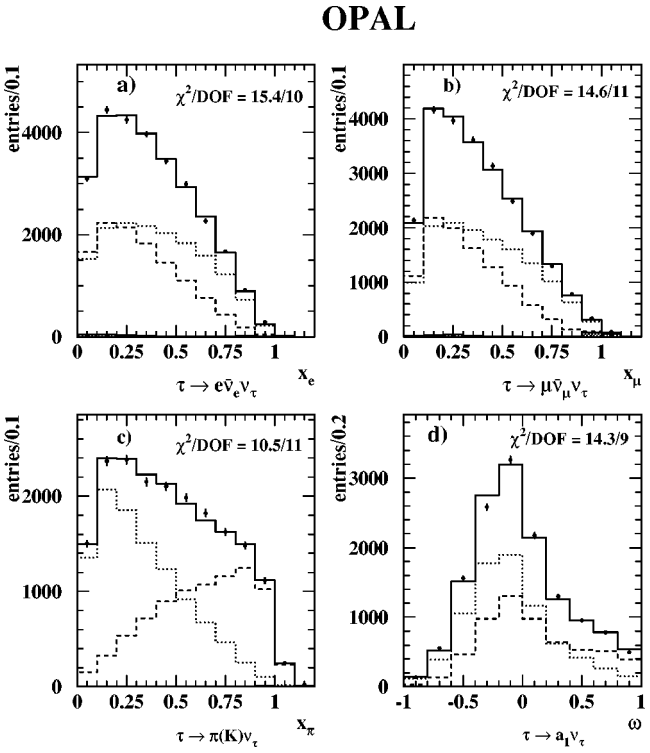

FIG. 30. Distribution in the kinematic variable used by OPAL (1996c) in the fits for four different τ decay channels where the data (shown with error bars) are integrated over the $\cos\theta$ range. Overlaying these distributions are Monte Carlo distributions for the positive-helicity (dashed) and negative-helicity (dotted) τ leptons and for their sum (solid) assuming the fitted value of P_τ. The small background from non $Z\to\tau\tau$ events is shown as a hatched histogram (almost invisible in the figure).

In the $\pi\nu$ channel the main source of background is from tau decays into $2\pi\nu$ when the photons from the π^o decays are not identified. The purity of the selected samples ranges from 84% to 94% depending on the experiment. In the $2\pi\nu$ channel the main source of background is from τ decays with more than one π^0. The purity of the selected samples ranges from 80% to 92%.

The charge, the momentum, and the direction of the charged particles are measured with the tracking devices, except for the experiments of L3, in which the energy deposits in the calorimeters are combined with the momentum measured by the tracking chamber. In ALEPH and DELPHI the photons are reconstructed as local maxima in highly segmented calorimeters, at a distance of a couple of centimeters from the impact point of the charged-particle track. L3 and OPAL fit the shower profile in the calorimeters, using reference histograms to subtract the energy coming from the hadronic shower of the nearby charged pion.

The fit for the polarization uses two sets of reference decay distributions, obtained applying the selection program to simulated data produced with the KORALZ Monte Carlo Simulation (Jadach *et al.*, 1991a, 1991b) and the full detector simulation. The two simulated sets are generated for positive and negative τ^- helicity, respectively (see Fig. 30). The polarization is extracted by performing a binned maximum likelihood fit of the measured distributions to the sum of the corresponding simulated distributions normalized by the coefficients $N(1+P_\tau)$ and $N(1-P_\tau)$.

With this procedure the main systematic errors are related to inconsistency between data and Monte Carlo simulations. Since the kinematic variables used in the fit depend on the momentum, an important source of systematic error is linked to the momentum dependence of the selection efficiency. In the $2\pi\nu$ channel the simulation of showers in the electromagnetic calorimeter is also an important source of systematic errors. Dependence on the model (Davier *et al.*, 1993) used for simulation of the decay $\tau\to 3\pi\nu$ does not affect the final result, since the weight of this channel is small.

The measurements obtained from the different τ decay channels are consistent with each other. They are averaged to obtain a more precise measurement of P_τ in a few separate $\cos\theta$ bins. The measured angular dependence is eventually fitted using Eq. (51) to extract $A_{\rm pol}$ and $A_{\rm pol}^{\rm FB}$. Since $A_{\rm FB}$ is small (~ 0.02) and well measured, its uncertainty is not propagated to the measurement of $A_{\rm pol}$ and $A_{\rm pol}^{\rm FB}$. In some experiments the small term $A_{\rm FB}$ is expressed in the fitting formula in terms of $A_{\rm pol}$ and $A_{\rm pol}^{\rm FB}$, using Eqs. (43), (44), and (45). The correlation between $A_{\rm pol}$ and $A_{\rm pol}^{\rm FB}$ is small ($\sim 4\%$). The experimental systematic errors are correlated among the different $\cos\theta$ bins of the angular fit, resulting in a smaller systematic error on $A_{\rm pol}^{\rm FB}$.

The measurements of $A_{\rm pol}$ and $A_{\rm pol}^{\rm FB}$ can be interpreted as measurements of $\mathcal{A}_\tau$ and $\mathcal{A}_e$ using Eqs. (43) and (44) after a small correction ($\simeq 0.003$) is applied to take into account the effects of the photon exchange, the $Z-\gamma$ interference, and initial and final-state radiation. Figure 31 shows the measurements of $\mathcal{A}_\tau$ and $\mathcal{A}_e$ and their averages including preliminary results presented at the Jerusalem conference (LEP Electroweak Group, 1997). The accuracy is typically limited by the statistical error. The measurements of $\mathcal{A}_e$ and $\mathcal{A}_\tau$ can be interpreted using Eq. (37) as measurement of the ratios $g_{V\ell}/g_{A\ell}$ for $\ell = e$ and τ. Assuming lepton universality, they can also be used for a precise determination of $\sin^2\theta_{\rm eff}^\ell$.

C. Measurement of $A_{\rm LR}$ at SLD

The left-right asymmetry [see Eq. (41)] has been measured with increasing precision by SLD (1994, 1997a) thanks to the possibility of operating SLC with a polarized electron beam (Phinney, 1993; Woods, 1995).

Polarized electrons are produced by a circularly polarized laser source hitting a GaAs photocathode, allowing SLC to be operated with an electron beam polarization of about 80%. The sign of the polarization is randomly chosen at the frequency of the SLAC machine pulse rate, so that the measurement is not affected by time variations of the apparatus efficiency.

The asymmetry of the cross sections is measured in a counting experiment. Hadronic Z decays are selected

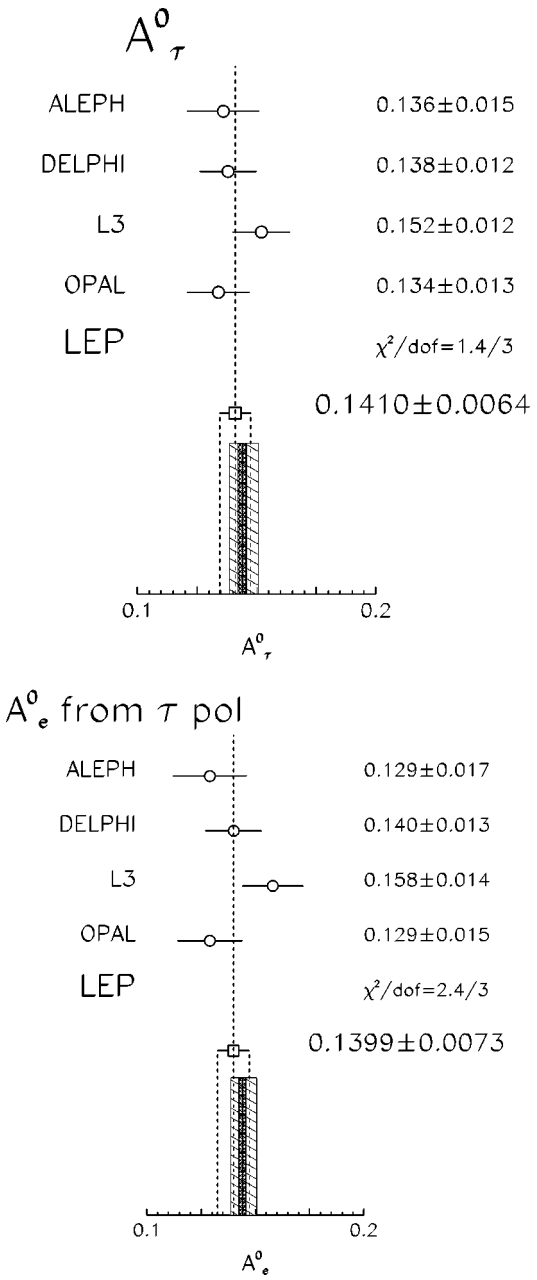

FIG. 31. The most recent measurements of $\mathcal{A}_\tau$ and $\mathcal{A}_e$ measured using τ polarization and the resulting LEP averages compared with the expectation of the standard model. The hatching code of the MSM prediction is described in Fig. 3.

with 99.9% purity, requiring at least four charged tracks, at least 22 GeV visible energy in the calorimeters, and an energy imbalance (ratio of vector to scalar energy sum in the calorimeter) less than 0.6. The events produced with left-handed (N_L) and right-handed (N_R) polarization are counted and their asymmetry $(N_L - N_R)/(N_L + N_R) \sim 0.12$ is measured. A small correction of $(0.06 \pm 0.06)\%$ is applied to take into account the residual contamination and small beam asymmetries.

The polarimeter measures the longitudinal polarization of electrons by Compton scattering after the interaction point with circularly polarized light from a Nd:YAG laser beam. The Compton-scattered electrons

TABLE VII. Relative systematic uncertainties (%) on the electron-beam polarization at SLD (Schumm, 1997). The 1996 result is preliminary and is expected to be reduced after the full analysis is completed.

Uncertainty	1994/5	1996
Laser polarization	0.2	0.2
Detector linearity	0.5	0.5
Detector calibration	0.29	0.30
Electronic noise	0.20	0.20
Interchannel consistency	–	0.80
Compton/SLD IP	0.17	0.18

are deflected by the first beam-line dipole after the interaction point and enter a threshold Cherenkov detector segmented in seven cells transverse to the beam line. The Compton cross-section asymmetry between the two laser polarizations is calculable within QED and is compared with the measured asymmetries, providing a redundant measurement of the product $(\mathcal{P})\mathcal{P}_\gamma$ of the electron and laser-beam polarization. The laser-beam polarization, typically 99.8%, is continuously monitored. The statistical accuracy on $(\mathcal{P})$ is of $\pm 1\%$ every three minutes. The relative systematic uncertainties in the polarization measurement are summarized in Table VII. The last entry of this table is the effect of the difference between the measured polarization and the polarization at the interaction point, mainly due to off-energy electrons which do not contribute to the effective luminosity (SLD, 1994).

The uncertainty on the polarization measurement gives the main systematic error for left-right asymmetry determination. The measured value of the asymmetry A_{LR} is slightly corrected by $+0.0029$ to take into account the effects of photon exchange, $Z-\gamma$ interference, and initial and final-state radiation. SLD (1997a) has recently obtained

$$A^0_{\mathrm{LR}} = 0.1545 \pm 0.0032, \tag{52}$$

which can be interpreted using Eq. (46) as a measurement of the ratios g_{Ve}/g_{Ae} and yields a very precise measurement of $\sin^2\theta^{\ell}_{\mathrm{eff}}$.

D. Universality of the neutral-current couplings

Lepton universality requires that the vector ($g_{V\ell}$) and the axial ($g_{A\ell}$) couplings of the neutral current to electron, muon, and tau be equal. The sum of the squares of the couplings is determined by measuring the partial width of the decay $Z \to \ell^+\ell^-$ (see Sec. II.E), using Eq. (11). The ratio of the vector and axial couplings is determined by measurements of the asymmetry $\mathcal{A}_\ell$ defined in Eq. (37) and described in the previous sections.

Figure 32 compares the vector and axial coupling constants of the neutral current to the different lepton flavors: the vector coupling of the muon is less precise than those of the electron and tau, since it is constrained only by the measurement of $A^0_{\mathrm{FB}}(\mu)$. The measurements are

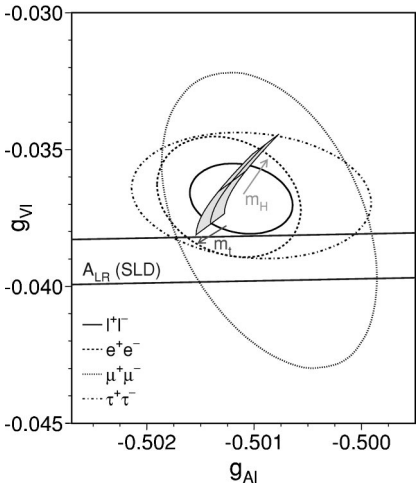

FIG. 32. 68% contours of $g_{V\ell}$ vs $g_{A\ell}$ for $\ell=e,\mu,\tau$ measured by LEP and the constraint from the SLD measurement of $\mathcal{A}_e$ are compared with the prediction of the standard model.

in good agreement, and lepton universality is tested to 0.2% for axial couplings and to 7% for the small vector coupling:

$$\frac{g_{V\mu}}{g_{Ve}}=0.932\pm0.087\,\frac{g_{A\mu}}{g_{Ae}}=0.999\pm0.0016,$$

$$\frac{g_{V\tau}}{g_{Ve}}=0.949\pm0.044\,\frac{g_{A\tau}}{g_{Ae}}=0.9998\pm0.0018.$$

E. Quark forward-backward asymmetry

The measurement of the forward-backward asymmetry of the decay $Z\to q\bar{q}$ provides a very precise determination of $\sin^2\theta^{\ell}_{\rm eff}$. Indeed, as shown in Table VI, the sensitivity of fermion forward-backward asymmetries to the mixing angle is particularly enhanced for quarks. A further advantage of the quark asymmetry is that dependence on the actual value of the center-of-mass energy (see Appendix) is much weaker for quarks than for leptons because of their smaller electric charge.

The extraction of $\mathcal{A}_e$ and $\sin^2\theta^{\ell}_{\rm eff}$ from quark forward-backward asymmetries requires a knowledge of $\mathcal{A}_q$, which is evaluated in terms of $\sin^2\theta^{\ell}_{\rm eff}$ using Eqs. (37) and (10):

$$\frac{g_{Vq}}{g_{Aq}}=1-\frac{2Q_q}{I_q^3}(\sin^2\theta^{\ell}_{\rm eff}+C_q).$$

The residual vertex correction C_q is computed in the minimal standard model. For $udsc$ quarks this correction is small and has very little dependence on the parameters of the model, while for b it depends on the top mass because of the additional $Z\to b\bar{b}$ vertex corrections (see Fig. 2) and it is $+0.0014$ for a top mass of 175 GeV (Hollik, 1993, 1995).

Measuring the asymmetry for a given quark requires evaluating its original charge from particles detected in the experiments. When the correlation from the charge of primary hadrons and their decay products is exploited, for instance by means of prompt leptons or D*, the decay products themselves provide the separation of the interesting events from other quark species. An alternative method is to employ an efficient method of event tagging, such as the lifetime b tagging described in Sec. III.A.1, and to measure the original quark charge with a jet charge technique.

Most of the measurements given in the following sections rely on the heavy-flavor tagging methods described in Sec. III.A. The precision obtained on the b and c asymmetries requires a careful assessment of the correction needed to extract $A_{\rm FB}^0$ as defined in Eq. (45) from the observed experimental asymmetry. This includes the treatment of QCD corrections.

The weak mixing angle can also be determined from the forward-backward jet charge asymmetry of inclusive hadrons without explicit tagging of individual flavors. These measurements, which require the detailed understanding of inclusive hadron properties, are described in the last section.

1. Measuring the asymmetry of b and c quarks from decays into leptons

In primary semileptonic decays of b hadrons there is a natural correlation between the sign of the lepton and the particle-antiparticle nature of the original b quark. Therefore a pure sample of $b\to\ell$ decays, obtained with lepton tagging techniques, can be used to measure the b forward-backward asymmetry. Experimentally the best definition of the primary quark direction is provided by the thrust axis, especially if both charged and neutral particles are used.

The thrust axis is normally taken as pointing to the hemisphere containing the lepton; then it is signed with the charge Q of the lepton, yielding the following estimator for the b quark direction:

$$\cos\theta_b=-Q\cos\theta_{\rm thrust}.$$

In a sample of semileptonic b decays, the asymmetry $A_{\rm FB}^{\rm obs}$ can be measured from the odd term $A_{\rm FB}$ in the angular distribution of Eq. (49). Provided the lepton and antilepton identification efficiencies are the same, the acceptance term $C(\cos\theta_b)$ is symmetric and does not contribute to the evaluation of the asymmetry if the minimum likelihood method is used to fit the angular distribution. An example of acceptance-corrected angular distribution can be seen in Fig. 33.

Even in a totally pure sample of $b\to\ell$ decays, the observed asymmetry $A_{\rm FB}^{\rm obs}$ is diluted with respect to the true b asymmetry by the presence of $B^0\overline{B}^0$ oscillations. The observed asymmetry is lowered by a factor $(1-2\chi)$ where χ is the average b mixing parameter, defined as the probability that a produced b state yields a $\bar{b}$ state. The observed asymmetry is further diluted by the presence of the $b\to c\to\ell$ cascade, which yields the wrong charge, hence reversing the direction of the b quark, and by charm semileptonic decay, which is sensitive to c asymmetry. This can be expressed as

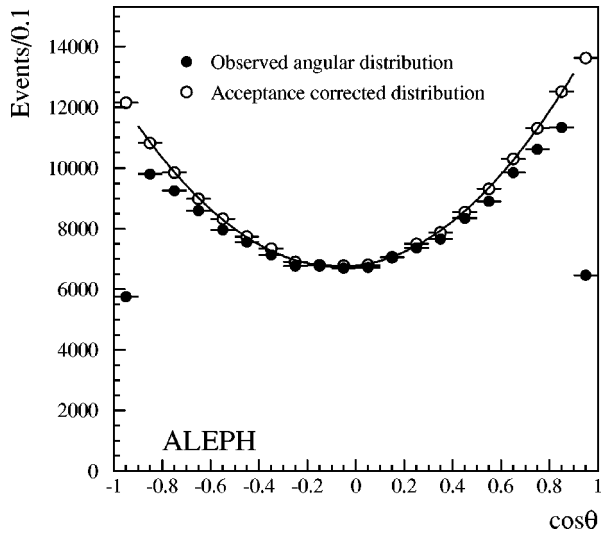

FIG. 33. Forward-backward b asymmetry from inclusive leptons. The angular distribution are as seen by ALEPH (1994a) before and after acceptance corrections.

$$A_{\mathrm{FB}}^{\mathrm{obs}}=(1-2\chi)(\eta_{b\to\ell}+\eta_{b\to\tau\to\ell}+\eta_{b\to\bar{c}\to\ell}-\eta_{b\to c\to\ell})A_{\mathrm{FB}}^{b}-\eta_{c\to\ell}A_{\mathrm{FB}}^{c}+\eta_{\mathrm{bkg}}A_{\mathrm{FB}}^{\mathrm{bkg}},$$

where the η_i are the fractions of lepton candidates from a given source and A_{FB}^{b}, A_{FB}^{c}, and $A_{\mathrm{FB}}^{\mathrm{bkg}}$ are the true b asymmetry, the c asymmetry, and the effective background asymmetry due to lepton fakes, respectively. The small components due to a τ from a b decay ($b\to\tau\to\ell$) and from $b\to c\bar{c}s$ followed by $\bar{c}\to\ell^-$ (indicated as $b\to\bar{c}\to\ell$) have the correct sign. The background asymmetry $A_{\mathrm{FB}}^{\mathrm{bkg}}$ is small but nonzero because of correlations in sign between high-$p_\perp$ hadrons and the original quark. This effect is normally evaluated by Monte Carlo simulations tuned on data.

The use of the above relation to extract the b asymmetry requires assumptions about the c asymmetry or an independent measurement of the c asymmetry itself. This can be avoided if, instead of applying a $p_\perp$ cut, a fit of the lepton distribution in the $(p,p_\perp)$ plane is performed by taking into account the lepton composition in each bin of the plane. In this way the c asymmetry becomes a free parameter of the fit and can be evaluated from low-$p_\perp$ leptons. The typical correlation between b and c asymmetry, when measured simultaneously in lepton fits, is 20%. The precision of present measurements (OPAL, 1993b, 1996a; ALEPH, 1994a, 1996b; L3, 1994a; DELPHI, 1995c) of the b (and c) asymmetry using leptons is limited by the statistics of the sample, the main systematic error being the uncertainty on the mixing parameter χ. It should be pointed out that modeling assumptions about the lepton spectra, which are necessary in order to calculate the η_i fractions, are not the main source of systematic errors in the b asymmetry. The effects of these assumptions on χ and on the semileptonic branching ratios $\mathbf{BR}(b\to\ell)$ and $\mathbf{BR}(b\to c\to\ell)$ work out in opposite directions, so that they partially cancel.

2. Measuring c quark asymmetry from D*

The charge correlation between prompt D* and c quarks can be exploited to measure the c asymmetry in a way similar to the b asymmetry for high-$p_\perp$ leptons. Here the main discriminating variable between the c and b sectors is the scaled energy X_E (see Sec. III.A.4). A cut on X_E allows us to select high-energy D* and therefore a rather pure sample of $Z\to c\bar{c}$. The typical purity for $X_E>0.5$ is about 80%. The thrust axis direction, signed by the D* charge, is used and a maximum likelihood fit to the log angular distribution is performed.

Since D*'s are selected by means of invariant-mass cuts in channels that have a sizable amount of background, particular care has to be taken to evaluate correctly the background contamination, which dilutes the asymmetry. For this purpose event-mixing techniques (i.e., taking the D meson combination and the slow pion from opposite hemispheres or from different events) are used to evaluate the background shape in an unbiased way. This allows one to treat partially reconstructed events and signal reflections which, being charge-correlated to the original quark, should not be counted as background. Sidebands of invariant-mass peaks or mixed events themselves can be used to evaluate the background asymmetry, which is generally close to zero.

When a hard cut on X_E is applied, the effect of the b asymmetry, which originates from the charge correlation in the $b\to$D* process, has to be taken into account and subtracted using an independent measurement of A_{FB}^{b} (ALEPH, 1995a). Alternatively, the X_E shape can be fitted to a c and b component and both c and b asymmetries can be measured (OPAL, 1993c; 1997b; DELPHI, 1995a). In all cases the effect of b mixing on the b asymmetry needs to be accounted for in a way that differs from an unbiased sample: the $b\to$D* process preferentially selects B_d hadrons, causing the effective χ parameter to be dominated by χ_d.

3. Measuring b quark asymmetry from jet charge

Tagging methods based on the long lifetime of b hadrons give the best performance in selecting $Z\to b\bar{b}$ decays (see Sec. III.A.1). As lifetime tagging does not directly provide a way to separate b from anti-b quarks, a charge estimator has to be built from the b hadronization and decay products. The event is divided into two hemispheres, using the thrust axis, and for each hemisphere the jet charge is defined as

$$Q_j=\frac{\Sigma_i|p_{\parallel i}|^{\kappa}q_i}{\Sigma_i|p_{\parallel i}|^{\kappa}}, \tag{53}$$

where $p_{\parallel i}$ is the longitudinal component of the charged-particle momentum i with respect to the thrust axis, q_i is the charge of the particle, and the sum runs over the charged particles in a given hemisphere. The κ parameter weighs the momentum of each particle and is set to a value giving the smallest statistical error to the measurement. This quantity is used in a statistical way, tak-

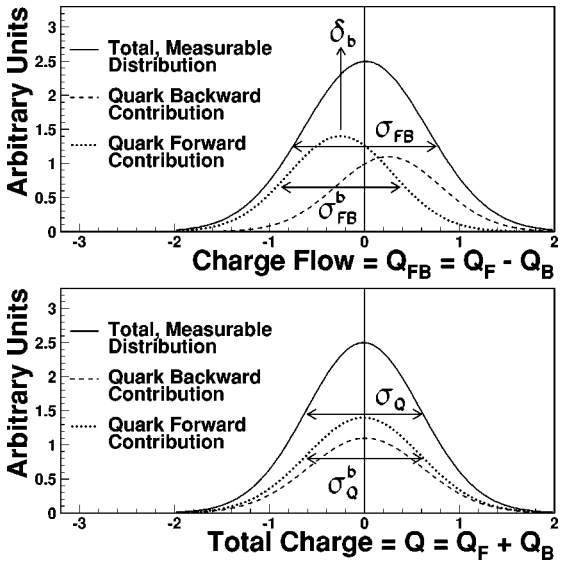

FIG. 34. Distributions of $Q_{\rm FB}$ and Q in the measurement of the b asymmetry from jet charge by ALEPH (1994b). The quantities $\sigma^b_{\rm FB}$ and σ^b_Q are the widths of $Q_{\rm FB}$ and Q for a b quark going forward. The charge separation (δ_b) can be measured by comparing the total width of $Q_{\rm FB}$ to the width of Q.

ing advantage of the fact that fragmentation and decay products retain some memory of the original quark charge.

The average difference between jet charges in the forward and backward hemispheres can be related to the b asymmetry through the relation

$$\langle Q^b_{\rm FB}\rangle \equiv \langle Q_{\rm F} - Q_{\rm B}\rangle = \delta_b A^b_{\rm FB}, \tag{54}$$

which holds for a pure sample of $Z\to b\bar{b}$ decays. The quantity δ_b is called the b charge separation, and it must be known in order to extract the asymmetry. For a pure sample of a given quark flavor, the charge separation δ_f can be measured from data by comparing the width of the $Q_{\rm FB}=Q_{\rm F}-Q_{\rm B}$ distribution to the width of $Q=Q_{\rm F}+Q_{\rm B}$, which is narrower and has an average value close to zero, as can be seen in Fig. 34. The procedure is explained in detail in the papers of the ALEPH (1994b) and OPAL (1995d) collaborations.

Actually, lifetime-tagged samples are contaminated by lighter quarks, in particular charm, and therefore the b asymmetry has to be extracted from the more general relation

$$\langle Q_{\rm F} - Q_{\rm B}\rangle = \sum_{f=u,d\ldots}^{b} \mathcal{P}_f C_f \delta_f A^f_{\rm FB}, \tag{55}$$

where $\mathcal{P}_f$ are the purities for each flavor ($\mathcal{P}_{u,d,s,c}\ll 1$) and C_f are acceptance factors which depend on the quark flavor, since the lifetime tagging biases the polar angle distribution of different flavors in different ways. The charge separations for light quarks cannot be measured on data, therefore extraction of the b asymmetry is affected by Monte Carlo-dependent small corrections.

This method allows one to measure the b asymmetry with a statistical precision similar to the method based on semileptonic decays: lifetime tagging selects b hadrons with much higher efficiency, but this is compensated for by the reduced sensitivity of the charge estimator. An advantage of this technique is that the effect of $B^0\overline{B}^0$ oscillations is included in δ_b, which is measured with data. Hence an explicit correction for b mixing is not needed. On the other hand, since the asymmetry is measured from the charge flow in forward versus backward hemispheres, the angular acceptance has to be studied, and it is a source of systematic error, in contrast to the measurement based on semileptonic decays. The main systematic errors arise from uncertainties in the fragmentation modeling used to evaluate the charge separations δ for light quarks and from detector biases for the δ_b measurement. Published measurements of the b asymmetry using jet charge can be found in papers by ALEPH (1994b), DELPHI (1995c), and OPAL (1995d, 1997c).

4. Corrections to the measured heavy-quark asymmetries

The extraction of the effective electroweak mixing angle requires evaluation of the corrected b and c asymmetries $A^0_{\rm FB}(b)$ and $A^0_{\rm FB}(c)$, from the measured asymmetries. Corrections have to be applied for QED initial and final-state radiation and for the effect of photon exchange and Z-γ interference, similarly to what is done for lepton forward-backward asymmetries. The measured asymmetry is extrapolated to $\sqrt{s}=M_Z$ assuming the standard-model energy dependence.

Heavy-quark asymmetries are also affected by radiative corrections due to strong interactions (Djouadi *et al.*, 1990; Altarelli and Lampe, 1993; Djouadi *et al.*, 1995), and one-loop QCD corrections are sufficient at the level of precision of present measurements. They consist of virtual vertex corrections and gluon bremsstrahlung corrections to the final states. The latter require a correct definition of the b quark direction, which should closely match the experimental definition based on thrust axis reconstruction. This has been done in the paper by Djouadi *et al.* (1995), where full one-loop corrections, including quark mass effects, have been calculated. The correction can be expressed as a factor modifying the asymmetry by $[1-C_f(\alpha_s/\pi)]$, where C_f is a flavor-dependent coefficient. Typical values of b and c quark masses yield $C_c=0.87$ and $C_b=0.79$. The experimental cuts bias the theoretical corrections. For instance, the momentum cut that is applied in lepton tagging selects events with reduced gluon radiation and thus has the effect of lowering the correction (Abbaneo *et al.*, 1997). QCD corrections do not apply when the b asymmetry is measured with a jet charge technique as described in Sec. IV.E.3. In this case the b charge separation, measured with data, naturally incorporates the effect of hard-gluon radiation. The sizes of the theoretical corrections used to extract the tree-level asymmetries are shown in Table VIII.

Averaging several measurements of b and c forward-backward asymmetries requires a correct treatment of the correlations between different techniques and different experiments. Still this is not as crucial as for other

TABLE VIII. Relative corrections to the experimental asymmetries.

Effects	Relative corrections	
	b asymmetry	c asymmetry
QED I.S.R.	+4.4%	+15.6%
QED F.S.R.	+0.02%	+0.08%
γ exchange and Z-γ interference	−0.003%	−0.1%
Final-state QCD corr.	+3.1%	+3.6%
Energy corr. at peak	−1.5%	−5.1%

heavy-flavor measurements, since all the results are dominated by the statistical error. The present world averages for the corrected asymmetries, as given by the LEP Electroweak Group (1997), are

$$A_{FB}^0(b) = 0.0983 \pm 0.0024,$$

$$A_{FB}^0(c) = 0.0739 \pm 0.0048.$$

There is a 10% correlation between the two results. The averages include preliminary results presented at the Jerusalem Conference. The most precise results, together with the average, are compared to the standard model prediction in Fig. 35.

5. Measurement of jet charge asymmetry in $Z \to q\bar{q}$

The measurement of jet charge was introduced in Sec. IV.E.3 for a sample of hadronic Z decays highly enriched in $Z \to b\bar{b}$. The same technique can be applied to the full $Z \to q\bar{q}$ sample. If heavy-quark tagging is not used, Eq. (55) can be rewritten as

$$\langle Q_{FB} \rangle \equiv \langle Q_F - Q_B \rangle = C \sum_{f=u,d\ldots}^{b} \delta_f A_{FB}^f \frac{\Gamma_{f\bar{f}}}{\Gamma_{had}}$$

$$= C \frac{3}{4} \sum_{f=u,d\ldots}^{b} \delta_f \mathcal{A}_e \mathcal{A}_f \frac{\Gamma_{f\bar{f}}}{\Gamma_{had}} \qquad (56)$$

where C is the geometrical acceptance. This relation is a linear function of $\mathcal{A}_e$ and can be used to extract the electroweak mixing angle from a measurement of the jet charge forward-backward asymmetry.

Knowledge of the five charge separations is crucial for a determination of $\sin^2\theta_{eff}$. At parton level δ_f is equal to twice the quark charge $(2q_f)$ but hadronization and decays dilute the charge separation in a flavor-dependent way: for example, the charm charge separation gets particularly reduced by the presence of the soft pion in the D^{*+} decay. The soft pion retains memory of the original charm charge, but being low momentum it gets a low weight from the jet charge definition [see Eq. (53)]. The δ_f's can be computed with Monte Carlo simulations of the hadronization process and of the charge flow in the detector (ALEPH, 1991a; DELPHI, 1992a; OPAL, 1992).

Measuring at least some of the δ_f's with data greatly increases the confidence level on the $\sin^2\theta_{eff}$ extraction. As is explained in Sec. IV.E.3, δ_b can be measured from

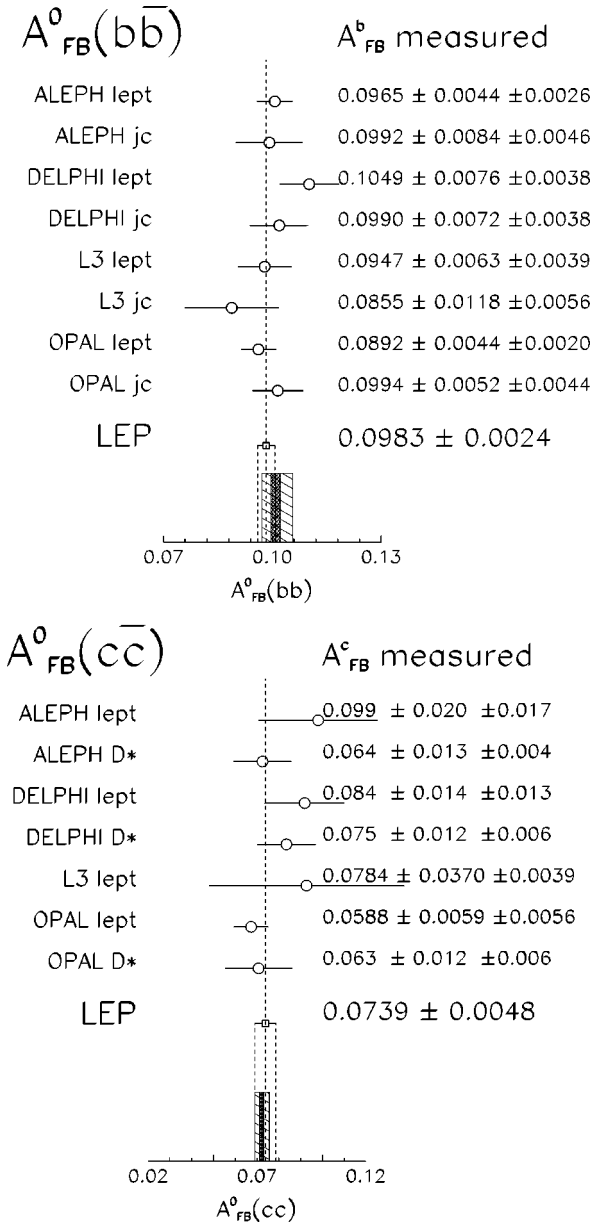

FIG. 35. The most recent A_{FB}^b, A_{FB}^c measurements and the resulting LEP average. The measured asymmetries have been readjusted to common values for the relevant parameters (like the χ mixing parameter) and translated into pole asymmetries. Only measurements at the Z peak are shown. The displayed error does not include systematic errors, which are common to at least two measurements. They are compared with the prediction of the standard model. The hatching code of the MSM prediction is described in Fig. 3.

pure samples of $Z \to b\bar{b}$ decays. In the paper by ALEPH (1996a) a novel technique was employed to evaluate δ_c from lifetime-tagged samples with varying charm content, as well as from fast-D^{*+} tagged samples. Individual charge separations for lighter quarks cannot be measured separately, but the average δ_{uds} can be inferred from the difference in width of the $\langle Q_F - Q_B \rangle$ and $\langle Q_F + Q_B \rangle$ distributions or, equivalently, from forward-backward jet charge correlations (ALEPH, 1994b, 1996a). Detailed Monte Carlo studies are needed to dis-

entangle the δ_u, δ_d, and δ_s contributions. In particular, the simulation has to be tuned to measured kaon and Λ production in order to have a realistic description of strangeness production. Indeed, the uncertainty on the γ_s parameter, which controls the relative amount of s versus u and d quark production from the sea, is one of the main sources of systematic error (ALEPH, 1991a, 1996a; DELPHI, 1992a; OPAL, 1992).

The present world average of $\sin^2\theta^{\ell}_{\rm eff}$ from the jet charge asymmetry, including new preliminary results by Ezion (1997), is

$$\sin^2\theta^{\ell}_{\rm eff}=0.2322\pm0.0010,$$

where the error is dominated by the uncertainty in fragmentation and decay modeling.

6. Measurements of heavy-quark forward-backward polarized asymmetries

The measurement of the combined final-state couplings $\mathcal{A}_b$ is complementary to the determination of R_b (Boulware and Finnel, 1991). Furthermore, it is only weakly dependent on $\sin^2\theta^{\ell}_{\rm eff}$ ($\delta\mathcal{A}_b\approx-0.63\,\delta\sin^2\theta^{\ell}_{\rm eff}$), thus probing different electroweak corrections than $\mathcal{A}_e$ (Blondel *et al.*, 1988).

The polarized forward-backward asymmetry of b and c quarks was measured by the SLD experiment using flavor-tagging techniques very similar to that used for unpolarized asymmetries (see Secs. III and IV.E). Lifetime tagging coupled to jet charge provides the best determination of $\mathcal{A}_b$ (SLD, 1995b, 1997c). The fit of the inclusive lepton spectra provides a simultaneous determination of $\mathcal{A}_b$,$\mathcal{A}_c$ (SLD, 1995c, 1997d), while D and D^{*+} mesons are used to measure $\mathcal{A}_c$ (SLD, 1995a). Lifetime-tagging analyses based on the correlation between the charge of identified kaons and the original primary b and c quarks provide additional measurements of $\mathcal{A}_b$ and $\mathcal{A}_c$ (SLD, 1997b, 1997e). These measurements are corrected for QCD effects. The correction depends on the flavor-tagging technique and it is about 3%, similar to the unpolarized case (see Sec. IV.E.4). A nice feature of forward-backward polarized asymmetries is their weak dependence on the center-of-mass energy within a few GeV around the Z pole (Blondel *et al.*, 1988). This makes the measurement essentially independent of QED initial-state radiation. The SLD results are combined (LEP Electroweak Group, 1997), yielding

$$\mathcal{A}_b=0.900\pm0.050,$$

$$\mathcal{A}_c=0.650\pm0.058,$$

with an 8% $\mathcal{A}_b$,$\mathcal{A}_c$ correlation.

The $\mathcal{A}$ parameters for b and c quarks can be evaluated at LEP from the unpolarized b and c asymmetries using Eq. (40) and the value of $\mathcal{A}_e$ derived from $A^0_{\rm FB}(\ell)$, the tau polarization, and $A^0_{\rm LR}$ (see Sec. IV.F), obtaining $\mathcal{A}_b=0.871\pm0.025$ and $\mathcal{A}_c=0.654\pm0.045$. These values are consistent with the direct measurements from SLD and can be averaged with them, giving

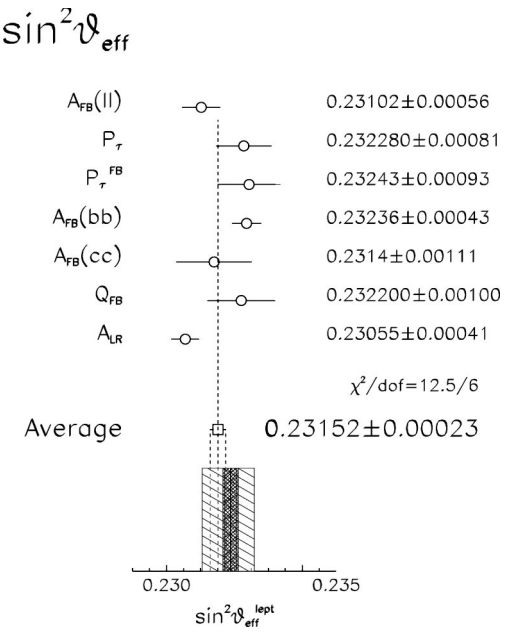

FIG. 36. The most precise determinations of $\sin^2\theta^{\ell}_{\rm eff}$ and their average compared with the prediction of the standard model. The hatching code of the MSM prediction is described in Fig. 3.

$$\mathcal{A}_b=0.877\pm0.023$$

$$\mathcal{A}_c=0.653\pm0.037,$$

to be compared to the standard-model prediction of $\mathcal{A}_b=0.935$ and $\mathcal{A}_c=0.668$. The measurement of the c asymmetry is in agreement with the prediction of the standard model, while the measurement of $\mathcal{A}_b$ is 2.5 standard deviations lower than the predicted value.

F. Comparison of the different determinations of $\sin^2\theta^{\ell}_{\rm eff}$

The most precise measurements of the asymmetries presented in the previous sections can be used to compute $\sin^2\theta^{\ell}_{\rm eff}$. A compilation of the various measurements is shown in Fig. 36. The average of the seven measurements is

$$\sin^2\theta^{\ell}_{\rm eff}=0.23152\pm0.00023,$$

with a χ^2 of 12.5 for six degrees of freedom corresponding to a confidence level of 5%.

There are two classes of measurements. The first class contains $A^0_{\rm FB}(\ell)$, the measurements of $\mathcal{A}_e$ and $\mathcal{A}_\tau$ from tau polarization, and the measurement of $A^0_{\rm LR}$ done at SLC, which can be interpreted in terms of the lepton asymmetry $\mathcal{A}_\ell$ and of $\sin^2\theta^{\ell}_{\rm eff}$ with the only assumption that of lepton universality. The second class contains the other three measurements. The derivation of the sine from them requires a knowledge of the $\mathcal{A}_q$ terms, which as discussed in Sec. IV.E, have a very mild dependence on $\sin^2\theta^{\ell}_{\rm eff}$ in the standard model.

The extraction of $\mathcal{A}_\ell$ from $A^0_{\rm FB}(\ell)$, $\mathcal{A}_e$, $\mathcal{A}_\tau$, and $A^0_{\rm LR}$ gives $\mathcal{A}_\ell=0.1505\pm0.0023$ with a χ^2 of 6.0 for three de-

grees of freedom corresponding to a confidence level of 11%. This value of $\mathcal{A}_\ell$ gives

$$\sin^2\theta^\ell_{\rm eff}=0.23108\pm0.00030.$$

The differences between this model-independent value of the sine and those derived from $A^0_{\rm FB}(b)$ and $A^0_{\rm FB}(c)$ are as follows: $\Delta\sin(b)=-0.00128\pm0.00052$ and $\Delta\sin(c)=-0.00032\pm0.00115$. The 2.5σ discrepancy shown by $\Delta\sin(b)$ is very strongly correlated with the discrepancy (2.5σ) already discussed in Sec. IV.E.6, where a value of $\mathcal{A}_b$ was extracted from $A^0_{\rm FB}(b)$ and compared to the standard-model prediction. These discrepancies are caused by the combination of two uncorrelated effects: as shown in Fig. 36, the effective mixing angle derived from the LEP b forward-backward asymmetry is high compared to the average, while the measurement from $A^0_{\rm LR}$, which dominates the model-independent value, shows the opposite behavior.

V. *W* MASS MEASUREMENT

The precise measurement done at the Z pole can be used to predict the mass of the W boson within the framework of the standard model. The comparison between the predicted and the measured masses is one of the most stringent tests of the minimal standard model. In the following sections, the direct measurement of the W mass is briefly described. The indirect determination of the W-to-Z mass ratio is also discussed, using the measured ratio of neutral- and charged-current interactions on an isoscalar target.

A. Measurement of the *W* mass at $p\bar{p}$ colliders

At proton-antiproton colliders W bosons are produced with a large cross section by quark-antiquark annihilation. W decays (into electron or muon plus neutrino) are selected by requiring an isolated lepton with high momentum, large transverse missing energy caused by the undetected neutrino, and additional cuts on the energy of the recoiling hadronic system. This yields a large sample with a background of a few percent.

Since the longitudinal component of the missing momentum cannot be measured, there is not sufficient information to reconstruct the mass on an event-by-event basis. The W mass M_W is extracted from a model-based fit of the Jacobian line shape of the transverse mass M_W^T distribution (see Fig. 37). The transverse mass is analogous to the invariant mass except that only the particle momentum components transverse to the beams are used:

$$M_W^T=\sqrt{2p_T^{\rm lepton}p_T^{\nu}(1-\cos\phi)}, \tag{57}$$

where ϕ is the angle between the lepton and the missing momentum measured on the transverse plane.

The W mass has been measured with this method by the UA2 Collaboration (1992) and more recently by CDF (1995a, 1997) and DØ (1997a). The measurement of CDF is based on the result of Run 1-A, from which they selected about $6000 W\to e\nu$ candidates and $3000 W\to\mu\nu$ candidates. The measurement of DØ is based on the full data sample, from which they selected about $33000 W\to e\nu$ candidates.

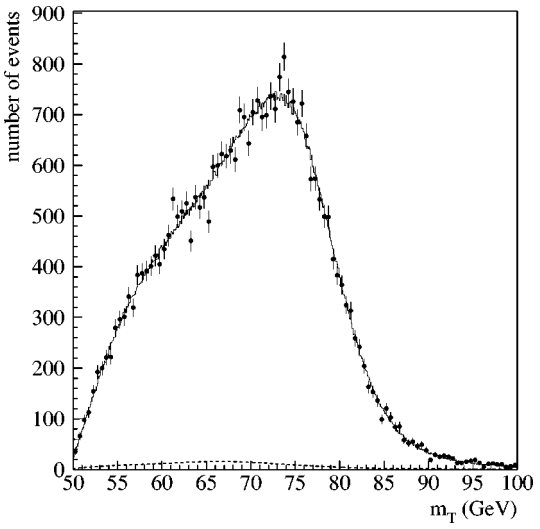

FIG. 37. Transverse mass distribution in run 1-b W sample of DØ (1997a).

The largest single source of systematic error in these measurements is the determination of the absolute energy scale. The momentum scale of the central detector of CDF is calibrated using a large sample of J/ψ decays to a precision of 6×10^{-4}, contributing only 50 MeV to the W mass measurement. This calibration is transferred to the calorimeter using high-energy electrons and correcting for radiation in the tracker. This procedure contributes an additional 110 MeV scale uncertainty on M_W in the electron channel.

The DØ calorimeter is calibrated using test-beam data, Z and J/ψ decays to electron pairs and π^0 decays. The uncertainty on the energy scale results in a 77-MeV uncertainty on M_W dominated by the limited statistics of Z decays.

Other sources of systematic errors enter through the modeling of the M_W^T distribution used for the fit. The most relevant are limited knowledge of the electron energy and muon momentum resolutions, simulation of the detector response to the recoiling hadronic system, and distributions of the W transverse and longitudinal momentum. The first two effects are calibrated using Z decays, while the latter is constrained by also using the measurement of the forward-backward charge asymmetry in W decays. The total systematic error on the modeling is about 130 MeV for the CDF measurement in the electron channel, 120 MeV for the CDF measurement in the muon channel, and 130 MeV for the DØ measurement in the electron channel, with small correlations. The average of the measurements of the W mass from the $p\bar{p}$ colliders given at the Lepton Photon Symposium in Hamburg (Kim, 1997) is $M_W=80.41\pm0.09$ GeV.

B. Measurement of the *W* mass at LEP

Pairs of W bosons have been recently produced at LEP in two runs at center-of-mass energies of 161 and

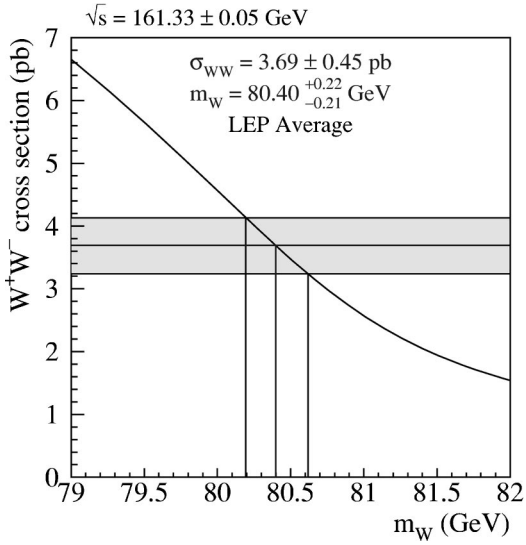

FIG. 38. Dependence of the WW cross section on M_W at 161 GeV.

172 GeV. The measurement of the cross section at threshold ($\sqrt{s}\sim 2m_W+0.5$ GeV) provides a sensitive measurement of the W mass because the dependence of the cross section on the mass is mainly of kinematical origin. However, since the cross section is measured only at one point, the determination of the mass can only be done within the framework of the standard model, though with very small dependence on its input parameters. At 172 GeV the W mass is measured from direct reconstruction of the final state.

The event selection is simple for final states where at least one W decays into a lepton plus neutrino. The final state $\ell\ell\nu\nu$ (11%) has two acoplanar leptons and missing energy, while the final state $q'\bar{q}\ell\nu$ (43%) has an isolated lepton, two hadronic jets, and isolated missing energy. These channels can be selected with high efficiency and very low background. The totally hadronic channel (46%) has a large QCD background that is less relevant at 172 GeV, where the WW cross section is larger. The events are selected using many topological properties that are combined in a single distribution (neural networks, likelihood function, weights), which is compared with the predicted distributions for the signal and the background obtained with Monte Carlo simulation.

In the 161-GeV data sample, each experiment (OPAL, 1996d; ALEPH, 1997e; DELPHI, 1997b; L3, 1997c) selected typically 5 events in the channel $\ell\ell\nu\nu$ and 15 events in the $q'\bar{q}\ell\nu$ channel. The small (few %) contribution of four-fermion events not resulting in two real W's in the final state is subtracted using Monte Carlo simulation. The cross sections measured in each channel are combined using the standard model branching ratios for the W decays. The results of the four experiments are averaged, giving a cross section for production of two *real* W's in the final state (usually called the CCO3 cross section) of 3.69 ± 0.45 pb. This corresponds (see Fig. 38) to $M_W=80.40\pm 0.22$ GeV. The main systematic error on the W mass comes from uncertainty on the beam energy and is around 30 MeV.

At 172 GeV the W mass is measured by direct reconstruction, using the $q'\bar{q}\ell\nu$ and the fully hadronic channels. A value of the W mass is extracted for each event using the energies and the directions of the reconstructed jets and leptons, applying the constraints of energy and momentum conservation and imposing, in some cases, the equality of the two W masses. With this procedure, the absolute energy scale of the W mass is constrained by the beam energy. The measured distribution is compared with the Monte Carlo expectations for many W masses to fit M_W. The simulation predicts a bias of about 200 MeV, mainly due to the combined effects of the constraints and initial-state radiation. Each Collaboration selected about 80 WW pairs for this measurement, which is statistically limited. The main systematic errors come from the simulation of the jets and, in the fully hadronic events, from final-state effects involving quarks or hadrons from the decays of the two W's (color reconnection, Bose-Einstein effects). The LEP average mass with direct reconstruction is $M_W=80.53\pm 0.18$ GeV.

The two values of the W mass measured at LEP with two different techniques are comparable in precision. Their average is $M_W=80.48\pm 0.14$ GeV. This average is in good agreement with the average of the measurements done at $p\bar{p}$ colliders.

C. Neutrino-nucleon scattering

The quantity $R_\nu=\sigma^\nu_{\rm NC}/\sigma^\nu_{\rm CC}$, i.e., the ratio between the neutral- and charged-current interactions of neutrinos on an isoscalar target, provides a precise indirect measurement (Llewellyn Smith, 1983) of s^2_W with very little dependence on other unknown parameters of the theory (Marciano and Stirlin, 1980; Stuart, 1987).

Blondel (1990) has shown that within the standard model this ratio can be written as

$$R_\nu=\left(\frac{M_W}{M_Z}\right)^4\frac{1}{2}\,\frac{1-2s^2_W+10/9s^4_W(1+r)}{1-2s^2_W+s^4_W}, \tag{58}$$

where $r=0.38\pm 0.01$ is the ratio between neutrino- and antineutrino-induced charged currents. By numerical accident, the dependence of the last term of Eq. (58) on s^2_W is very weak and

$$R_\nu=\left(\frac{M_W}{M_Z}\right)^4\frac{1}{2}(1+0.050\pm 0.003)$$

provides a precise indirect measurement of the ratio between the W and Z masses. The largest theoretical errors in Eq. (58) come from uncertainties in the distributions of strange and charm quark seas in the nucleon.

Events induced by the muon neutrino beam in thick calorimeters are classified as NC or CC events using the event length, thus exploiting the characteristic penetration of the muons produced in charged currents. The main experimental systematic error comes from the model needed for subtraction of the short charged-

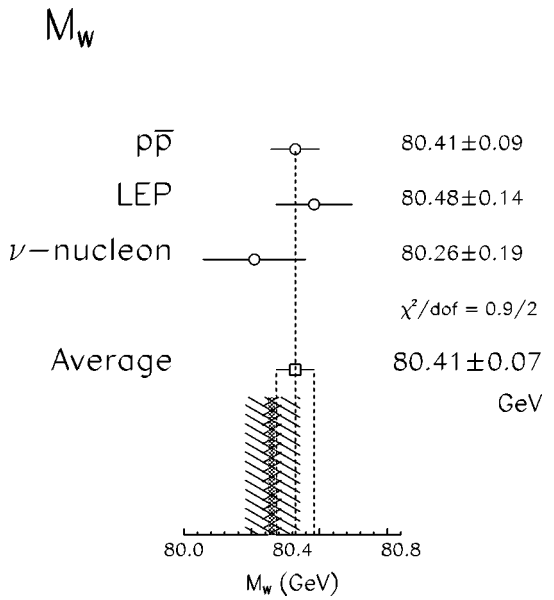

FIG. 39. Recent determinations of the W mass compared with the expectation of the standard model. The hatching code of the MSM prediction is described in Fig. 3.

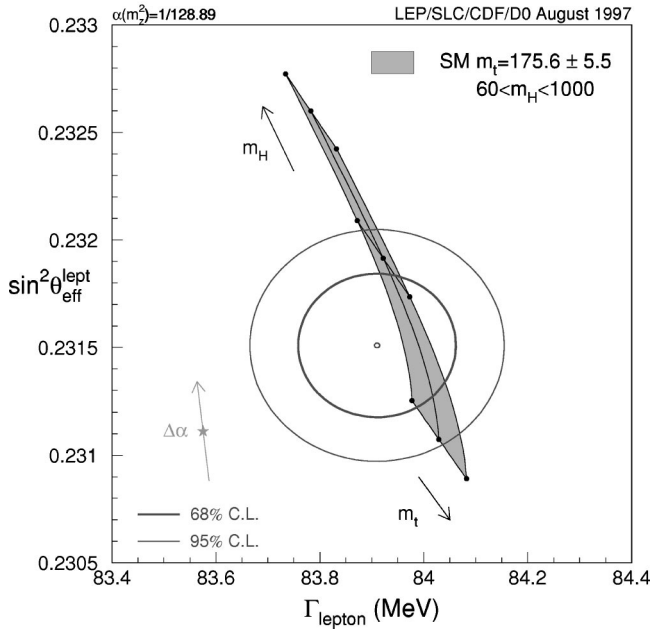

FIG. 40. The 68%- and 95%-confidence level contours of Γ_ℓ vs $\sin^2\theta^\ell_{\rm eff}$ compared with the MSM predictions. The star shows the ''Born'' prediction (only the running of α is included) and the arrow shows the effect of its present uncertainty.

current events that are misclassified. The largest source of contamination in the short-event sample comes from events in which the outgoing muon does not cross the required number of counters and from events induced by the the small fraction of electron neutrinos present in the beam. The CCFR experiment (CCFR, 1996) measures $s^2_W=1-(M_W/M_Z)^2$ with a statistical error of 0.0025. The main contribution to the experimental error (0.0038) comes from limited knowledge of the electron neutrino flux, while the theoretical error (0.0039) is dominated by uncertainties in the charm production.

The present world average is essentially a combination of the measurements done by CDHS (1986), CHARM (1987), and CCFR (1996):

$$s^2_W=1-(M_W/M_Z)^2=0.2254\pm0.0037$$

or, equivalently, a value of $M_W=80.26\pm0.19$ GeV. This indirect measurement of the W mass is compared to the other measurements in Fig. 39 together with the standard-model prediction.

VI. STANDARD-MODEL TESTS

Precise measurements of many electroweak observables performed at LEP and SLC have been presented in the previous sections. The first part of this section analyzes these data within the framework of the minimal standard model. Then possible models beyond the MSM are studied. In particular, the epsilon variables introduced by Altarelli *et al.* (1992, 1993a, 1993b) are used to obtain constraints on new physics arising from the minimal supersymmetric standard model or technicolor. Finally, limits on extra neutral bosons are discussed in Sec. VI.C.

A. Standard-model fits

The measurements of the electroweak observables discussed in this report are analyzed within the framework of the minimal standard model to verify whether the data are able to discriminate the nontrivial MSM radiative corrections introduced in Sec. I.B. In a first stage the test is restricted to the subset of measurements specifically sensitive to the different electroweak radiative corrections discussed in Sec. I.D: Γ_ℓ, $\sin^2\theta^\ell_{\rm eff}$, M_W, and R_b, which are, respectively, directly sensitive to $\Delta\rho$, $\Delta\kappa$, Δr, and the $Z\to b\bar{b}$ vertex correction.

Figure 40 compares the probability contours from the measurements of Γ_ℓ and $\sin^2\theta^\ell_{\rm eff}$ with the MSM prediction. This plot contains almost all the information on radiative corrections obtained from Z line-shape and asymmetry measurements. The measurements are not consistent with the ''Born'' prediction—in which the only radiative correction included is the running of the electromagnetic coupling constant—while they are consistent with the MSM prediction for light Higgs masses, with a confidence level better than 68%.

The effect of nontrivial electroweak corrections is even more apparent in Fig. 41, showing probability contours from the measurements of M_W and $\sin^2\theta^\ell_{\rm eff}$. The measurements are again inconsistent with the ''Born'' prediction and consistent with the MSM prediction. Figure 42 shows the intersections among the one-standard-deviation bands (68% C.L.) for R_b, $\sin^2\theta^\ell_{\rm eff}$ and R_ℓ measurements, the latter mixing both dependences. The consistency of the intersections provides a rather model-independent check of the direct and indirect determinations of R_b. The intersection region is in good agreement with the MSM predictions.

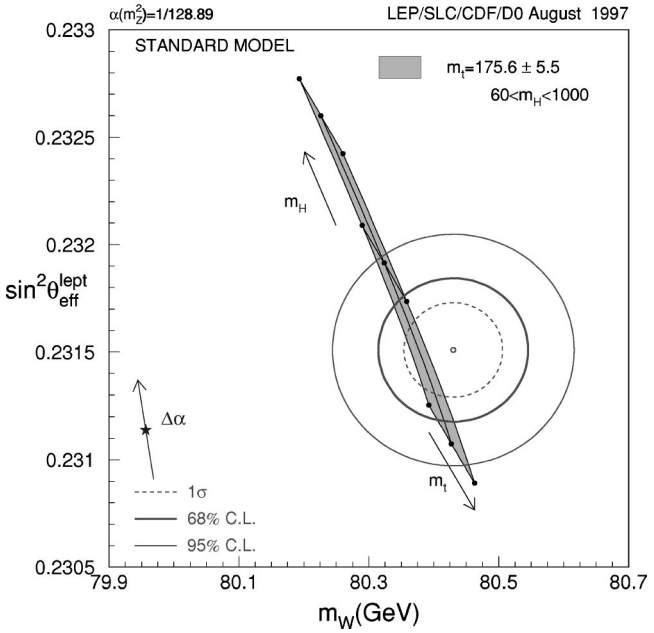

FIG. 41. Contours at 39%, 68%, and 95% confidence levels of M_W vs $\sin^2\theta_{\rm eff}$ compared with the predictions of the minimal standard model. The star shows the "Born" prediction (only the running of α is included), and the arrow shows the effect of its present uncertainty.

The previous plots show that the measurements are sufficiently precise to discriminate the nontrivial radiative corrections. It is now important to verify that measurements sensitive to different radiative corrections show consistency with the predictions when these corrections are computed within the MSM with a given set of values for its input parameters.

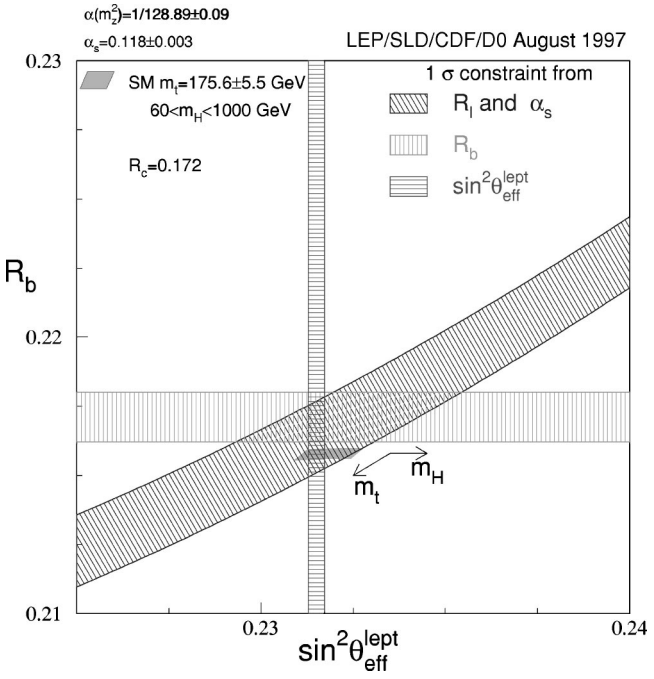

FIG. 42. One-standard-deviation bands of the R_b, $\sin^2\theta_{\rm eff}$, and R_ℓ measurements compared with MSM predictions.

This analysis is done with a χ^2 fit of the measurements to their MSM predictions using the complete set of electroweak observables discussed in this review. In the fit it is assumed that the systematic errors—prevailing over the statistical ones for some of the relevant measurements—have a Gaussian behavior. The set of data used in the fit is summarized in Table IX. The two values for R_b and the two values for R_c are combined before the fit, to take into account the correlations between their systematic errors, resulting in 21 input measurements, including $\alpha(M_Z^2)$, α_s, and m_t. The χ^2 is minimized by recomputing the MSM predictions of the 21 input observables with different values of the MSM parameters. G_F is not varied, since it is known with high precision, while the Z mass—known with similar precision—is varied to take into account the small correlation with some of the input data. All the other MSM parameters are varied. Table IX shows the result of the fit and the statistical significance—in standard deviations—of the difference between the measured values and their MSM predictions. No significant discrepancy is observed.

The χ^2 of the fit is 18 for 16 degrees of freedom, which corresponds to a confidence level of 30%. It is worth noting that the numerical value of the $\chi^2/N_{\rm DF}$ depends on the choice of dataset used in the fit. This choice is unbiased but also arbitrary, since the actual set of individual direct measurements is much larger, and some of them have been combined with *a priori* assumptions into the quantities used in the fit. In the combination process, the information on the internal consistency among the combined measurements is lost, and therefore some relevant statistical information is missing. As an example, the largest pulls in Table IX come from the SLD $A_{\rm LR}$ determination of $\sin^2\theta_{\rm eff}$ and from the forward-backward b asymmetry. If these measurements were combined before the fit, together with the other asymmetries, the resulting $\chi^2/N_{\rm DF}$ of the fit would be smaller (see discussion in Sec. IV.F). Conversely, combining the two values of the W mass before the fit results in an increase of the $\chi^2/N_{\rm DF}$.

The fit has been repeated, excluding from the input values $\alpha(M_Z^2)$, α_s, and m_t in turn. In this study the Higgs mass is fixed at 300 GeV. The results are given in Table X. When $\alpha(M_Z^2)$ is left unconstrained, the data predict $\alpha^{-1}(M_Z^2)=129.10\pm0.11^{+0.25}_{-0.32}$, in good agreement with the actual measurement of $\alpha^{-1}(M_Z^2)=128.896\pm0.090$, with slightly larger uncertainty and a large variation when the Higgs mass is moved from 70 GeV to 1 TeV. This is because the maximal sensitivity to $\Delta\alpha$ comes from the measurement of $\sin^2\theta_{\rm eff}$, which is also very sensitive to M_H (see Table I in Sec. I.C).

When α_s is left free, the data predict $\alpha_s=0.1211\pm0.0030^{+0.0026}_{-0.0019}$, in good agreement with the world average $\alpha_s=0.118\pm0.003$ and with the same accuracy for a fixed value of the Higgs mass. The influence of the Higgs mass is, in this case, quite small because the main sensitivity to α_s comes from R_ℓ, which is almost insensitive to non-QCD radiative corrections, as discussed in Sec.

TABLE IX. Summary of the measurements included in the combined analysis of standard-model parameters. Section (a) summarizes LEP averages, Section (b) summarizes the relevant SLC results, and Section (c) the electroweak results from hadron colliders and νN scattering. The estimated systematic error component of the quoted uncertainty is indicated in parenthes. The MSM fit result in column 3 and the pulls in column 4 are derived from the fit including all data with the Higgs mass as a free parameter ($M_H = 109$ GeV).

	Measurement	Correlation matrix	Standard-model fit	Pull
$\alpha(M_Z^2)^{-1}$	$128.896 \pm 0.090(83)$		128.909	−0.2
$\alpha_s(M_Z^2)$	$0.118 \pm 0.003(3)$		0.119	−0.3
(a) LEP				
Line-shape and lepton asymmetry:				
M_Z [GeV]	$91.1867 \pm 0.0020(15)$		91.1866	0.0
Γ_Z [GeV]	$2.4948 \pm 0.0025(15)$	0.05	2.4962	−0.6
σ_h^o [nb]	$41.486 \pm 0.053(52)$	−0.01 −0.16	41.471	0.3
R_ℓ	$20.775 \pm 0.027(24)$	−0.02 0.00 0.14	20.751	0.9
$A_{\rm FB}^o(\ell)$	$0.0171 \pm 0.0010(7)$	0.06 0.00 0.00 0.01	0.0163	0.9
τ polarization:				
$\mathcal{A}_\tau$	$0.1411 \pm 0.0064(40)$		0.1472	−1.0
$\mathcal{A}_e$	$0.1399 \pm 0.0073(20)$		0.1472	−1.0
b and c quark:				
R_b	$0.2174 \pm 0.0009(7)$		0.2158	1.8
R_c	$0.1727 \pm 0.0050(38)$	−0.22	0.1723	−0.1
$A_{\rm FB}^0(b)$	$0.0983 \pm 0.0024(10)$	−0.03 0.03	0.1032	−2.0
$A_{\rm FB}^0(c)$	$0.0739 \pm 0.0048(25)$	0.02 −0.08 0.13	0.0737	0.0
$q\bar{q}$ charge asymmetry:				
$\sin^2\theta_{\rm eff}^\ell(Q_{\rm FB})$	$0.2322 \pm 0.0010(8)$		0.23150	0.7
M_W [GeV]	$80.48 \pm 0.14(5)$		80.377	0.7
(b) SLD				
$\sin^2\theta_{\rm eff}^\ell(A_{\rm LR}^o)$	$0.23055 \pm 0.00041(14)$		0.23150	−2.3
R_b	$0.2124 \pm 0.0029(17)$		0.2158	−1.1
R_c	$0.1810 \pm 0.0145(79)$		0.1723	0.6
$\mathcal{A}_b$	$0.900 \pm 0.050(31)$		0.935	−0.7
$\mathcal{A}_c$	$0.650 \pm 0.058(29)$		0.668	−0.3
(c) $p\bar{p}$ and νN				
M_W [GeV] $(p\bar{p})$	$80.41 \pm 0.09(07)$		80.377	0.4
$1 - M_W^2/M_Z^2(\nu N)$	$0.2254 \pm 0.0037(23)$		0.2230	0.6
m_t [GeV] $(p\bar{p})$	$175.6 \pm 5.5(4.2)$		172.9	0.5

I.D. The difference between the value of α_s obtained from this fit and the value quoted in Sec. II.D.3, where α_s was derived from R_ℓ alone, comes from the additional sensitivity of Γ_Z and σ_h^o to α_s.

When m_t is left unconstrained the data predict $m_t = 181.3^{+6.1+15.7}_{-6.2-17.3}$ GeV, in perfect agreement with the Tevatron measurement $m_t = 175.6 \pm 5.5$ GeV. For a fixed value of the Higgs mass the uncertainty in the fitted value is similar to that of the direct measurement. The large variation of the central value when M_H is changed reflects the large correlation between the contributions of m_t and M_H to radiative corrections already discussed in Sec. I.D.

The results of the fits when only M_H is left free are shown in Table XI. The data predict $M_H = 109^{+108}_{-60}$ GeV. This value is in agreement with the

TABLE X. Results of fits to the data set of Table IX for fixed M_H values. The central values and the first errors refer to $M_H = 300$ GeV. The second errors correspond to the variation of the central value when varying M_H from 70 GeV (lower number) to 1 TeV (upper number).

Free →	$\alpha^{-1}(M_Z^2)$	α_s	m_t
$\alpha^{-1}(M_Z^2)$	$129.10 \pm 0.11^{+0.25}_{-0.32}$	$128.97 \pm 0.07^{+0.10}_{-0.12}$	$128.95 \pm 0.08^{+0.03}_{-0.05}$
α_s	$0.1193 \pm 0.0021^{+0.0010}_{-0.0005}$	$0.1211 \pm 0.0030^{+0.0026}_{-0.0019}$	$0.1195 \pm 0.0021^{+0.0011}_{-0.0007}$
m_t (GeV)	$174.7 \pm 4.8^{+2.8}_{-2.3}$	$178.0 \pm 4.2^{+6.9}_{-7.4}$	$181.3^{+6.1+15.7}_{-6.2-17.3}$

TABLE XI. Results of fits to the data set of Table IX with the Higgs mass left free (column 2) and all listed parameters left free (column 3).

Free →	M_H	all
$\alpha^{-1}(M_Z^2)$	128.91 ± 0.09	$128.75^{+0.35}_{-0.27}$
$\alpha_s(M_Z^2)$	0.1188 ± 0.0022	$0.1204^{+0.0038}_{-0.0034}$
m_t (GeV)	172.9 ± 5.3	165^{+12}_{-11}
M_H (GeV)	109^{+108}_{-60}	25^{+143}_{-16}
$\chi^2/(N_{\mathrm{DF}})$	18/16	16/13

negative result of the searches at LEP, which bounds M_H from below at about 77 GeV (Janot, 1997), and with the validity range of our perturbative calculations (Cabibbo *et al.*, 1979; Lindner, 1986; Luscher and Weisz, 1988; Sher, 1989; Altarelli and Isidori, 1994; Casas *et al.*, 1995), which bound M_H from above at about 1 TeV. This result is the best estimate of M_H now possible, since it uses all the relevant data available. The dependence of the radiative corrections on M_H is logarithmic, and the result of the fit is more correctly expressed as $\log_{10}(M_H/1\,\mathrm{GeV}) = 2.04^{+0.30}_{-0.35}$.

Figure 43 shows the χ^2 variation of this fit as a function of the Higgs mass and the effect of uncertainties in the calculations used for the predictions, already discussed in Sec. I.C. A 95-%-confidence-level upper limit $M_H < 420\,\mathrm{GeV}$ can be derived from this fit, using the most pessimistic assumption for the theoretical error on the calculations and neglecting the information contained in the lower limit from direct searches. Recent calculations of higher-order contributions for some of the main observables (Degrassi *et al.*, 1997b) may reduce the theoretical uncertainty, thus possibly reducing the upper limit on the Higgs mass computed with this technique to about $M_H < 295\,\mathrm{GeV}$.

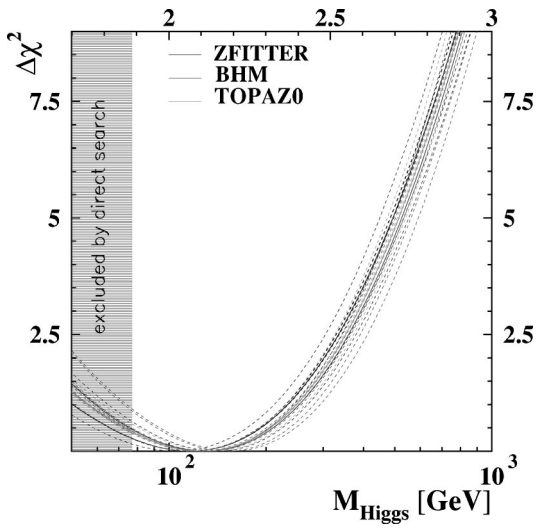

FIG. 43. Variation of the χ^2 of the fit vs Higgs mass using all precision data. Different lines correspond to results obtained using electroweak libraries with different options in the calculations (Burgers *et al.*, 1990; Bardin *et al.*, 1992; Montagna *et al.*, 1993).

A word of caution on the determination of the upper limit on the Higgs mass: since the measurements are sensitive to $\log M_H$, small fluctuations in the position of the minimum generate significant changes in M_H and in its error, resulting in large variations of the upper limit. Moreover a proper evaluation of the upper limit should include the information contained in the direct limit from searches at LEP2. The main conclusion from Fig. 43 is that the electroweak fit prefers a light Higgs mass in a range consistent with the negative searches performed at LEP2.

The last column of Table XI shows the result of the fit when the MSM input parameters mentioned above are simultaneously unconstrained. Even in this case the data are precise enough to predict values for these parameters. They are in good agreement with direct measurements and theoretical expectations.

B. Tests of new physics using the ε's variables

As already discussed in Sec. I.D, there are four nontrivial and numerically relevant loop corrections contributing beyond tree level to predictions of the observables presented in this report. They are the three vacuum polarization corrections Δr, $\Delta\kappa$, and $\Delta\rho$ and the $Z \to b\bar{b}$ vertex correction. In the MSM they have a similar leading dependence, as shown by Eq. (20).

In other models, due to the contributions of still undiscovered heavy particles, the vacuum polarization terms Π^W, $\Pi^{\gamma Z}$, and Π^Z could be different. It is interesting to analyze the precise electroweak measurements to extract the loop contributions as if they were independent. Several possibilities have been suggested (Kennedy and Langacker, 1990; Peskin and Takeuchi, 1990; Novikov *et al.*, 1993), among which the most popular are the ε parameters (Altarelli *et al.*, 1995). The ε parameters are a set of four variables, defined in terms of measured electroweak observables, which quantify the deviations of these observables with respect to the Born prediction plus QED and QCD effects, which we shall call the "Born" expectation below.

The defining observables are M_W, $A_{\mathrm{FB}}^0(\ell)$, Γ_ℓ, and Γ_b, which are related to the loop corrections introduced in Sec. I.B as follows:

$$\frac{M_W}{M_Z} \to \Delta r_W \equiv \Delta r - \Delta\alpha,$$

$$A_{\mathrm{FB}}^0(\ell) \to \sin^2\theta_{\mathrm{eff}}^{\ell} = s_0^2(1 - \Delta\kappa'),$$

$$\Gamma_\ell \to g_{A_l} = -\frac{1}{2}\left(1 + \frac{\Delta\rho_l}{2}\right),$$

$$\Gamma_b \to g_{A_b} = -\frac{1}{2}\left(1 + \frac{\Delta\rho_l}{2}\right)(1 + \varepsilon_b),$$

$$\frac{g_{V_b}}{g_{A_b}} = \left(1 - \frac{3}{4}\sin^2\theta_{\mathrm{eff}}^{\ell} + \varepsilon_b\right) \Big/ (1 + \varepsilon_b),$$

where ε_b is the $Z\to b\bar{b}$ vertex correction introduced to modify only the left-handed b-quark coupling to the Z and not the right-handed one. The quantity s_0 is defined by

$$s_0^2 c_0^2 = \frac{\pi\alpha(M_Z)}{\sqrt{2}G_F M_Z}, \tag{59}$$

with $c_0^2 = 1 - s_0^2$. This definition of the sine is similar to that in the tree-level Eq. (1), but includes the running of α to $q^2 = M_Z^2$.

The quantities Δr_W, $\Delta\rho_l$, $\Delta\kappa'$, and ε_b measure deviations from the "Born" expectations of the defining observables. The ε variables are defined by linear combinations of these deviations:

$$\begin{aligned}
\varepsilon_1 &= \Delta\rho_l, \\
\varepsilon_2 &= c_0^2\Delta\rho_l + \frac{s_0^2}{c_0^2 - s_0^2}\Delta r_W - 2s_0^2\Delta\kappa', \\
\varepsilon_3 &= c_0^2\Delta\rho_l + (c_0^2 - s_0^2)\Delta\kappa'.
\end{aligned} \tag{60}$$

In the MSM the leading contributions to the ε variables are

$$\begin{aligned}
\varepsilon_1 &= \frac{3G_F}{8\pi^2\sqrt{2}}m_t^2 - \frac{3G_F M_W^2}{4\pi^2\sqrt{2}}\frac{s_W^2}{c_W^2}\ln\frac{M_H}{M_Z} + \cdots, \\
\varepsilon_2 &= -\frac{G_F M_W^2}{2\pi^2\sqrt{2}}\ln\frac{m_t}{M_Z} + \cdots, \\
\varepsilon_3 &= \frac{G_F M_W^2}{12\pi^2\sqrt{2}}\ln\frac{M_H}{M_Z} + \cdots, \\
\varepsilon_b &= -\frac{G_F}{4\pi^2\sqrt{2}}m_t^2 + \cdots.
\end{aligned} \tag{61}$$

Here ε_1 has the dominant m_t and M_H dependences, ε_2 contains the logarithmic m_t dependence, ε_3 is mainly sensitive to $\ln(M_H/M_Z)$—but about three times less sensitive than ε_1—and ε_b has a quadratic sensitivity to m_t from the $Z\to b\bar{b}$ vertex correction. The variables ε_2 and ε_3 do not have contributions of the order $G_F m_t^2$ and hence are more sensitive to possible contributions from new physics.

The analysis in terms of the ε variables can be extended with some dynamical assumptions to other electroweak observables. In particular, the observables discussed in this review can be included in the analysis with the assumption that all deviations from the MSM are only contained in the vacuum polarization diagrams and in the $Z\to b\bar{b}$ vertex (Altarelli *et al.*, 1995). A subset of the data shown in Table IX is analyzed in terms of the ε variables using the formulas of reference (Altarelli *et al.*, 1995) and propagating the present uncertainties in $\alpha(M_Z^2)$ and in $\alpha_s(M_Z^2)$ in the fit. The result is

$$\begin{aligned}
\varepsilon_1 &= (4.1\pm 1.2)\times 10^{-3}, \\
\varepsilon_2 &= (-9.5\pm 2.1)\times 10^{-3}, \\
\varepsilon_3 &= (3.9\pm 1.1)\times 10^{-3}, \\
\varepsilon_b &= (-3.5\pm 1.9)\times 10^{-3},
\end{aligned}$$

in good agreement with the standard-model expectations.

Figure 44 shows the results for ε_1, ε_3, and ε_b, which are the variables mainly constrained by LEP and SLD measurements. These results are compared in Fig. 45 with ε_2 that is linked to the W mass measurement. In these plots the 39%-C.L. contours obtained from measurements of the ε variables are shown together with the MSM predictions for different values of m_t and M_H. The "Born" prediction corresponds to $\varepsilon_i = 0$ and is not compatible with the results of the fit, which are consistent with the direct measurement of the top mass and prefer a light Higgs mass.

1. Implications for the minimal supersymmetric standard model

The minimal supersymmetric standard model (MSSM) (Nilles, 1984; Haber and Kane, 1985; Barbieri, 1988) is a natural extension of the MSM with solid motivations. It is a complete and consistent model and can be used to predict all the observables discussed in the present report. However, it has a large number of free parameters, which make fitting the data in the most general case very difficult. Following (Altarelli, 1997; see also Altarelli *et al.*, 1993b), we consider two limiting scenarios:

(i) The "*heavy MSSM*," in which all supersymmetric particles (s particles or sparticles) are rather massive. In this case the MSSM predictions for the radiative corrections reproduce the MSM results with a light Higgs particle ($M_H \leqslant 100\,\mathrm{GeV}$); (Barbieri *et al.*, 1992).

(ii) The "*light MSSM*," in which some of the sparticles have a mass close to their present experimental lower bounds. In this case, the pattern of radiative corrections may deviate sizably from that of the MSM. The most relevant differences occur in vacuum polarizations and/or in the Zbb vertex. These effects can be described in terms of the ε variables obtained from the fit described in the previous section.

Since the data interpreted in the MSM prefer a light Higgs particle, they are also compatible with the heavy MSSM scenario. This case is illustrated in Fig. 46. In this figure the width of the band of the MSSM prediction is due to the MSSM Higgs sector and corresponds to the region covered by the allowed values for the masses of the Higgs bosons.

Several effects in the ε variables are predicted (Alvarez-Gaumé *et al.*, 1983; Barbieri and Maiani, 1983; Hollik, 1990b; Boulware and Finnel, 1991; Garcia and Solà, 1995; Altarelli, 1997) in the light MSSM scenario. The good agreement of the ε variables with their MSM expectations gives little room for the expected deviations, and limits on the MSSM parameters can be obtained. However, in most cases large deviations from the

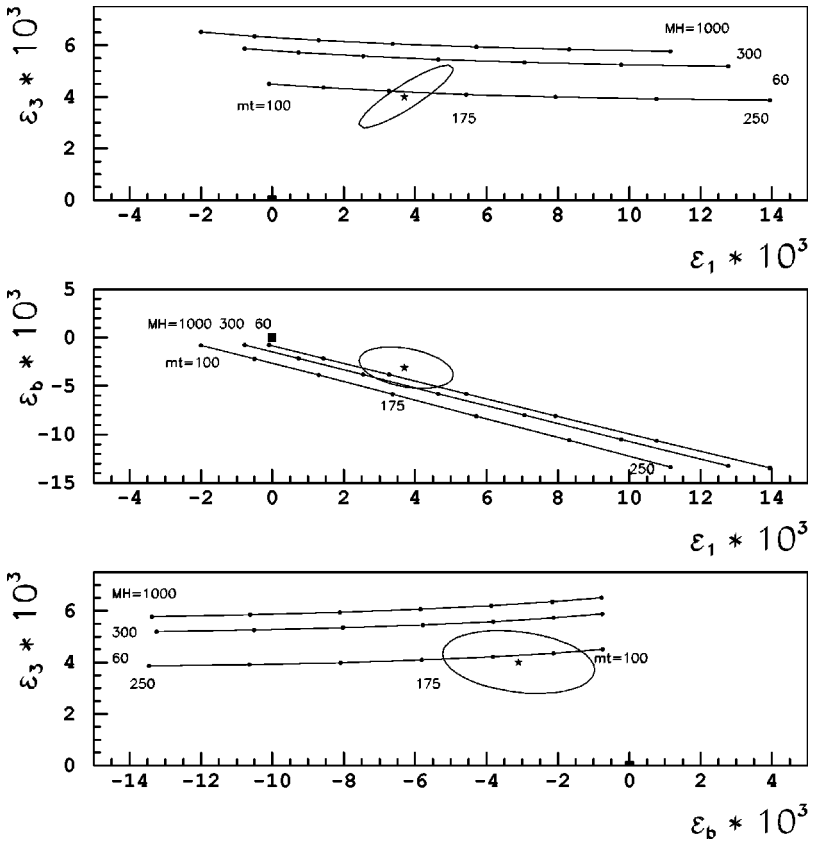

FIG. 44. The 39% C.L. contours of the ε variables compared with the predictions of the minimal standard model as a function of m_t and M_H. The "Born" expectation ($\varepsilon_i=0$) is indicated by a solid square.

MSM prediction correspond to regions of the MSSM parameters already excluded by direct searches, and no further constraint can be derived.

2. Implications for technicolor

Most technicolor models (Weinberg, 1976; Farhi and Susskind, 1981) produce large and positive corrections to ε_3 (Ellis *et al.*, 1995). The experimental values of ε_1 and ε_3 are small enough to rule out a substantial class of simple technicolor models (Ellis *et al.*, 1995), as is shown in Fig. 46.

The fitted value of ε_b also disfavors a wide class of such models: in extended technicolor models the same mechanism that generates the large top-quark mass also leads to large corrections to the $Z\rightarrow b\bar{b}$ vertex (Chivukula *et al.*, 1992). These imply large, negative corrections to ε_b that are not observed.

C. Limits on extra neutral bosons

In most grand unified theories the gauge group is such that, after the breaking of the GUT symmetry, it gives rise to one or more extra U(1) groups (Ross, 1987). If one of these groups, or a combination of them, would remain unbroken at relatively low energies (a few TeV), the effect of the extra neutral gauge boson, called Z', could be seen at LEP (Hewett and Rizzo, 1989).

Extra Z bosons have three effects on LEP observables:

(i) The exchange of a virtual Z' in the s channel modifies cross sections and asymmetries for all pairs of fermions. However, since around the Z pole the interference between the almost purely imaginary Z-mediated amplitude and the almost purely real Z'-mediated amplitude is very small, the effect of the Z' amplitude squared is very small for Z' masses above the direct limits set by CDF (1997c) and DØ (1996).

(ii) If the new neutral gauge boson and the Z boson mix, then the low-mass eigenstate (the one seen at LEP1) does not coincide with the standard-model Z boson. The measured mass is shifted by a small amount—below 1 MeV—for Z' masses above the Tevatron limits.

(iii) In the case of Z-Z', mixing, the couplings of the low-mass eigenstate to fermions contain an admixture of the Z' coupling to fermions. Since the couplings of the Z to fermions have been very precisely measured at LEP and SLD, the Z-Z' mixing can be severely constrained.

Several experiments have studied putting limits on the Z-Z' mixing and Z' mass (L3, 1993c; ALEPH, 1994f). The program of reference (Riemann, 1993) is generally used to compute the predictions for the electroweak observables discussed in this report when including the ef-

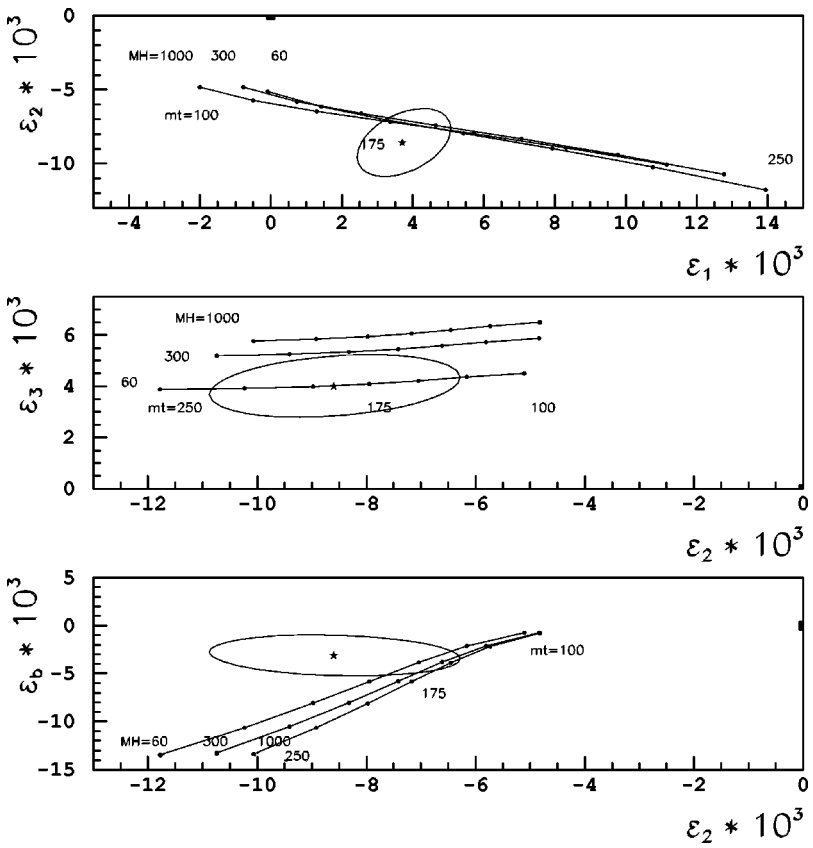

FIG. 45. The 39% C.L. contours of the ε variables compared with the predictions of the minimal standard model as a function of m_t and M_H. The "Born" expectation ($\varepsilon_i=0$) is indicated by a solid square.

fect of an extra Z boson from E_6 models or left-right symmetric models (Ross, 1987). A fit to all data is performed, leaving free the Z-Z' mixing angle, the Z mass, the top mass, and α_s, although the last three quantities are constrained to their measured values. The Z' mass and the Higgs mass are fixed. With this method, and using the data presented here, mixing angles larger than about 2–5 mrad can be excluded at the 95% confidence level for most Z' models. If the Z' mass is left free in the fit, one observes that the sensitivity to its value is rather poor.

Some experiments have used Z peak events with photons radiated in the initial state to probe the regions with effective center-of-mass energy, $\sqrt{s'}$, well below the Z mass (DELPHI, 1995f; L3, 1996; ALEPH, 1997c). In this case, the interference between photon-mediated, Z-mediated, and Z'-mediated amplitudes can be sizable and therefore one has a handle on the Z' mass. Unfortunately, most of the sensitivity comes from events with hard initial-state radiation, of which there are not many. The exclusion limits on $M_{Z'}$ that can be obtained are not competitive with the direct limits obtained at the Tevatron.

D. Conclusions and outlook

The measurements performed at LEP and SLC by the collaborations ALEPH, DELPHI, L3, OPAL, and SLD have substantially improved the precision of the test of the standard model. The Z mass is measured with an accuracy of 2 parts in 10^5 and all the other relevant electroweak observables are measured with a typical precision of about 1 part in 10^3.

These measurements are compared with predictions based on the standard model of the electroweak interactions, showing a good overall agreement. At this level of precision the effects of the nontrivial loop contributions are visible with a significance larger than three standard deviations. The top mass predicted by the electroweak fit of LEP and SLC data is 181 ± 18 GeV, in very good agreement with the direct measurement 175 ± 6 GeV by the CDF and DO Collaborations.

The mass of the Higgs boson is predicted including the measured value of the top mass in the fit. The prediction $M_H=109^{+108}_{-60}$ GeV has large asymmetric errors, reflecting the intrinsic logarithmic dependence of the electroweak radiative corrections on the mass of the Higgs boson. This result translates into an upper limit of 420 GeV on the Higgs mass at 95% confidence level.

Few improvements are expected from the final analyses of the present LEP data set. The prolongation of the run of SLD up to 0.5 million Z decays would reduce the error on $A_{\rm LR}$ by a factor of 1.5 and consequently the error on the $\sin^2\theta^{\ell}_{\rm eff}$ by about 20%. With 500 pb^{-1} per experiment above the threshold for production of W pairs, LEP2 will measure the W mass with a precision of

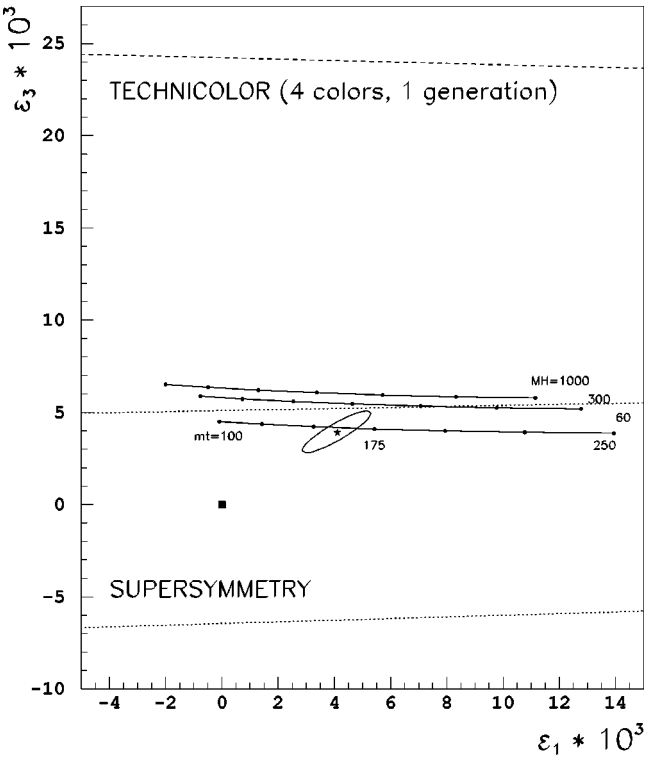

FIG. 46. The one-sigma (39% C.L.) contour in the ε_1 vs ε_3 plane. The "Born" expectation $\varepsilon_i=0$ is indicated by a solid square. The solid lines are the predictions of the minimal standard model for different values of m_t and M_H. The band between the dotted lines is the expectation for a "heavy MSSM." The dashed line corresponds to the expectation for a simple technicolor model (Ellis *et al.*, 1995).

30 MeV. Combining this result with the final value of M_W from run 1 of the Tevatron will reduce the present error on M_W by about a factor of three. In addition the final analysis of the top mass could reduce the error to about 4 GeV. With this improved precision the error on the prediction of $\log_{10}(M_H/1\,\mathrm{GeV})$ is reduced from 0.3 to about 0.2.

If LEP2 does not discover the Higgs boson, no other important improvements in the precision of the test of the standard model are expected before the new century. Then the new high-luminosity run of the Tevatron and eventually LHC will produce a new set of data that will put the standard model to more stringent tests.

ACKNOWLEDGMENTS

The results presented in this report are the outcome of many years of work by LEP and SLC physicists. We are indebted to many ALEPH, DELPHI, L3, OPAL, and SLD colleagues for all we have learned from them during this time. In particular we should like to thank the members of the ALEPH Electroweak Group, of the LEP Electroweak Working Group, and of the LEP Energy Calibration Working Group.

We have referenced as much as we could other people's work and we apologize if we forgot anybody. We are grateful to Duccio Abbaneo, Alain Blondel, Tiziano Camporesi, David Charlton, Robert Clare, Fabiola Gianotti, Su Dong, Patrick Janot, Klaus Moenig, Sasha Olshevsky, Fabrizio Palla, Monica Pepe-Altarelli, Dieter Schlatter, and Frederic Teubert for providing plots, for giving suggestions about the paper, and for their constructive criticisms.

Finally we should like to thank Paola Catapano for reading the manuscript and Valerie Brunner for her help with the references.

APPENDIX: CROSS SECTIONS AND FORMULAE

The differential cross section for $f\bar{f}$ production, colliding unpolarized e^+ with polarized e^- with longitudinal polarization P_e, can be computed in terms of the effective couplings using the amplitudes introduced in Section I.B in Eqs. (3) and (9).

Neglecting the masses of the fermions, producing effects of $\mathcal{O}(m_f^2/s)$, we can write the differential cross section for the production of a fermion f with helicity λ ($\lambda=\pm1$) at an angle θ with respect to the direction of the incoming e^- in the following way:

$$\begin{aligned}\frac{d\sigma}{d\cos\theta}(s,\cos\theta,\lambda;P_e) &= \frac{\pi\alpha^2(s)}{4s}N_c^f\{[(1+\cos^2\theta)G_1(s)+2\cos\theta G_2(s)] \\ &\quad -\lambda[(1+\cos^2\theta)G_4(s)+2\cos\theta G_3(s)] \\ &\quad -P_e([(1+\cos^2\theta)G_3(s)+2\cos\theta G_4(s)] \\ &\quad -\lambda[(1+\cos^2\theta)G_2(s)+2\cos\theta G_1(s)])\} \qquad \text{(A1)}\end{aligned}$$

where N_c^f is the color factor ($N_c^f=1$ for leptons and $N_c^f=3(1+\alpha_s/\pi)$ for quarks) and

$$\begin{aligned}G_1(s) &= Q_e^2Q_f^2+2Q_eQ_fg_{Ve}g_{Vf}\chi_{\gamma Z}(s) \\ &\quad +(g_{Ve}^2+g_{Ae}^2)(g_{Vf}^2+g_{Af}^2)\chi_{ZZ}(s), \\ G_2(s) &= 2Q_eQ_fg_{Ae}g_{Af}\chi_{\gamma Z}(s) \\ &\quad +4g_{Ve}g_{Ae}g_{Vf}g_{Af}\chi_{ZZ}(s), \\ G_3(s) &= 2Q_eQ_fg_{Ae}g_{Vf}\chi_{\gamma Z}(s) \\ &\quad +2g_{Ve}g_{Ae}(g_{Vf}^2+g_{Af}^2)\chi_{ZZ}(s), \\ G_4(s) &= 2Q_eQ_fg_{Ve}g_{Af}\chi_{\gamma Z}(s) \\ &\quad +2(g_{Ve}^2+g_{Ae}^2)g_{Vf}g_{Af}\chi_{ZZ}(s).\end{aligned}$$

The couplings g_{Vf} and g_{Af} are defined in Eq. (10) and

$$\chi_{\gamma Z}(s)=F_G(s)\frac{s(s-M_Z^2)+s^2\Gamma_Z/M_Z\,\mathrm{Im}(\Delta\alpha)}{(s-M_Z^2)^2+s^2\Gamma_Z^2/M_Z^2},$$

$$\chi_{ZZ}(s)=F_G^2(s)\frac{s^2}{(s-M_Z^2)^2+s^2\Gamma_Z^2/M_Z^2},$$

$$F_G(s)=\frac{G_FM_Z^2}{2\sqrt{2}\pi\alpha(s)}.$$

The coefficient F_G at the Z pole is $F_G(M_Z^2)\simeq 1.407$.

The total cross section, summing on the two possible helicities of the outgoing fermion, is

$$\sigma(s)=\frac{4\pi\alpha^2(s)}{3s}N_c^f[G_1(s)-P_eG_3(s)]. \tag{A2}$$

In Eqs. (A1) and (A2) the electron polarization is defined as $P_e=+1$ for 100% right-ended electron polarization and $P_e=-1$ for 100% left-ended electron polarization. The symbol $\mathcal{P}$ used in Eqs. (41) and (42) represents the average magnitude of the beam polarization, which is by definition a positive quantity. The asymmetries defined in the Eqs. (38) to (42) can be computed using the differential cross section (A1):

$$A_{\rm pol}(s)=-\frac{G_4(s)}{G_1(s)},$$

$$A_{\rm pol}^{\rm FB}(s)=-\frac{3}{4}\frac{G_3(s)}{G_1(s)},$$

$$A_{\rm FB}(s)=\frac{3}{4}\frac{G_2(s)}{G_1(s)},$$

$$A_{\rm LR}(s)=\frac{G_3(s)}{G_1(s)},$$

$$A_{\rm FB}^{\rm pol}(s)=\frac{3}{4}\frac{G_4(s)}{G_1(s)}.$$

The energy dependence of the ratios G_i/G_1 near the Z pole is given by

$$\frac{G_2(s)}{G_1(s)}=\mathcal{A}_e\mathcal{A}_f+S_2^f\frac{1}{F_G(M_Z^2)}\left[\frac{(s-M_Z^2)}{s}+\frac{\Gamma_Z}{M_Z}\mathrm{Im}(\Delta\alpha)\right],$$

$$\frac{G_3(s)}{G_1(s)}=\mathcal{A}_e+S_3^f\frac{1}{F_G(M_Z^2)}\left[\frac{(s-M_Z^2)}{s}+\frac{\Gamma_Z}{M_Z}\mathrm{Im}(\Delta\alpha)\right],$$

$$\frac{G_4(s)}{G_1(s)}=\mathcal{A}_f+S_4^f\frac{1}{F_G(M_Z^2)}\left[\frac{(s-M_Z^2)}{s}+\frac{\Gamma_Z}{M_Z}\mathrm{Im}(\Delta\alpha)\right], \tag{A3}$$

where the asymmetries $\mathcal{A}_f$ are defined by Eq. (37) and the coefficients S_i^f are

$$S_2^f=\frac{2Q_eQ_f}{(g_{Ve}^2+g_{Ae}^2)(g_{Vf}^2+g_{Af}^2)}(g_{Ae}g_{Af}-g_{Ve}g_{Vf}\mathcal{A}_e\mathcal{A}_f),$$

$$S_3^f=\frac{2Q_eQ_f}{(g_{Ve}^2+g_{Ae}^2)(g_{Vf}^2+g_{Af}^2)}g_{Ve}(g_{Af}-g_{Vf}\mathcal{A}_f),$$

$$S_4^f=\frac{2Q_eQ_f}{(g_{Ve}^2+g_{Ae}^2)(g_{Vf}^2+g_{Af}^2)}g_{Vf}(g_{Ae}-g_{Ve}\mathcal{A}_e). \tag{A4}$$

Table XII shows the numerical values of the effective couplings computed from Eq. (10) assuming $\rho^f=1$ and $\sin^2\theta_{\rm eff}^f=0.2316$ and also the numerical values of other functions of these couplings introduced in this Appendix. The energy dependence of the measured asymmetries and the correction due to the imaginary part of $\Delta\alpha$ can be computed using the numerical coefficients given in Table XII. The largest effect is for the forward-backward asymmetry of the leptons:

TABLE XII. Numerical values of the couplings and of their functions computed assuming $\rho^f=1$ and $\sin^2\theta_{\rm eff}^f=0.2316$.

f	g_{Vf}	g_{Af}	$\mathcal{A}_f$	S_2^f	S_3^f	S_4^f
e,μ,τ	-0.036	-0.5	0.143	7.92	0.56	0.56
u,c,t	$+0.191$	$+0.5$	0.667	4.62	1.75	0.24
d,s,b	-0.346	-0.5	0.935	1.78	1.22	0.04

$$A_{\rm FB}^{\ell}(s)=\frac{3}{4}\left[\mathcal{A}_e\mathcal{A}_\ell+S_2^\ell\frac{1}{F_G(M_Z^2)}\times\left(2\frac{\sqrt{s}-M_Z}{M_Z}+\frac{\Gamma_Z}{M_Z}\mathrm{Im}(\Delta\alpha)\right)\right]$$
$$=\frac{3}{4}\mathcal{A}_e\mathcal{A}_\ell+0.00009\Delta E(\mathrm{MeV})+0.002, \tag{A5}$$

where $\Delta E=\sqrt{s}-M_Z$. This is also the asymmetry measured with the smallest statistical error (0.001). For the other asymmetries the effect is smaller:

$$A_{\rm LR}^q(s)=\mathcal{A}_e+S_3^q\frac{1}{F_G(M_Z^2)}\left(2\frac{\sqrt{s}-M_Z}{M_Z}+\frac{\Gamma_Z}{M_Z}\mathrm{Im}(\Delta\alpha)\right)$$
$$=\mathcal{A}_e+0.00002\Delta E(\mathrm{MeV})+0.0005 \tag{A6}$$

and

$$A_{\rm pol}^\tau(s)=\mathcal{A}_e+S_4^\tau\frac{1}{F_G(M_Z^2)}\left(2\frac{\sqrt{s}-M_Z}{M_Z}+\frac{\Gamma_Z}{M_Z}\mathrm{Im}(\Delta\alpha)\right)$$
$$=\mathcal{A}_e+0.000009\Delta E(\mathrm{MeV})+0.0002. \tag{A7}$$

REFERENCES

Abbaneo, D., P. Antilogus, T. Behnke, S. Blyth, M. Elsing, R. Faccini, R. Jones, K. Mönig, S. Petzold, and R. Tenchini, 1997, "QCD corrections to the forward-backward asymmetries of c and b quarks at the Z pole," CERN-PPE/98-32.

ALEPH Collaboration, D. Decamp *et al.*, 1990, Nucl. Instrum. Methods Phys. Res. A **294**, 121.

ALEPH Collaboration, D. Decamp *et al.*, 1991a, Phys. Lett. B **259**, 377.

ALEPH Collaboration, D. Decamp *et al.*, 1991b, Phys. Lett. B **266**, 218.

ALEPH Collaboration, D. Buskulic *et al.*, 1992a, Phys. Lett. B **295**, 396.

ALEPH Collaboration, D, Decamp *et al.*, 1992b, Z. Phys. C **53**, 375.

ALEPH Collaboration, D. Buskulic *et al.*, 1993a, Phys. Lett. B **313**, 535.

ALEPH Collaboration, D. Buskulic *et al.*, 1993b, Phys. Lett. B **313**, 549.

ALEPH Collaboration, D. Buskulic *et al.*, 1994a, Z. Phys. C **62**, 179.

ALEPH Collaboration, D. Buskulic *et al.*, 1994b, Phys. Lett. B **335**, 99.
ALEPH Collaboration, D. Buskulic *et al.*, 1994c, Z. Phys. C **62**, 1.
ALEPH Collaboration, D. Buskulic *et al.*, 1994d, Z. Phys. C **62**, 539.
ALEPH Collaboration, D. Buskulic *et al.*, 1994e, Nucl. Instrum. Methods Phys. Res. A **346**, 461.
ALEPH Collaboration, D. Buskulic *et al.*, 1994f, Z. Phys. C **62**, 539.
ALEPH Collaboration, D. Buskulic *et al.*, 1995a, Phys. Lett. B **352**, 479.
ALEPH Collaboration, D. Buskulic *et al.*, 1995b, Nucl. Instrum. Methods Phys. Res. A **360**, 481.
ALEPH Collaboration, D. Buskulic *et al.*, 1995c, Phys. Lett. B **343**, 444.
ALEPH Collaboration, D. Buskulic *et al.*, 1995d, Phys. Lett. B **357**, 699.
ALEPH Collaboration, D. Buskulic *et al.*, 1996a, Z. Phys. C **71**, 357.
ALEPH Collaboration, D. Buskulic *et al.*, 1996b, Phys. Lett. B **384**, 414.
ALEPH Collaboration, D. Buskulic *et al.*, 1996c, Phys. Lett. B **378**, 373.
ALEPH Collaboration, D. Buskulic *et al.*, 1996d, Z. Phys. C **69**, 183.
ALEPH Collaboration, D. Buskulic *et al.*, 1996e, "Measurement of R_c," Paper contributed to ICHEP 96, Warsaw, PA10-016.
ALEPH Collaboration, D. Buskulic *et al.*, 1997a, Phys. Lett. B **401**, 150.
ALEPH Collaboration, D. Buskulic *et al.*, 1997b, Phys. Lett. B **401**, 163.
ALEPH Collaboration, R. Barate *et al.*, 1997c, Phys. Lett. B **399**, 329.
ALEPH Collaboration, R. Barate *et al.*, 1997d, "Study of Charmed Hadron Production in Z Decays," Paper contributed to EPS HEP'97, Jerusalem, EPS-623.
ALEPH Collaboration, R. Barate *et al.*, 1997e, Phys. Lett. B **401**, 347.
Alexander, G., *et al.*, 1988 in *Proceedings of the Workshop on Polarization at LEP*, edited by G. Alexander, G. Altarelli, A. Blondel, G. Coignet, E. Keil, D. E. Plane, and D. Treille (CERN 88-06 Geneva), Vol. 2, p. 3.
Alley, R., *et al.*, 1995, Nucl. Instrum. Methods Phys. Res. A **365**, 1.
Altarelli, G., 1982, Phys. Rep. **81**, 1.
Altarelli, G., 1997, Acta Phys. Pol. B **28**, 3.
Altarelli, G., R. Barbieri, and F. Caravaglios, 1993a, Nucl. Phys. B **405**, 3.
Altarelli, G., R. Barbieri, and F. Caravaglios, 1993b, Phys. Lett. B **314**, 357.
Altarelli, G., R. Barbieri, and F. Caravaglios, 1995, Phys. Lett. B **349**, 145.
Altarelli, G., R. Barbieri, and S. Jadach, 1992, Nucl. Phys. B **369**, 3.
Altarelli, G., N. Cabibbo, G. Corbo, L. Maiani, and G. Martinelli, 1982, Nucl. Phys. B **208**, 365.
Altarelli, G., and G. Isidori, 1994, Phys. Lett. B **337**, 141.
Altarelli, G., and B. Lampe, 1993, Nucl. Phys. B **391**, 3.
Altarelli, G., and S. Petrarca, 1991, Phys. Lett. B **261**, 303.
Alvarez-Gaumé, L., J. Polchinski, and M. Wise, 1983, Nucl. Phys. B **221**, 495.
Amaldi, U., A. Bohm, L. S. Durkin, P. Langacker, K. Mann, W. J. Marciano, A. Sirlin, and H. H. Williams, 1987, Phys. Rev. D **36**, 1385.
Arbuzov, A., *et al.*, 1996, Phys. Lett. B **383**, 238.
ARGUS Collaboration, H. Albrecht *et al.*, 1990, Phys. Lett. B **249**, 359.
ARGUS Collaboration, H. Albrecht *et al.*, 1993, Z. Phys. C **57**, 533.
Arnaudon, L., 1992, Phys. Lett. B **284**, 431.
Arnaudon, L., *et al.*, 1994, Z. Phys. C **66**, 45.
Arnaudon, L., *et al.*, 1995, Nucl. Instrum. Methods Phys. Res. A **357**, 249.
Arnaudon, L., *et al.*, 1992, "The Energy Calibration of LEP in 1991," CERN-PPE/92-125, CERN-SL/92-37 (DI).
Assmann, R., *et al.*, 1995, Z. Phys. C **66**, 567.
Assmann, R., *et al.*, 1998, "Calibration of the centre-of-mass energies at LEP1 for perecise measurements of Z properties," CERN-EP/98-12.
Barbieri, R., 1988, Riv. Nuovo Cimento **11**, 1.
Barbieri, R., F. Caravaglios, and M. Frigeni, 1992, Phys. Lett. B **279**, 169.
Barbieri, R., and L. Maiani, 1983, Nucl. Phys. B **224**, 32.
Bardin, G., J. Duclos, A. Magnon, J. Martino, E. Zavattini, A. Bertin, M. Capponi, M. Piccinini, and A. Vitale, 1984, Phys. Lett. B **137**, 135.
Bardin, D., M. S. Bilenkii, G. Mitselmakher, T. Riemann, and M. Sachwitz, 1989, Z. Phys. C **44**, 493.
Bardin, D., M. Bilenkii, A. Chizhov, A. Sazonov, O. Fedorenko, T. Riemann, and M. Sachwitz, 1991a, Nucl. Phys. B **351**, 1.
Bardin, D., M. Bilenkii, A. Sazonov, Yu. Sedykh, T. Riemann, and M. Sachwitz, 1991b, Phys. Lett. B **255**, 149.
Bardin, D., W. Hollik, and T. Riemann, 1991c, Z. Phys. C **49**, 485.
Bardin D., *et al.*, 1992, CERN-TH/6443-92, Computer Code ZFITTER, based on the papers of Bardin *et al.* (1989, 1991a, 1991b).
Bardin, D., W. Hollik, and G. Passarino, 1995, Eds., *Proceedings of the Working Group on Precision Calculations for the Z resonance* (CERN 95-03, Geneva).
Beenakeer, W., F. A. Berends, and S. C. van der Mark, 1991a, Nucl. Phys. B **355**, 281.
Beenakeer, W., F. A. Berends, and S. C. van der Mark, 1991b, Nucl. Phys. B **349**, 323.
Beenakker, W., and W. Hollik, 1988, Z. Phys. C **40**, 141.
Behrends, R. E., R. J. Finkelstein, and A. Sirlin, 1956, Phys. Rev. **101**, 866.
Bella, G., 1995, Nucl. Phys. B (Proc. Suppl.) **40**, 475.
Bellantoni, L., *et al.*, 1991, Nucl. Instrum. Methods Phys. Res. A **310**, 618.
Berends, F. A., G. J. H. Burgers, and W. L. Van Neerven, 1987, Phys. Lett. B **185**, 395.
Bliek, L., *et al.*, 1985, IEEE Trans Instrum. Meas. **IM-34**, 304.
Blondel, A., B. W. Lynn, F. M. Renard, and C. Verzegnassi, 1988, Nucl. Phys. B **304**, 438.
Blondel, A., 1990, in *Radiative Corrections*, edited by N. Dombej and F. Boudjema (Plenum, London), p. 35.
Bonneau, G., and F. Martin, 1971, Nucl. Phys. B **27**, 381.
Borelli, A., M. Consoli, L. Maiani, and R. Sisto, 1990, Nucl. Phys. B **333**, 357.
Bortolotto, C., *et al.*, 1991, Nucl. Instrum. Methods Phys. Res. A **306**, 459.
Bottigli, U., 1993, Phys. Medica **9**, 75.

Boulware, M., and D. Finnel, 1991, Phys. Rev. D **44**, 2054.
Burgers, G., F. Jegerlehner, B. Kniehl, and J. H. Kühn, 1989, in *Proceedings of the Workshop on Z Physics at LEP 1*, edited by G. Altarelli, R. Kleiss, and C. Verzegnassi (CERN 89-08, Geneva), Vol. 1, p. 55.
Burgers, G., W. Hollik, and M. Martinez, 1990, Computer code BHM, initially based on the work of Consoli *et al.* (1989) and Burgers *et al.* (1989).
Burkhardt, H., and B. Pietrzyk, 1995, Phys. Lett. B **356**, 398.
Cabibbo, N., and R. Gatto, 1961, Phys. Rev. **124**, 1577.
Cabibbo, N., L. Maiani, G. Parisi, and R. Petronzio, 1979, Nucl. Phys. B **158**, 295.
Cage, M. E., *et al.*, 1985, IEEE Trans Instrum. Meas. **IM-34**, 301.
Casas, J., J. Espinosa, and M. Quiros, 1995, Phys. Lett. B **342**, 171.
CCFR Collaboration, P. G. Reutens *et al.*, 1985, Phys. Lett. B **152**, 404.
CCFR Collaboration, K. McFarland *et al.*, 1996, in *Electroweak Interactions and Unified Theories*, Proceedings of the XXXIst Rencontre de Moriond, Les Arcs, edited by J. Tran Thanh Van (Editions Frontières, Paris), p. 97.
CDF Collaboration, F. Abe *et al.*, 1995a, Phys. Rev. D **52**, 4784.
CDF Collaboration, F. Abe *et al.*, 1995b, Phys. Rev. Lett. **74**, 2626.
CDF Collaboration, A. Gordon *et al.*, 1997a, in *Electroweak Interactions and Unified Theories*, Proceedings of the XXXIInd Rencontre de Moriond, Les Arcs, edited by J. Tran Thanh Van (Editions Frontières, Paris), p. 109.
CDF Collaboration, F. Abe *et al.*, 1997b, Phys. Rev. Lett. **80**, 2767.
CDF Collaboration, F. Abe *et al.*, 1997c, Phys. Rev. Lett. **79**, 2192.
CDHS Collaboration, H. Abramowicz *et al.*, 1986, Phys. Rev. Lett. **57**, 298.
CHARM Collaboration, J. V. Allaby *et al.*, 1987, Z. Phys. C **36**, 611.
Chetykin, K. G., J. H. Kühn, and A. Kwiatkowski, 1996, Phys. Rep. **277**, 189.
Chivukula, R. S., S. B. Selipsky, and E. H. Simmons, 1992, Phys. Rev. Lett. **69**, 575.
CLEO Collaboration, D. Bortoletto *et al.*, 1988, Phys. Rev. D **37**, 1719.
CLEO Collaboration, S. Henderson *et al.*, 1992, Phys. Rev. D **45**, 2212.
CLEO Collaboration, A. Bean *et al.*, 1993, Phys. Lett. B **317**, 647.
Cohen, E., and B. Taylor, 1986, Rev. Mod. Phys. **59**, 1128.
Consoli, M., W. Hollik, and F. Jegerlehner, 1989, in *Proceedings of the Workshop on Z Physics at LEP 1*, edited by G. Altarelli, R. Kleiss, and C. Verzegnassi (CERN 89-08, Geneva), Vol. 1, p. 7.
Costa, G., J. Ellis, G. L. Fogli, D. V. Nanopoulos, and F. Zwirner, 1988, Nucl. Phys. B **297**, 244.
DØ Collaboration, S. Abachi *et al.*, 1995, Phys. Rev. Lett. **74**, 2632.
DØ Collaboration, S. Abachi *et al.*, 1996, Phys. Lett. B **385**, 471.
DØ Collaboration, D. Wood *et al.*, 1997a, in *Electroweak Interactions and Unified Theories*, Proceedings of the XXXIInd Rencontre de Moriond, Les Arcs, edited by J. Tran Thanh Van (Editions Frontières, Paris), p. 117.
DØ Collaboration, Abachi, S. *et al.* 1997b, Phys. Rev. Lett. **79**, 1197.
Davier, M., *et al.*, 1993, Phys. Lett. B **306**, 411.
Degrassi, G., P. Gambino, and A. Vicini, 1996, Phys. Lett. B **383**, 219.
Degrassi, G., P. Gambino, and A. Sirlin, 1997a, Phys. Lett. B **394**, 188.
Degrassi, G., P. Gambino, M. Passera, and A. Sirlin, 1997b, "Role of M_W in Precision Studies of the Standard Model," CERN-TH/97-197.
DELCO Collaboration, W. Bacino *et al.*, 1979, Phys. Rev. Lett. **43**, 1073.
Delhaye, F., *et al.*, 1986, Metrologia **22**, 103.
DELPHI Collaboration, P. Abreu *et al.*, 1990, Phys. Lett. B **252**, 140.
DELPHI Collaboration, P. Aarnio *et al.*, 1991, Nucl. Instrum. Methods Phys. Res. A **303**, 233.
DELPHI Collaboration, P. Abreu *et al.*, 1992a, Phys. Lett. B **277**, 371.
DELPHI Collaboration, P. Abreu *et al.*, 1992b, Phys. Lett. B **295**, 383.
DELPHI Collaboration, P. Abreu *et al.*, 1992c, Z. Phys. C **53**, 555.
DELPHI Collaboration, P. Abreu *et al.*, 1993, Z. Phys. C **59**, 533.
DELPHI Collaboration, P. Abreu *et al.*, 1994a, Phys. Lett. B **341**, 109.
DELPHI Collaboration, P. Abreu *et al.*, 1994b, Nucl. Phys. B **418**, 403.
DELPHI Collaboration, P. Abreu *et al.*, 1995a, Z. Phys. C **66**, 341.
DELPHI Collaboration, P. Abreu *et al.*, 1995b, Z. Phys. C **65**, 555.
DELPHI Collaboration, P. Abreu *et al.*, 1995c, Z. Phys. C **65**, 569.
DELPHI Collaboration, P. Abreu *et al.*, 1995d, Z. Phys. C **67**, 1.
DELPHI Collaboration, P. Abreu *et al.*, 1995e, Z. Phys. C **67**, 183.
DELPHI Collaboration, P. Abreu *et al.*, 1995f, Z. Phys. C **65**, 603.
DELPHI Collaboration, P. Abreu *et al.*, 1996a, Z. Phys. C **70**, 531.
DELPHI Collaboration, P. Abreu *et al.*, 1996b, "Summary of R_c measurements in Delphi," Contributed paper to ICHEP 96, Warsaw, PA01-060.
DELPHI Collaboration, P. Abreu *et al.*, 1997a, "Measurement of the partial decay width $R_b^0 = \Gamma_{b5}\Gamma_{\rm had}$ with the DELPHI detector at LEP," Paper contributed to EPS HEP'97, Jerusalem, EPS-419.
DELPHI Collaboration, P. Abreu *et al.*, 1997b, Phys. Lett. B **397**, 158.
Djouadi, A., J. H. Kühn, and P. M. Zerwas, 1990, Z. Phys. C **46**, 411.
Djouadi, A., B. Lampe, and P. M. Zerwas, 1995, Z. Phys. C **67**, 123.
Eidelman, S., and F. Jegerlehner, 1995, Z. Phys. C **67**, 585.
Ellis, J., G. L. Fogli, and E. Lisi, 1995, Phys. Lett. B **343**, 282.
Ezion, E., 1997, in *International Europhysics Conference on High Energy Physics*, Jerusalem 1997, edited by D. Lelouch, G. Mikenberg, and E. Rabinovici (Springer, Berlin), p. 671.
Farhi, E., and L. Susskind, 1981, Phys. Rep. **74**, 277.

Farley, F. J. M., and E. Picasso, 1990, in *The Muon g-2 Experiment in Quantum Electrodynamics*, edited by T. Kinoshita (World Scientific, Singapore), p. 479.
FMM Collaboration, D. Bogert *et al.*, 1985, Phys. Rev. Lett. **55**, 1969.
Garcia, D., and J. Solà, 1995, Phys. Lett. B **354**, 335.
Giovannetti, K. L., *et al.*, 1984, Phys. Rev. D **29**, 343.
Glashow, S. L., 1961, Nucl. Phys. **22**, 579.
Grinstein, B., M. B. Wise, and N. Isgur, 1986, Phys. Rev. Lett. **56**, 298.
Haber, H. E., and G. L. Kane, 1985, Phys. Rep. **117**, 75.
Hartland, A., *et al.*, 1985, IEEE Trans Instrum. Meas. **IM-34**, 309.
Harton, J., 1995, Nucl. Phys. B (Proc. Suppl.) **40**, 463.
Hasert, F. J., *et al.*, 1973, Phys. Lett. B **46**, 138.
Hebbeker, T., M. Martinez, G. Passarino, and G. Quast, 1994, Phys. Lett. B **331**, 165.
Hewett, J. L., and T. Rizzo, 1989, Phys. Rep. **183**, 193, and references therein.
Hildreth, M. D., *et al.*, 1996, ''Preliminary RF Corrections to the LEP energy for the 1995 scan,'' CERN LEP energy working group 96-02. http://www.cern.ch/LEPECAL/reports/reports.html
Hollik, W., 1990a, Fortschr. Phys. **38**, 165.
Hollik, W., 1990b, Mod. Phys. Lett. A **5**, 1909.
Hollik, W., 1993, in *Precision Tests of the Standard Electroweak Model*, edited by P. Langacker (World Scientific, Singapore), p. 37.
Hollik, W., 1995, ''Electroweak Theory,'' hep-ph/9602380.
HRS Collaboration, P. Baringer *et al.*, 1988, Phys. Lett. B **206**, 551.
Isgur, N., D. Scora, B. Grinstein, and M. B. Wise, 1989, Phys. Rev. D **39**, 799.
Jadach, S., J. H. Kühn, and Z. Wąs, 1991, Comput. Phys. Commun. **64**, 75.
Jadach, S., W. Placzek, E. Richter-Wąs, B. F. L. Ward, and Z. Wąs, 1997, Comput. Phys. Commun. **102**, 229.
Jadach, S., E. Richter-Wąs, B. F. L. Ward, and Z. Wąs, 1992, Comput. Phys. Commun. **70**, 305.
Jadach, S., and B. F. L. Ward, 1988, Phys. Rev. D **38**, 2897.
Jadach, S., and B. F. L. Ward, 1989, Phys. Rev. D **40**, 3582.
Jadach, S., and B. F. L. Ward, 1996, Phys. Lett. B **389**, 129.
Jadach, S., and Z. Wąs, 1989 in *Proceedings of the Workshop on Z Physics at LEP 1*, edited by G. Altarelli, R. Kleiss, and C. Verzegnassi (CERN, Geneva), Vol. 1, p. 235.
Jadach, S., Z. Wąs, R. Decker, M. Jeżabek, and J. H. Kühn, 1993, Comput. Phys. Commun. **76**, 361.
Jadach, S., B. F. L. Ward, and Z. Wąs, 1991, Comput. Phys. Commun. **66**, 276.
Jadach, S., B. F. L. Ward, and Z. Wąs, 1994, Comput. Phys. Commun. **79**, 503.
JADE Collaboration, S. Bethke *et al.*, 1988, Phys. Lett. B **213**, 235.
Janot, P., 1997, in *International Europhysics Conference on High Energy Physics*, Jerusalem, 1997, edited by P. Lelouch, G. Mikenberg, and E. Rabinovici (Springer, Berlin), p. 212.
Jowett, J. M., J. Wenninger, and J. Yamartino, 1995, ''Influence of Dispersion and Collision Offsets on the Centre-of-Mass Energy at LEP,'' CERN-SL/95-46 (OP). http://www.cern.ch/LEPECAL/reports/reports.html
Kennedy, D. C., and P. Langacker, 1990, Phys. Rev. Lett. **65**, 2967.
Kim, Y. K., 1997, in *Proceedings of the 18th International Symposium On Leptron-Photon Interactions (LP97)*, Hamburg, 1997, edited by A. De Roeck and A. Wagner (World Scientific, Singapore), p. 493.
Kinoshita, T., and W. B. Lindquist, 1981, Phys. Rev. Lett. **47**, 1573.
Kinoshita, T., and W. B. Lindquist, 1983, Phys. Rev. D **27**, 853; 1983, **27**, 867; 1983, **27**, 877; 1983, **27**, 886.
Kinoshita, T., and A. Sirlin, 1959, Phys. Rev. **113**, 1652.
Kleiss, R., *et al.*, 1989, in *Proceedings of the Workshop on Z Physics at LEP 1*, edited by G. Altarelli, R. Kleiss, and C. Verzegnassi (CERN, Geneva), Vol. 3, p. 129.
Kounine, A., 1995, Nucl. Phys. B (Proc. Suppl.) **40**, 437.
Kühn, J. H., and E. Mirkes, 1992, Z. Phys. C **56**, 661.
L3 Collaboration, B. Adeva *et al.*, 1990, Nucl. Instrum. Methods Phys. Res. A **289**, 35.
L3 Collaboration, O. Adriani *et al.*, 1992, Phys. Lett. B **292**, 454.
L3 Collaboration, O. Adriani *et al.*, 1993a, Phys. Lett. B **317**, 467.
L3 Collaboration, O. Adriani *et al.*, 1993b, Phys. Lett. B **307**, 237.
L3 Collaboration, O. Adriani *et al.*, 1993c, Phys. Lett. B **306**, 187.
L3 Collaboration, O. Adriani *et al.*, 1993d, Phys. Lett. B **301**, 136.
L3 Collaboration, M. Acciarri *et al.*, 1994a, Phys. Lett. B **335**, 542.
L3 Collaboration, M. Acciarri *et al.*, 1994b, Phys. Lett. B **341**, 245.
L3 Collaboration, M. Acciarri *et al.*, 1994c, Z. Phys. C **62**, 551
L3 Collaboration, M. Acciarri *et al.*, 1996, Phys. Lett. B **374**, 331.
L3 Collaboration, M. Acciarri *et al.*, 1997a, ''Measurement of R_b with the L3 Detector,'' Paper contributed to EPS HEP'97, Jerusalem, EPS-489.
L3 Collaboration, M. Acciarri *et al.*, 1997b, Phys. Lett. B **407**, 361.
L3 Collaboration, M. Acciarri *et al.*, 1997c, Phys. Lett. B **398**, 223.
Lançon, E., and A. Blondel, 1996, ''Determination of LEP Energy Spread using Experimental Constraints,'' LEP Energy Working group note 96-10. http://www.cern.ch/LEPECAL/reports/reports.html
Langacker, P., 1989, Phys. Rev. Lett. **63**, 1920.
Leike, A., T. Riemann, and J. Rose, 1991, Phys. Lett. B **273**, 513.
LEP Electroweak Group (The LEP Collaborations, ALEPH, DELPHI, L3, OPAL, and the LEP Electroweak Working Group), 1996, Nucl. Instrum. Methods Phys. Res. A **378**, 101.
LEP Electroweak Group (The LEP Collaborations ALEPH, DELPHI, L3, OPAL, The LEP Electroweak Working Group, and the SLD Heavy Flavour Group), 1997, ''A Combination of Preliminary Electroweak Measurements and Constraints on the Standard Model,'' CERN-PPE/97-154.
Letts, J., and P. Mattig, 1997, Z. Phys. C **73**, 217.
Lindner, M., 1986, Z. Phys. C **31**, 295.

Llewellyn Smith, C. H., 1983, Nucl. Phys. B **228**, 205.
Lonnblad, L., C. Peterson, and T. Rognvaldsson, 1991, Nucl. Phys. B **349**, 675.
Luscher, M., and P. Weisz, 1988, Phys. Lett. B **212**, 472.
Lynn, B. W., 1988, in *Proceedings of the Workshop on Polarization at LEP*, CERN 88-06, edited by G. Alexander, G. Altarelli, A. Blondel, G. Coignet, E. Keil, D. E. Plane, and D. Treille (CERN, Geneva), Vol. 1, p. 24.
Marciano, W. J., and A. Sirlin, 1980, Phys. Rev. D **22**, 2695.
MARK II Collaboration, R. Jacobsen *et al.*, 1991, Phys. Rev. Lett. **67**, 3347.
MARK III Collaboration, R. M. Baltrusaitis *et al.*, 1985, Phys. Rev. Lett. **54**, 1976.
MARK III Collaboration, D. Coffman *et al.*, 1991, Phys. Lett. B **263**, 135.
Martinez, M., L. Garrido, R. Miquel, J. L. Harton, and R. Tanaka, 1991, Z. Phys. C **49**, 645.
Maruyama, T., E. L. Garwin, R. Prepost, and G. Zapalac, 1992, Phys. Rev. B **46**, 4261.
Montagna, G., O. Nicrosini, G. Passarino, F. Piccinini, and R. Pittau, 1993, Comput. Phys. Commun. **76**, 328.
Nilles, H. P., 1984, Phys. Rep. **110**, 1.
Novikov, V., L. Okun, and M. Vytsotsky, 1993, Nucl. Phys. B **397**, 35.
Olshevski, A., 1995, in *Proceedings of the International Euroconference on High Energy Physics*, Brussels, 1995, edited by J. Lemonne, C. Vander Velde, and F. Verbeure (World Scientific, Singapore).
OPAL Collaboration, G. Alexander *et al.*, 1991a, Phys. Lett. B **266**, 485.
OPAL Collaboration, K. Ahmet *et al.*, 1991b, Nucl. Instrum. Methods Phys. Res. A **305**, 34.
OPAL Collaboration, G. Alexander *et al.*, 1992, Phys. Lett. B **294**, 436.
OPAL Collaboration, P. D. Acton *et al.*, 1993a, Z. Phys. C **60**, 579.
OPAL Collaboration, R. Akers *et al.*, 1993b, Z. Phys. C **60**, 19.
OPAL Collaboration, R. Akers *et al.*, 1993c, Z. Phys. C **60**, 601.
OPAL Collaboration, R. Akers *et al.*, 1993d, Z. Phys. C **60**, 199.
OPAL Collaboration, R. Akers *et al.*, 1994a, Z. Phys. C **61**, 19.
OPAL Collaboration, R. Akers *et al.*, 1994b, Z. Phys. C **61**, 209.
OPAL Collaboration, R. Akers *et al.*, 1995a, Phys. Lett. B **353**, 595.
OPAL Collaboration, R. Akers *et al.*, 1995b, Z. Phys. C **65**, 17.
OPAL Collaboration, R. Akers *et al.*, 1995c, Z. Phys. C **67**, 27.
OPAL Collaboration, R. Akers *et al.*, 1995d, Z. Phys. C **67**, 365.
OPAL Collaboration, R. Akers *et al.*, 1996a, Z. Phys. C **70**, 357.
OPAL Collaboration, K. Ackerstaff *et al.*, 1996b, Z. Phys. C **72**, 1.
OPAL Collaboration, G. Alexander *et al.*, 1996c, Z. Phys. C **72**, 365.
OPAL Collaboration, K. Ackerstaff *et al.*, 1996d, Phys. Lett. B **389**, 416.
OPAL Collaboration, K. Ackerstaff *et al.*, 1997a, Z. Phys. C **74**, 1.
OPAL Collaboration, G. Alexander *et al.*, 1997b, Z. Phys. C **73**, 379.
OPAL Collaboration, K. Ackerstaff *et al.*, 1997c, Z. Phys. C **75**, 385.
OPAL Collaboration, K. Ackerstaff *et al.*, 1997d, Eur. Phys. J. C **1**, 439.
OPAL Collaboration, K. Ackerstaff *et al.*, 1997e, "Tests of the Standard Model and Constraints on New Physics from Measurements of Fermion Pair Production at 130-GEV to 172-GEV at LEP," CERN-PPE/97-101.
OPAL Collaboration, K. Ackerstaff *et al.*, 1997f, Z. Phys. C **76**, 387.
Particle Data Group, R. M. Barnett *et al.*, 1996, Phys. Rev. D **54**, 1.
Peskin, M., and T. Takeuchi, 1990, Phys. Rev. Lett. **65**, 964.
Peterson, C., D. Schlatter, I. Schmitt, and P. Zerwas, 1982, Phys. Rev. D **27**, 105.
Phinney, N., 1993, Int. J. Mod. Phys. A **45**, 2A.
Privitera, P., 1993, Phys. Lett. B **308**, 163.
Quast, G., 1997, in *International Europhysics Conference on High Energy Physics*, Jerusalem, 1997, edited by D. Lelouch, G. Mikenberg, and E. Rabinovici (Springer, Berlin), p. 679.
Ratoff, P., 1996, in *Proceedings of the 28th International Conference on High Energy Physics*, Warsaw, edited by Z. Ajduk and A. K. Wroblewski (World Scientific, Singapore), Vol. 1, p. 884.
Riemann, T., 1992, Phys. Lett. B **293**, 451.
Riemann, S., 1993, Computer Code ZEFIT based on Riemann (1994).
Riemann, S., 1994, Ph.D. thesis (Aachen Tech. Hochshule).
Ross, G. G., 1987, *Grand Unified Theories* (Cambridge University, Cambridge), and references therein.
Rougé, A., 1990, in *Proceedings of the 1st International Workshop on τ Lepton Physics*, Orsay, edited by M. Davier and B. Jean-Marie (Editions Frontières, Paris), p. 213.
Rumelhart, D. E., G. E. Hinton, and R. J. William, 1986, Nature **323**, 533.
Salam, A., 1968, in *Proceedings of the 8th Nobel Symposium*, edited by Aspenaegarden (Almqvist and Wicksell, Stockholm), p. 367.
Schmelling, M., 1996, in *Proceedings of the 28th International Conference on High Energy Physics*, Warsaw, edited by Z. Ajduk and A. K. Wroblewski (World Scientific, Singapore), Vol. 1, p. 91.
Schumm, B., 1997, "Electroweak Results from the SLD," SLAC-PUB-7697.
Seymour, M. H., 1995, Nucl. Phys. B **436**, 136.
Shepherd-Themistocleous, C. H., 1996, in *Proceedings of the 28th International Conference on High Energy Physics*, Warsaw, edited by Z. Ajduk and A. K. Wroblewski (World Scientific, Singapore), Vol. 1, p. 880.
Sher, M., 1989, Phys. Rep. **179**, 273.
Sjostrand, T., 1994, Comput. Phys. Commun. **82**, 74.
Sjostrand, T., and M. Bengtsson, 1987, Comput. Phys. Commun. **43**, 367.
Sjostrand, T., and M. Bengtsson, 1989, The LUND Monte Carlo Programs, CERN long write-up, unpublished.
SLD Collaboration, 1984, The SLD design report, SLAC Report 273. http://www-sld.slac.stanford.edu/sldwww/sldintro/sldintro.html
SLD Collaboration, K. Abe *et al.*, 1994, Phys. Rev. Lett. **73**, 25.
SLD Collaboration, K. Abe *et al.*, 1995a, Phys. Rev. Lett. **75**, 3609.
SLD Collaboration, K. Abe *et al.*, 1995b, Phys. Rev. Lett. **74**, 2890.

SLD Collaboration, K. Abe *et al.*, 1995c, Phys. Rev. Lett. **74**, 2895.
SLD Collaboration, K. Abe *et al.*, 1997a, Phys. Rev. Lett. **78**, 2075.
SLD Collaboration, K. Abe *et al.*, 1997b, "Measurement of Ab from the Left-Right Forward-Backward Asymmetry in $Z0$ Decays using Charged Kaon Tagging," Paper contributed to EPS HEP'97, Jerusalem, EPS-123.
SLD Collaboration, K.. Abe *et al.*, 1997c, "Measurement of Ab at the $Z0$ Resonance using a Jet-Charge Technique," Paper contributed to EPS HEP'97, Jerusalem, EPS-122.
SLD Collaboration, K. Abe *et al.*, 1997d, "Measurement of Ab and Ac at the $Z0$ Pole using a Lepton Tag," Paper contributed to EPS HEP'97, Jerusalem, EPS-124.
SLD Collaboration, K. Abe *et al.*, 1997e, "Measurement of Ac with Reconstructed D*+ and D+ Mesons," "A Measurement of Rb using a Vertex Mass Tag," Paper contributed to EPS HEP'97, Jerusalem, EPS-125.
SLD Collaboration, K. Abe *et al.*, 1997f, "A Measurement of Rb using a Vertex Mass Tag," Paper contributed to EPS HEP'97, Jerusalem, EPS-118.
Sokolov, A., and I. M. Ternov, 1964, Dokl. Akad. Nauk SSSR **153**, 1052 [Sov. Phys. Dokl. **8**, 1203 (1963)].
Steinberger, J., 1997, in *Electroweak Interactions and Unified Theories*, Proceedings of the XXXIInd Rencontre de Moriond, Les Arcs, edited by J. Tran Thanh Van (Editions Frontières, Paris), p. 149.
Stuart, R. G., 1987, Z. Phys. C **43**, 445.
Stuart, R. G., 1991, Phys. Lett. B **272**, 353.
TASSO Collaboration, M. Althoff *et al.*, 1984, Phys. Lett. B **149**, 524.
TASSO Collaboration, W. Braunschweig *et al.*, 1989a, Z. Phys. C **44**, 365.
TASSO Collaboration, W. Braunschweig *et al.*, 1989b, Z. Phys. C **44**, 1.
TOPAZ Collaboration, K. Miyabayashi *et al.*, 1995, Phys. Lett. B **347**, 171.
Tsai, Y. S., 1971, Phys. Rev. D **4**, 2821.
UA1 Collaboration, G. Arnison *et al.*, 1983a, Phys. Lett. B **122**, 103.
UA1 Collaboration, G. Arnison *et al.*, 1983b, Phys. Lett. B **126**, 398.
UA2 Collaboration, M. Banner *et al.*, 1983a, Phys. Lett. B **122**, 476.
UA2 Collaboration, P. Bagnaia *et al.*, 1983b, Phys. Lett. B **129**, 130.
UA2 Collaboration, J. Alitti *et al.*, 1992, Phys. Lett. B **276**, 354.
Van del Wel, W., *et al.* 1985, IEEE Trans Instrum. Meas. **IM-34**, 314.
Van Dick, Jr., R. S., P. B. Schwinberg, and H. G. Dehmet, 1984, in *The Electron and Positron Geonium Experiment*, Atomic Physics 9, edited by S. Van Dick and E. Norval (World Scientific, Singapore), p. 53.
Wada, T., *et al.* 1985, IEEE Trans Instrum. Meas. **IM-34**, 306.
Weinberg, S., 1967, Phys. Rev. Lett. **19**, 1264.
Weinberg, S., 1976, Phys. Rev. D **13**, 974.
Wenninger, J., 1994, "Study of the LEP Beam Energy with Beam Orbits and Tunes," CERN-SL/94-14 (BI).
Woods, M., 1995, in *Proceedings of 11th International Symposium on High Energy Spin Physics*, Bloomington, Indiana, AIP Conf. Proc. No. 343, edited by K. J. Heller and S. L. Smith (AIP, New York), p. 911.
Worris, M. A., 1991, Ph.D. thesis (Cornell University).
Yennie, D. R., S. C. Frautschi, and H. Suura, 1961, Ann. Phys. (N.Y.) **13**, 379.